2013-04-11

Elucidation of Peptide Sequence Effects that Control the Activity, Size, and Function of Nanoparticles

Ryan H. Coppage
University of Miami, ryan.coppage@gmail.com

UNIVERSITY OF MIAMI

ELUCIDATION OF PEPTIDE SEQUENCE EFFECTS THAT CONTROL THE ACTIVITY, SIZE, AND FUNCTION OF NANOPARTICLES

By

Ryan Coppage

A DISSERTATION

Submitted to the Faculty
of the University of Miami
in partial fulfillment of the requirements for
the degree of Doctor of Philosophy

Coral Gables, Florida

May 2013

UNIVERSITY OF MIAMI

A dissertation submitted in partial fulfillment of
the requirements for the degree of
Doctor of Philosophy

ELUCIDATION OF PEPTIDE SEQUENCE EFFECTS THAT CONTROL THE ACTIVITY, SIZE, AND FUNCTION OF NANOPARTICLES

Ryan H. Coppage

Approved:

_____
Marc R. Knecht, Ph.D.
Professor of Chemistry

_____
M. Brian Blake, Ph.D.
Dean of the Graduate School

_____
Rajeev Prabhakar, Ph.D.
Professor of Chemistry

_____
Roger M. Leblanc, Ph.D.
Professor of Chemistry

_____
Onur Tigli, Ph.D.
Professor of Electrical Engineering

COPPAGE, RYAN (Ph.D., Chemistry)
Elucidation of Peptide Sequence Effects that Control the Activity, Size, and Function of Nanoparticles. (May 2013)

Abstract of a dissertation at the University of Miami.

Dissertation supervised by Professor Marc R. Knecht.
No. of pages in text. (171)

Bio-inspired nanoparticle catalysis offers the opportunity to improve on current catalytic standards with respect to turnover efficiency, organic solvent use, and thermal activation. Unfortunately, projected energy demands will soon outweigh our fuel supplies. The task of creating multifunctional catalysts that both lower thermal activation and possess a number of functions in aqueous conditions is daunting. Similar to these needs, nature has evolved to create a wide range of highly specialized catalytic processes, which incorporate inorganic materials, take place in ambient temperatures, and in an aqueous environment. These specialized biological systems provide inspiration, but are not applicable to current needs. Exploitation of these biotic-abiotic systems could allow for green, multifunctional catalysts.

In the resulting works, a peptide sequence has been isolated via phage display with affinity for Pd surfaces, that forms stable, peptide-capped nanoparticles. Substitution of residues results in the tuning of both nanocatalyst activity and nanoparticle size, such that a peptide surface-controlling effect can be noted. These characteristics can be exploited to ultimately understand the binding interactions among bio-inorganic interfaces, such that a rational design of biomolecules can be realized for the synthesis of highly active, green, multifunctional nanomaterials.

L*earn from yesterday, live for today, hope for tomorrow.*
The important thing is not to stop questioning.
- Albert Einstein

ACKNOWLEDGEMENT

I owe thanks to many people, as my path has not been solely of my own obstinate tendencies or direction. There are many educators and mentors that have inspired and helped guide me through my time as a student. Most importantly, I would like to thank Dr. Marc Knecht for his guidance, vast knowledge, and his unmeasured patience with me as his graduate student. Many thanks to Dr. Terry McCreary, Dr. Daniel Johnson, and Beth Brubaker for engaging conversations and for friendship and encouragement. Also, thanks are owed to Dr. Nick Bedford and Dr. Joe Slocik, by whom many problems were solved via their vast knowledge and immediate answers.

I would like to express my appreciation to Dr. David Owen, Dr. Daniel Johnson, Dr. John Anthony, and Dr. John Balk for inspiring me to be the best teacher possible and showing me that the effort required far exceeds the standard. Thank you for demonstrating to me what it takes to be an effective teacher and discussing your tactics with me.

I am forever indebted to Dr. Terry McCreary, for his precious humor, savage wit, demeanor, and satirical perspective. Your outlook on life and corresponding philosophies have always been dear to me. Thank you for being patient when I was not and believing when I did not believe in myself.

Finally, I would like to thank the person that has made me the inquisitive skeptic that I am, my mother, who always taught me to question everything and decide what was right for myself. She was my very first teacher. I am only here because of your implanted obstinacy.

TABLE OF CONTENTS

List of Figures

List of Tables

List of Publications

1. Mirau, P. A.; Naik, R. R.; Coppage, R.; Knecht, M. R.; Ramezani-Dakhel, H.; Heinz, H.; Vaia, R. A.; Koerner, H.; Kotlarchyk, M. The Structure of Peptides at the Palladium Nanoparticle Interface. **2013**. *In Preparation.*

2. Coppage, R.; Slocik, J. M.; Bedford, N.; Knecht, M. R. Exploiting Peptide Sequence Effects to Enhance the Catalytic Reactivity of Nanoparticles. *J. Am. Chem. Soc.* **2013**. *In Revision.*

3. Coppage, R.; Slocik, J.M.; Briggs, B.D.; Frenkel, A.I.; Naik, R.R.; Knecht, M.R. Determining Peptide Sequence Effects that Control the Size, Structure, and Function of Nanoparticles. *ACS Nano*, **2012**, 1625-1636.

4. Bhandari, R.; Coppage, R.; Knecht, M. Mimicking Nature's Strategies for the Design of Nanocatalysts. *Catal. Sci. Technol.* **2012**, *2*, 256-266. (published as a HOT Article; featured on the inside front cover of the February 2012 issue.)

5. Coppage, R.; Slocik, J.M.; Briggs, B.D.; Frenkel, A.I.; Heinz, H.; Naik, R.R.; Knecht, M.R.; Crystallographic Recognition Controls Peptide Binding for Bio-based Nanomaterials. *J. Am. Chem. Soc.* **2011**, *133*, 12346-12349.

6. Coppage, R.; Slocik, J.M.; Sethi, M.; Pacardo, D.B.; Naik, R.R.; Knecht, M.R. Elucidation of Peptide Effects that Control the Activity of Nanoparticles, *Angew. Chem., Int. Ed.* **2010**, *49*, 3767-3770.

Chapter 1. Bio-Inspired Materials Catalysis

1.1 Introduction to Bio-Inspired Materials Catalysis

Currently, projected fossil fuel usage is predicted to exhaust available supplies in the next ~40 years.[1] To that end, the continued consumption of these fuels and subsequent CO_2 production is anticipated to result in ecological damage, including global warming,[2] ocean acidification,[3] and air quality/pollution concerns.[4] Additionally, this fuel exhaustion will result in an increase in energy costs associated with scarce fossil fuels, specifically oil reserves.[5] The projected consumption of fossil fuel reserves also greatly impacts the feed chemicals employed as the building blocks of current syntheses, including the production of bulk organic solvents. Taken together, these effects will lead to significantly higher costs associated with catalysis, resulting in a greater need for more energy-neutral material-synthesis processes. As such, the exhaustion of fossil fuels could cripple the chemical and materials industry over the next few decades. In light of this crisis, the development of less energy-dependent practices could help reduce energy concerns and lower overall energy consumption. To that end, developing lower-energy processes is one solution for the continued production of pharmaceuticals, complex molecules, and the development of molecular electronics.

The development of new, sustainable catalysis standards could prove to be beneficial for projected energy consumption. Though advances in catalysis have targeted energy neutrality, the fabrication of efficient, low-energy catalysts with a wide range of reactivities remains difficult. Catalysis is a process through which alternate, lower-energy pathways are followed for a chemical reaction, decreasing the activation energy for a specific process.[6] Due to this lower activation energy requirement, greater product yields

are typically observed at lower temperatures.[7] Current catalytic processes typically use large volumes of organic solvents, consume great amounts of energy, and produce byproducts and other waste that require specialized separations and disposal.[8,9] While these issues can be addressed individually, green catalysis offers a way to globally address these concerns.[10,11] Green catalysts function under energy-neutral and environmentally friendly conditions, including ambient temperatures and aqueous solvents. Replacing traditional catalysts with such ecologically and economically friendly materials would result in more efficient reaction processes, thereby significantly lowering production costs.[8]

Several types of catalysts are commonly employed for a variety of reactions; however, they are classified as either homogeneous or heterogeneous.[12] Homogeneous catalytic reactions are processed in a single phase where the catalyst exists in the same phase as the substrates. In contrast, heterogeneous catalysts are typically mounted onto a support or in a different phase from the reactants and are highly dependent on the diffusion of reagents and products to and from the reactive surface. Existing somewhat between these two types of catalysts are pseudo-homogeneous catalysts, in which the materials are in a different phase from the reactants and are dispersed in a solution, resulting in colloidal distribution.[13] Most nanocatalytic systems fall into this third state, thus raising the complications associated with their complete structure/function relationship determination.[12]

While catalysis reduces thermal loading and thus lowers fuel consumption, current systems are not sustainable as fossil fuel supplies decrease. To that end, it would be advantageous to develop more sustainable catalytic practices, including the

development of energy-neutral systems. Reflecting these standards, materials are needed that function at ambient temperatures and in aqueous solutions.[8] The use of nanomaterials as active catalysts has demonstrated superior reactivity for a number of catalytic processes, which may be attractive alternatives to achieve such functionality.[14] Furthermore, these systems frequently employ the use of low-temperature conditions and are often soluble in aqueous systems.

Nanomaterials possess at least one dimension in the size range of 1 – 100 nm. This size range is advantageous, as both the functionalization of the surface allows for the selective tuning of nanoparticle solubility and surface:volume ratio of these materials are highly desirable.[15] Due to the various metal composition and easily modulated surfaces, nanomaterials have received attention as potential high-efficiency catalysts.[16] Nanocatalyst materials exhibit an increased surface area exposure, resulting in a more efficient display of the catalytic material surface; this optimization of surface exposure results in enhanced catalyst reactivity. Nanocatalysts are difficult to fully classify as either homogenous or heterogeneous catalysts.[12] They are not truly homogenous as they are colloidally suspended throughout a solution, thus giving rise to different phases in the reaction mixture. Furthermore, nanocatalysts optimize the metal surface area for catalytic activity and are highly dispersed in the solution to minimize mass transport effects that can cause diminished reactivity rates. The development of nanocatalyst systems could reduce the amount of unnecessary waste and energy consumption for necessary processes.[8]

Additionally, the ligands employed in the synthesis of nanomaterials, which are required to achieve particle stability in the solvent system, have been demonstrated to

control access to the inorganic surface.[17,18] These ligands act as passivants, preventing bulk aggregation of the nanostructures. Furthermore, surface ligands can be designed to modulate solubility of the materials in addition to exposing active functional groups, which may further enhance material reactivity and allow for multifunctional use.[19,20] These ligands include the use of biological components such as peptides, proteins, and other biomolecules.[21] To that end, the biotic/abiotic interface of materials is significant for nanocatalyst activity, though a full understanding of biomolecule binding and ordering on inorganic surfaces is still not fully understood.

Evolution has shaped biological processes into a wide variety of specialized systems, with exacting control over inorganic structures.[22] These range from predation defense (spicule formation) and direction sensing to the formation of highly complex inorganic architectures through biomineralization.[22-24] The wide range of function with respect to limited component precursors provides for a highly desirable system of easily modulated and synthesized peptides. Though these naturally occurring biomineralization systems are incredibly complex and diverse, they typically do not possess many functions outside of their intended applications.

From the ability of inorganic materials organization, biomineralization has provided inspiration for the biomimetic synthesis of nanomaterials not present in the biosphere.[23] Bio-nanomaterials are synthesized with biological ligands as surface passivants to create biomolecule-capped metal nanostructures.[25,26] These nanomaterial systems can be incredibly tunable and monodisperse, including shape-specific, crystalline growth-directing, and multi-component materials.[27] Inorganic nanomaterial systems have been employed in catalysis,[26] assembly,[28] and delivery applications.[29] Of these

applications, the potential for the development of superior biomimetic nanocatalysts has received significant attention. The optimization of active surface area, aqueous solvent use, ambient temperatures, and extremely low consumption of precious metal materials make these systems highly desirable. These attributes make biomimetic nanomaterials ideal for use as catalysts in many reactions that otherwise employ high temperatures, high catalyst loadings, organic solvents, and lengthy reaction times.[30] Furthermore, bionanocatalysts have been targeted as a potential standard for more sustainable catalyst materials.[10] To this end, biomimetic nanoparticle-based systems have demonstrated significant catalytic activity in a range of applications, in addition to operating in ambient conditions.[31,32]

The bioligands on the particle surface can dramatically impact the overall nanomaterial reactivity. The biotic/abiotic interface must be designed to both expose the inorganic catalytic materials while maintaining nanoparticle stability.[20] A variety of ligands have been employed to synthesize these materials, including peptides, proteins, and binding molecules like streptavidin.[33-35] Furthermore, the short peptide sequences and proteins demonstrated to readily bind inorganic surfaces can be expressed through fusions on the cell surface or quickly synthesized on solid supports. Though surface-specific biomolecules have been demonstrated to passivate and support nanocatalyst functionality, the biotic/abiotic interface and binding effects are not fully understood. These peptides possess combinations of sequence-unique binding motifs, structures, and interfacial effects that remain difficult to predict. Additionally, the orientation, sequence, concentration, and structural/binding motif of the biomolecule passivant has been demonstrated to greatly affect catalytic reactivities.[36] While bionanocatalyst systems are

relatively new, they offer the potential to decrease reaction costs through lower energy requirements and aqueous solvent use. Additionally, the ambient temperatures at which they function provide optimal reaction conditions, allowing for more sustainable catalysis.

In this text, various biomimetic nanomaterial systems are outlined as potential nanocatalysts employing more sustainable methods. This includes the use of peptides and biomolecules for the synthesis of inorganic nanomaterials, structure assemblies, and complex nanoarchitecture design. While these works involve biomimetic inorganic materials synthesis and assembly, a number of them demonstrate the activities possible for nanomaterial systems applied as ambient-condition catalysts. Though the biotic/abiotic interface is still not fully understood, these works demonstrate an efficiency that is desirable in room-temperature, aqueous conditions. To that end, the continued development of bionanomaterials for applied nanocatalyst systems and sustainable catalyst standards would be economically and ecologically advantageous.

1.2 Phage Display

The design and synthesis of bio-inspired materials from the bottom up requires materials-directing peptides that can recognize and bind inorganic surfaces.[36] Ideally, these peptides should control the atomic arrangement of the metal atoms at the particle surface; however, such capabilities remain difficult to achieve. Since a majority of biomineralization processes are carried out through peptide interactions with inorganic materials, the rational design of such sequences could lead to specific nanomaterials.

These peptides can be isolated from random libraries through biocombinatorial processes such as phage display.[37] Bacteriophage are a type of virus, which infect prokaryotic bacteria to replicate. Some phage possess single-stranded DNA, thus making them ideal candidates for genetic engineering to easily modify their solution displayed coat proteins.[38] Most commonly used, the filamentous M13 phage, seen in **Figure 1.1** below, is composed of five different coat proteins, two at the recognition end, a capsid coat protein along the major shaft of the virus, and two at the opposite end. These phage are ~900 nm long and 6-8 nm wide, which can change dependent on the size of the enclosed cDNA. Protein modifications and additions are typically performed at the opposing end pIII and pIX minor coat proteins, in addition to the main capsid pVIII major coat protein.[39-41]

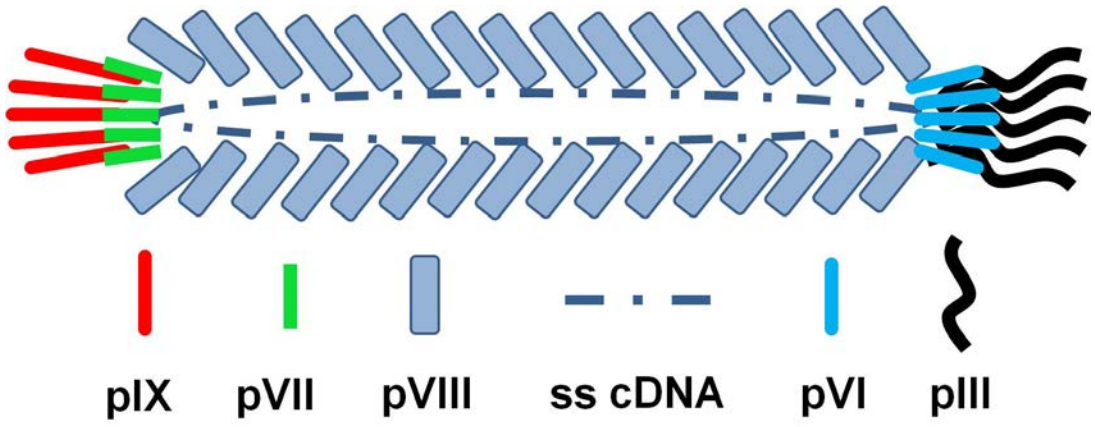

Figure 1.1. A filamentous M13 bacteriophage and its corresponding minor coat proteins, pIX, pVII, pVI, and pIII from left to right, respectively, the pVIII major coat protein and phage genomic ss cDNA.

The major pVIII coat proteins are the least susceptible to modification, as large additions of amino acids inhibit virion assembly after cell infection.[42] Commonly, pIII minor coat protein genes are modified for recognition changes, as these represent the host-binding interaction side of the phage. This recognition capability allows for a wide range of applications from assembly and specifically tuned recognition motifs to peptide, protein, and antibody binding.[38]

Phage display is the process by which different biomolecules, especially short peptides, are presented on the pIII minor coat of the virus. These displayed peptides are randomized on different individual phage, to which >1 billion different sequences can be present in solution, representing a combinatorial library. This library can then be scanned for affinity to a target substrate.[37] Based on this incredibly large number of sequences, it is likely that a set of these peptides will specifically bind the target substrate. To begin the biopanning process, the phage are incubated with the desired substrate to initiate binding (**Figure 1.2**). The system is then washed to remove any unbound phage. Next, the bound phage are eluted from the target with a low-pH elution step, which reverses the binding and allows for collection and amplification.

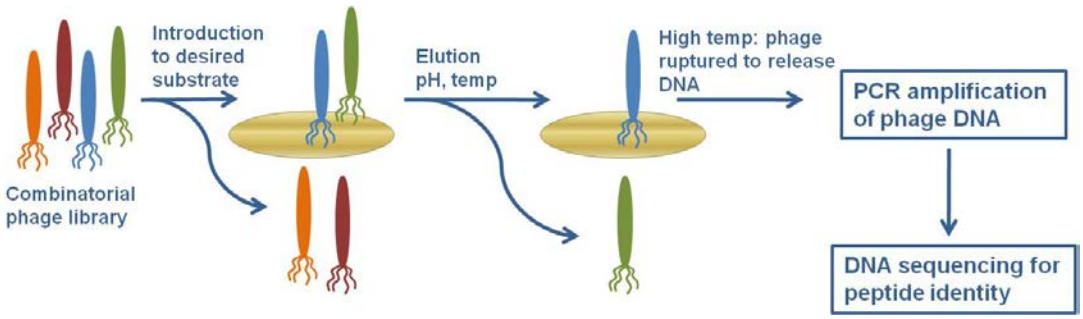

Figure 1.2. Phage display diagram of Naik *et al.* PCR-complemented procedure.[37]

These phage are then amplified by a bacterial host and then reintroduced to the target substrate. The process is repeated multiple times with increasingly stringent washes, thus only the most strongly bound phage remain. Typically, phage are collected after a fourth or fifth elution cycle, amplified, and their DNA is sequenced.[43] This DNA sequencing allows for gene identification and thus the pIII sequence identity of the substrate-binding peptide. Interestingly, those phage with the strongest substrate affinity may remain bound to the target surface and not identified. To account for this, Naik and coworkers have demonstrated that the bound phage can be ruptured directly on the surface, which releases their DNA.[37] From this, the released DNA can be amplified and sequenced, providing peptide sequences with the greatest surface affinities. This method and related selection processes allow for the isolation of peptides with affinities for a variety of materials, including Pd, Ag, Au, Fe_2O_3, TiO_2, and CdS.[22,23,36,37,44] Phage display is not predictive of sequences or binding motifs; however, the isolation of surface-specific peptides may provide valuable sequence information toward the rational design of materials-directing biomolecules.

1.3 Peptide Affinity and Self-Assembly

A number of amino acids are known to complex metal ions in solution and possess some interactions with metal surfaces.[45,46] Additionally, the placement of these moieties with respect to peptide or protein sequence has immediate consequences on the biotic/abiotic interface of a biomimetic surface, which directs material activity.[47] These metal-binding molecules have the potential to bind, passivate, and thus control inorganic surface properties. A number of systems employ the use of metal-specific peptides in materials synthesis, which can direct facet growth, resulting in size and shape control.[48,49] To this

end, the peptide-layered biotic-abiotic interface has the potential to dictate inorganic surface functionality, overall size, and shape, as a function of amino acid sequence. All of these structural characteristic work together to control the catalytic properties of inorganic nanomaterials, where the functionality can be readily tuned via structural changes.

Recently, Sarikaya and coworkers have focused on controlling the surface chemistry of carbon materials through the use of engineered, self-assembled peptides.[50] Rather than the covalent binding observed with thiols via cysteine, short peptides bind through combinations of weaker forces at multiple positions at the carbon-peptide interface. Additionally, graphene and carbon nanotubes have been used for a wide range of applications, including biosensing, due to their unique electronic properties.[51,52] While a number of functionalization techniques have been developed to control the surface of these materials,[53,54] it would be beneficial to preserve the intrinsic properties of graphene through less invasive surface methods that chemically damage the structure. A number of graphene-binding peptides have been previously identified and employed for bioinorganic nanomaterials synthesis and surface control.[54,55] To that end, Sarikaya and coworkers employed the dodecapeptide GrBP5-WT (IMVTESSDYSSY), due to the ordered and uniform molecular surfaces formed on graphene, seen in **Figure 1.3**.

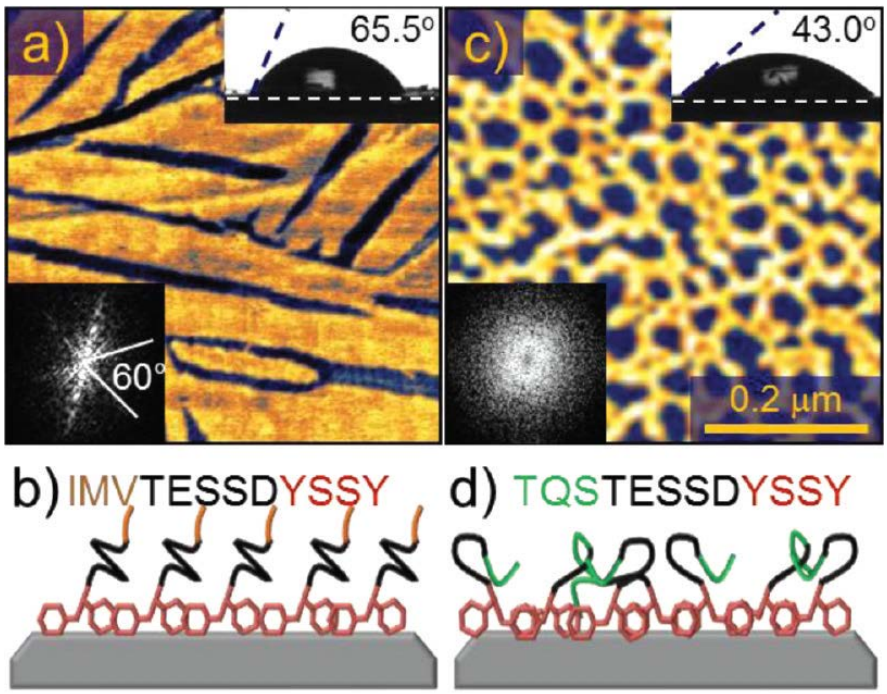

Figure 1.3. Hydrophobic and hydrophilic patterning on graphite of the indicated peptide sequences. The wild type sequence (b) corresponds to (a) the AFM image on the upper left while the hydrophilic (d) sequence corresponds to (c) the AFM on the upper right (reproduced from ref. 50 with permission).

It was found that self-assembly arises through a combination of binding among the aromatic rings of the two tyrosine residues on C-terminal region of the peptide likely through pi-stacking.[50] Additionally, substitution of the hydrophobic residues with hydrophilic ones inhibits formation of ordered peptide layers, causing the peptide layer to remain amorphous. To this end, the N-terminus was hypothesized to be responsible for patterning on the graphite surface. Based on these hydrophobic or hydrophilic residues, the wettability of graphite was controlled by varying the N-terminal sequence of GrBP5 in **Table 1.1**.

Peptide	Sequence	Mol. Mass
GrBP5-WT	IMV-TESSDYSSY	1381.4
GrBP5-Phob	LIA-TESSDYSSY	1335.3
GrBP5-Phil	TQS-TESSDYSSY	1354.3
SS-GrBP5	SSIMV-TESSDYSSY	1555.6

Table 1.1. Graphite-specific parent peptide GrBP5-WT and its modified analogues.

The main sequence of GrBP5-WT was maintained throughout for each peptide from the GrBP5-WT, while the ends were substituted as LIA, TQS, and SSIMV as hydrophobic, hydrophilic, and a SerSer addition, respectively. The SS-GrBP5 demonstrates that the tyrosines at the C-terminus are responsible for the graphite recognition and binding.[56] Wettability was characterized by the contact angle measurement of a macroscopic water droplet on the peptide-functionalized graphite surface. An effective transition threshold from amorphous to ordered phase was observed at 70% surface coverage. The measured contact angle of the macroscopic drop was recorded and observed to be greatly different as a function of the peptide sequence across similar surface coverage. To that end, these properties can be selectively tuned by small amino acid substitutions toward the ability to modulate inorganic surface availability.

Similarly, a peptide isolated with affinity for silica, QBP1 (PPPWLPYMPPWS), was employed in the self-assembly of nanocrystal quantum dots (QD) as a molecular linker.[57] To determine the binding immobilization of a silica-specific peptide, streptavidin-coated QDs (SA-QD) and biotinylated QBP1 (QBP1-bio) at the amine-terminated end of the peptide were used to functionalize QDs with the QBP1. The adsorption of these materials was characterized by QCM-D measurements, shown in

Figure 1.4. After an initial mass adsorption had been reached, a biotin buffer solution was added to all three systems. The resulting increase in frequency demonstrates the presence of biotin-SA binding, which leaches some material off of the QCM chips. Thus, both the SA-QD nonspecific interactions and SA-QD-to-functionalized-silica-surface interactions were overcome by biotin-SA binding after initial adsorption.

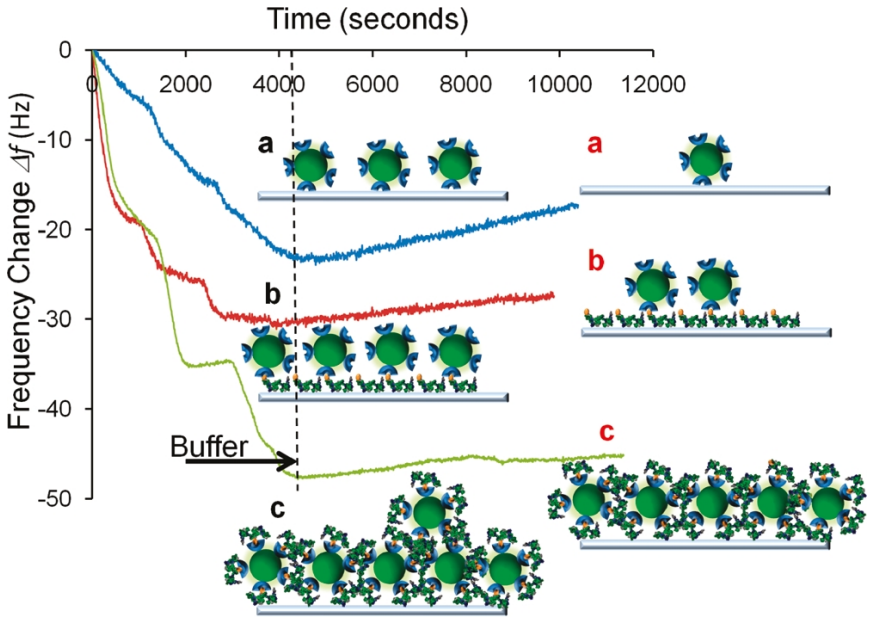

Figure 1.4. QCM-D analysis of the three QD systems with just SA-QD (a), SA-QD with QBP1-bio functionalized Si (b), and the nanoassembly QD (c) adsorption. A biotin buffer was added as indicated, resulting in slight decreases in adsorption to the surface (reproduced from ref. 57 with permission).

Analysis of these materials via binding affinity values demonstrates that the SA-QD with bio-QBP1 nanohybrid structure demonstrates the strongest binding to silica surfaces, as seen in **Table 1.2**. The hybrid assembly demonstrated a k_a value of 4.66 $\times 10^4$ $M^{-1}s^{-1}$, while the sequential assembly and SA-QD were observed to possess k_a values of 5.39 $\times$ 10^3 $M^{-1}s^{-1}$ and 0.60 $\times$ 10^3 $M^{-1}s^{-1}$, respectively.

kinetic constant	SA-QD	sequential assembly	nanohybrid assembly
k_a (M^{-1}/s)	0.60×10^3	5.39×10^3	4.66×10^4
k_d (s^{-1})	2.20×10^{-2}	6.40×10^{-2}	2.30×10^{-2}
K_{eq} (M^{-1})	2.56×10^4	8.43×10^4	2.03×10^6
ΔG (kcal mol^{-1})	−5.9	−6.7	−8.6

Table 1.2. Binding affinity values for the SA-QD, sequential assembly, and nanohybrid assembly for silica surface (reproduced from ref. 57 with permission).

The k_d values were roughly similar for all materials, resulting in K_{eq} values in decreasing order of nanohybrid > assembly > SA-QD. While the affinity of streptavidin for biotin is one of the strongest interactions known (4×10^{14} M^{-1}),[58,59] the binding abilities of short peptides are advantageous for nanomaterial passivation, surface control, and thus modulating inorganic material reactivity.[43] These processes only begin to characterize the biointerface of functional materials and biomimetic catalysts, which would allow further control over complex nanomaterials with superior properties through specific biotic/abiotic interactions. Additionally, a better understanding of these interactions could lead to the production of specialized materials, which are designed to possess improved catalytic reactivity.

1.4 Metallic Pt Bio-Nanomaterials

Peptide sequences have been shown to possess an affinity for specific inorganic surfaces, potentially even showing facet selectivity.[60,61] This is significant due to the high-energy edge and vertex atoms at the particle surface, which have been demonstrated to be highly active for catalytic applications.[62] Catalyst materials have typically been composed of transition metals.[63,64] Along these lines, nanomaterials have been designed by optimizing the exposure of these materials. Additionally, biological components have

been demonstrated to direct catalytic processes and control inorganic surfaces,[65] thus a certain biological-inorganic material synergy is possible. By passivating a nanomaterial surface with biologically active moieties, this synergy may lead to multifunctional catalytic materials.[66] These systems have been incorporated into nanocatalyst syntheses in various ways, with peptides coordinating metal ions prior to reduction, passivating the surface of the zerovalent materials, facilitating growth along specific planes,[48] combined motifs for linking/joining nanomaterials,[28] and functionalizing the surface of a nanomaterial with catalytically active groups and single atom metal-binding ligands.[21,67]

Platinum is commonly used as a catalyst in catalytic converters,[68] hydrogenation,[69] in the decomposition of hydrogen peroxide into water and oxygen,[70] and in oxidation/reduction reactions.[71] Traditionally, these methods typically involve bulk Pt black as a heterogeneous catalysts, which does not exploit the increased surface area possible through nanomaterial catalysts. The controlled synthesis of Pt nanomaterials could minimize wasted noble metal catalyst and increase catalytic turnover. To that end, Huang and colleagues have developed Pt nanocrystals with electrocatalytic activity through the use of Pt-specific peptides.[48] This peptide was obtained via phage display, through panning for sequences with an affinity for Pt metal.[48] From this selection process, a septamer sequence, BP7A (Ac-TLHVSSY-$CONH_2$, acylated on the N-terminus and with an amide functionality on the C-terminus), was obtained after the third biopanning cycle with an affinity for Pt wires. Pt nanocrystals were then synthesized in the presence of this peptide, with a controlled injection of $NaBH_4$, followed by the addition of ascorbic acid for slow reduction and selective facet growth. By varying the peptide concentration, particle shape was observed to be dependent on the BP7A

concentration. Water-dispersible nanocrystals formed in the presence of the peptide results in non-spherical materials termed mulitpods, in which a pod is growth along one facet. Of the materials produced in the presence of the BP7A peptide, linear growth occurs from the Pt crystal core along specific facets, resulting in single, bi, tri or tetra-pod shapes (**Figure 1.5**). Most pods were observed to grow along the <111> direction, while others were observed to grow in the <100> direction. Strangely, pods were not observed to grow in the <110> direction, which is uncharacteristic of the (111) < (100) < (110) energetic sequence of low index facets. Due to this observation, it is likely that the BP7A showed preferential binding to the (110) facets. At lower peptide concentrations, growth was observed along the (111) and (100) facets, while at higher concentrations, all facets were bound by BP7A, resulting in spherical shapes. TEM image analysis demonstrates that multipod NCs showed distinctive (110) facets as compared to spherical Pt nanocrystals.

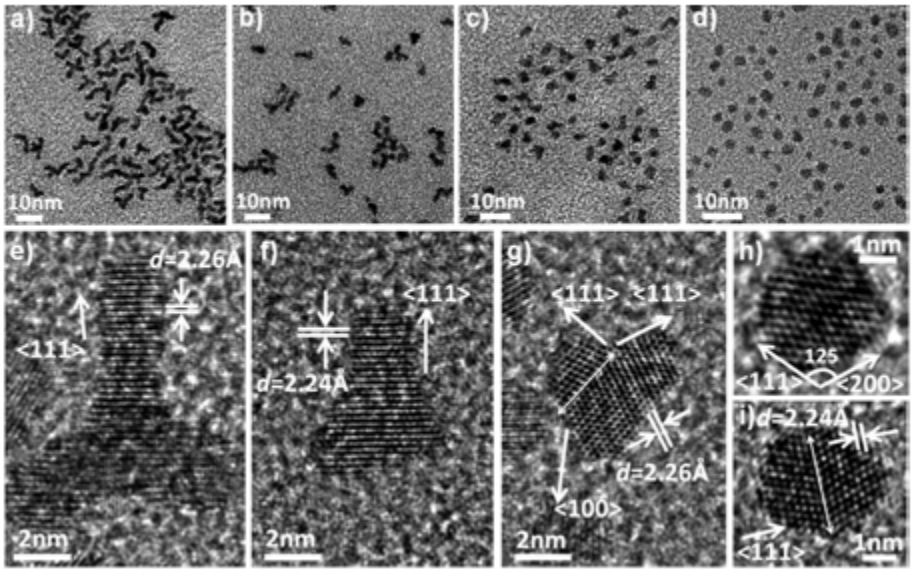

Figure 1.5. TEM analysis of Pt nanocrystal multipod structures with varying concentrations of BP7A peptide (22.5-250 μg/mL, a-d). Higher concentrations of peptide yielded more spherical particles, where lower concentrations of the peptide yielded

allowed for facet growth resulting in multipod structures (reproduced from ref. 48 with permission).

A correlation likely exists between the BP7A peptide sequence and the Pt nanocrystals pod growth, with facet selectivity driving the particle growth direction. This correlation between ligand and core material is likely responsible for the observed differences in nanocrystal size and shape. Due to the isolation of BP7A with affinity to Pt wires, some recognition of Pt facets (along the wire surface) may be present in the peptide sequence. Two amino acids, His and Tyr, are present that are known for their interaction with metals, such that their placement in a sequence may make a particular facet more energetically favorable. At lower peptide concentrations (22.5 μg/mL), the biotic/abiotic interface is less dense, as less overall peptide is bound to the surface. This surface motif leaves unbound facets open for continued particle growth to result in multipod formation. To this end, when a higher concentration of the peptide is present (250 μg/mL), more facets of the nanocrystal surface are bound and passivated, resulting in inhibited growth and spherical shapes.

Electrochemical studies were performed via cyclic voltametry (CV) to evaluate the electrochemical surface are (ECSA) of the multipods. Of these materials, the low-peptide concentration Pt crystals with a large number of pod growths were observed to possess the greatest ECSA. Additionally, the CV scans provided data that corresponded to H2 desorption/adsorption on (110) facets. This is consistent with the preferential growth binding mechanism of BP7A, in which the peptides preferably bind to and lower the surface energy of the (110) facet, resulting in growth on the (100) and (111) facets. As is expected for nanomaterials, shape deviation from spherical particles leads to an

increased surface area:volume relationship, while the materials synthesized with higher peptide concentrations possess lower ECSA values, more similar to Pt black standards.

Similar to the multipod structures in design, Huang and coworkers also isolated facet-specific peptide sequences via phage display to generate Pt nanocrystals of varying morphologies.[72] These techniques are significant for controlling surface structures, directing nanomaterial growth, and influencing the overall shape of the final materials. Shape-controlled nanomaterial growth is likely to be a kinetically directed process, in which low-energy facets persist.[73,74] While high-energy facets vanish, a particular shape is formed that is dominated by low energy surfaces. This effect is controlled by the design and employment of facet-specific ligands, which likely lower the overall facet energy to which they bind. This phenomenon results in selective particle growth, crystalline structure, and tunable shape control. Additionally, nanomaterial phase selectivity has been demonstrated through temperature control during materials annealing.[75] A nitride source was introduced to silicon nanowires and annealed at various temperatures. Kinetic growth competition was observed at nanoscale dimensions, which may help to further predict formation in other systems. Combined, these property controls are valuable, as the direction of shape, growth, and size can lead to increased activity of nanomaterials. Additionally, non-spherical nanomaterials are exceptionally valuable, due to the presence of high-energy edge and vertex atoms and a greater exposed surface area.[76] Peptides with an affinity for Pt were isolated by phage display, in which Pt cubes (with (100) facets) and Pt octahedra (with (111) facets) were deposited on silicon and used as the target surfaces. After three biopanning cycles, the remaining phage were eluted and sequenced for each system. Two peptides were obtained with an affinity for

these facets, septamers T7 (TLTTLTN) for the (100) and S7 (SSFPEPD) for the (111) Pt facets.[72] By employing these sequences in the presence of Pt^{2+} ions, non-spherical Pt nanomaterials were synthesized in both cases. For each synthesis, first $NaBH_4$ was added as an initial reductant, such that nucleation could occur. Next, ascorbic acid was added as a slower reductant, allowing for more controlled materials growth, in **Figure 1.6**.

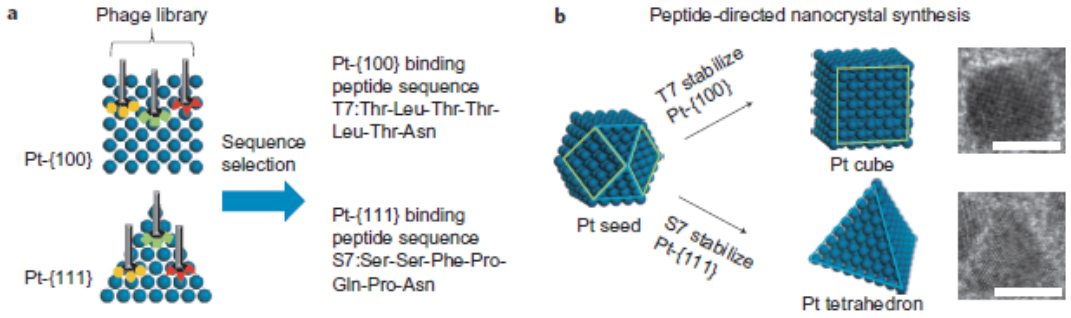

Figure 1.6. Shape-orienting Pt nanomaterials synthesis with a) phage display for plane-selective peptide sequences and b) plane-specific synthesis of Pt nanomaterials with T7 and S7 peptides. Scale bars are 20 nm (reproduced from ref. 71 with permission).

This dual-reductant method is employed to help control growth kinetics of the materials. To this end, a small amount of $NaBH_4$ is first consumed for the production of small seed crystals (~5 nm). The ascorbic acid then slowly reduces Pt^{2+} ions, which can then be added to higher energy, unbound facets, not inhibited by peptide binding. As expected, the T7 sequence resulted in the formation of cube structures (encased in 111 facets) and the S7 peptide produced tetrahedral nanoparticles (encased in 100 facets). Additionally, Huang and coworkers also performed this synthesis with varying single crystalline and twinned seeds.[49] This synthesis was repeated with Pt seeds generated with the multipod-forming BP7A peptide, to compare final material geometries. The BP7A peptide was observed to generated single-twinned seed crystals, which demonstrated different end materials. From these BP7A Pt seeds, right-bipyramids were produced in place of cubes,

indicating that growth still occurred along appropriate facets. To that end, the BP7A peptide assisted in formation of single-twinned seeds. These are shaped into right bipyramid and (111)-bipyramid by stabilizing (100) and (111) facets, depending on use of the T7 or S7 peptides, respectively. In the absence of BP7A peptide, single-crystalline seeds are produced, which then are grown into cubes and tetrahedrons, as seen in **Figure 1.7**.

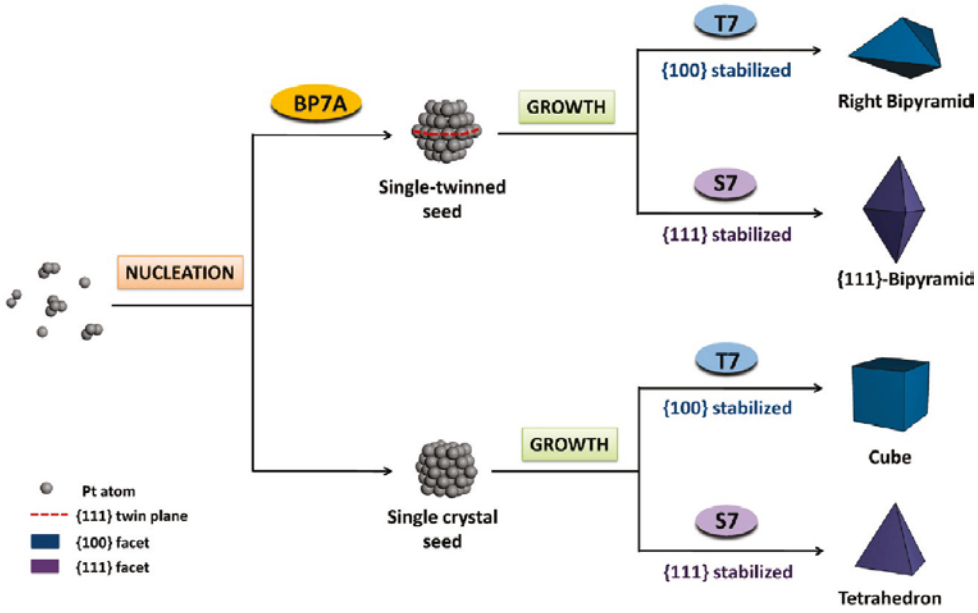

Figure 1.7. Materials synthesis diagram, dependent on BP7A-influenced seeds and sequence-stabilized growth facets (reproduced from ref. 49 with permission).

Similar to the multipod structures, the final particle shape was dependent on the presence of T7 or S7 used in the reaction. To confirm this growth mechanism, S7 peptide was added to a growth solution of T7-capped nanocubes, in which peptide concentrations were equivalent. The T7-capped nanocubes were observed to change shape to tetrahedral geometries, enclosed with (111) facets. This phenomenon suggests that the S7 affinity to (111) facets is greater than the T7 affinity to (100) facets. Due to the observed change in shape, it is likely that the S7 peptide more strongly binds the (111) facet, directing growth

to result in tetrahedron morphology. While these binding affinity value differences can be observed, a full understanding of the biotic/abiotic interaction is not yet fully realized. Likely, unique conformational structures of T7 and S7 and their hydroxyl-containing residues are responsible for facet selectivity. A more in-depth understanding of these binding and facet-specific effects could lead to the development of superior materials-directing peptides with multifunctional and improved catalytic activity.

1.5 Pd Biomimetic Nanocatalysts

Aside from Pt, Pd is a noble metal catalyst heavily used in hydrogenation,[77] dehydrogenation,[78] C-C couplings,[26] and as an electrocatalyst for the oxidation of alcohols.[79] Without catalytic Pd, these processes typically require high reaction temperatures and harsh organic solvents. Due to its wide range of functionality and harsh solution conditions, the development of Pd nanomaterials that function in ambient conditions is highly desirable. To that end, Pd materials would need to be prepared that are soluble in aqueous environments, are stable and passivated at ambient temperatures, but still possess accessibility to the particle surface.

In pursuit of surface-specific ligands, the Pd4 peptide (TSNAVHPTLRHL) was isolated via phage display with an affinity for Pd.[36] Through Monte Carlo simulations, this sequence was modeled to possess its strongest binding at the histidines at positions 6 and 11.[80] Other residues were also simulated to bind the surface, such as the asparagine and arginine residues;[80] however, they were reported to be weaker binders in the Pd4 sequence. From this structure simulation, it was modeled that the peptide likely forms a pinched structure on Pd surfaces, as seen in **Figure 1.8**.[80] In this case, reaction materials

could move near the nanoparticle surface, such that atom abstraction could take place between binding residues or under the unbound peptide.

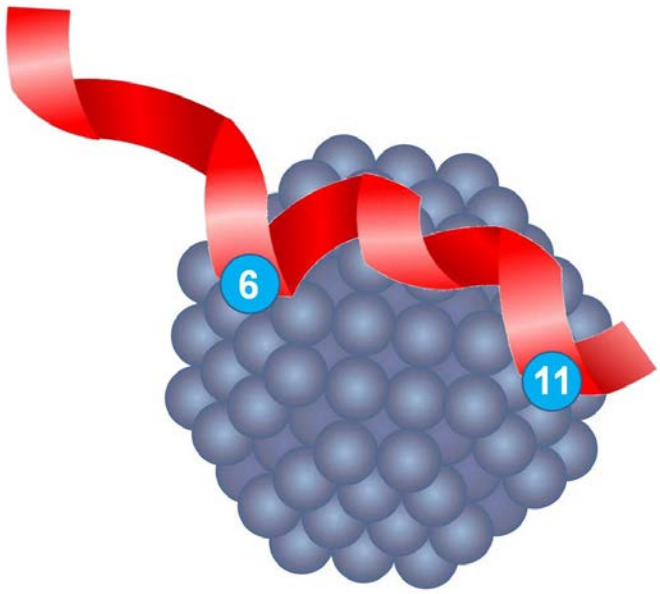

Figure 1.8. A possible pinched structure motif in which 6 and 11-position histidines bind the surface.

To that end, Pacardo *et. al.* synthesized nearly monodisperse 1.9 ± 0.3 nm peptide-capped Pd nanoparticles by reducing K_2PdCl_4 in the presence of Pd4.[26] These materials were demonstrated to be stable at room temperature, in water, and were observed to be highly active for the C-C coupling Stille reaction. In this process, the Pd4 peptide passivates the Pd nanoparticles, from which Pd atoms can be leached for oxidative addition. Next in the coupling, transmetallation occurs in a process involving an organostannane,[9] followed by reductive elimination to form the new C-C bond and release of a Pd^0 atom in **Figure 1.9**. These nanocatalysts were demonstrated to generate quantitative reaction product yields at catalyst loadings of 0.005% Pd mol over 24.0 h, which was performed at room temperature in water. For this reaction, a TOF value of 3207 ± 269 mol product (mol Pd × h)$^{-1}$ was reported.[26]

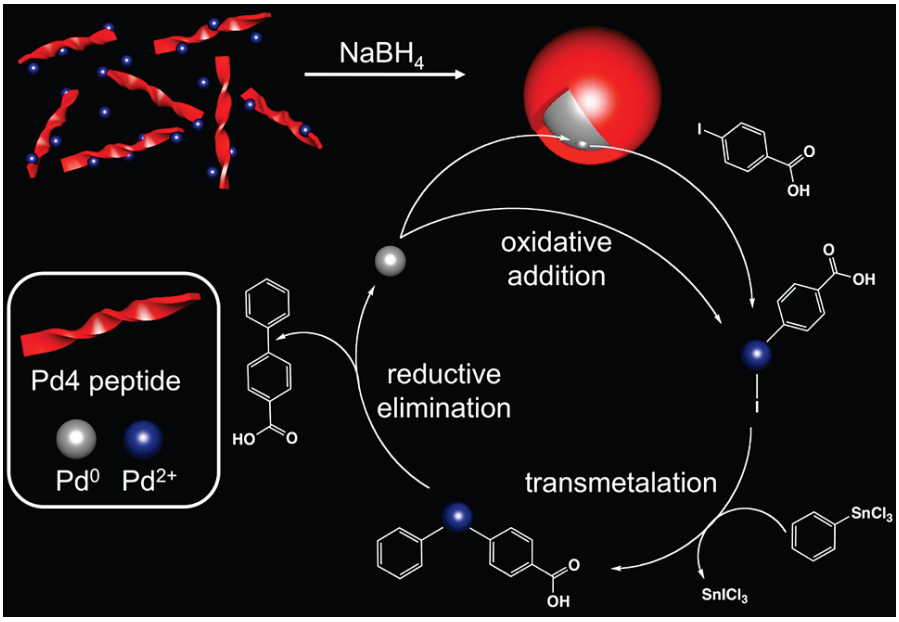

Figure 1.9. Synthesis of peptide-passivated Pd nanoparticles and their use as catalysts in the Stille coupling reaction (reproduced from ref. 26 with permission).

While the Pd4 peptide is capable of forming complexes with Pd^{2+} ions and passivating Pd biomimetic nanocatalysts, the exact binding mechanism by which Pd4 binds and passivates Pd surfaces is still unclear. Unfortunately, imaging techniques do not exist that can visualize biomolecules on inorganic surfaces.

While these materials are proposed to undergo an atom-leaching mechanism from the surface of the particles for the Stille coupling reaction, there has been some controversy in regard to the exact mechanism of catalysis.[81,82] Two suggested mechanisms exist, in that both an atom-leaching event and a surface-based reaction are possible. Pacardo *et. al.* have obtained evidence that supports the presence of a leaching mechanism for the Stille coupling reaction.[83] This work incorporated the use of Pd4-capped Pd nanoparticles, such that the Pd surface is covered with a layer of activity-

directing peptides. These materials were employed due to their optimal operating conditions in aqueous solutions and ambient temperatures (**Figure 1.10)**.

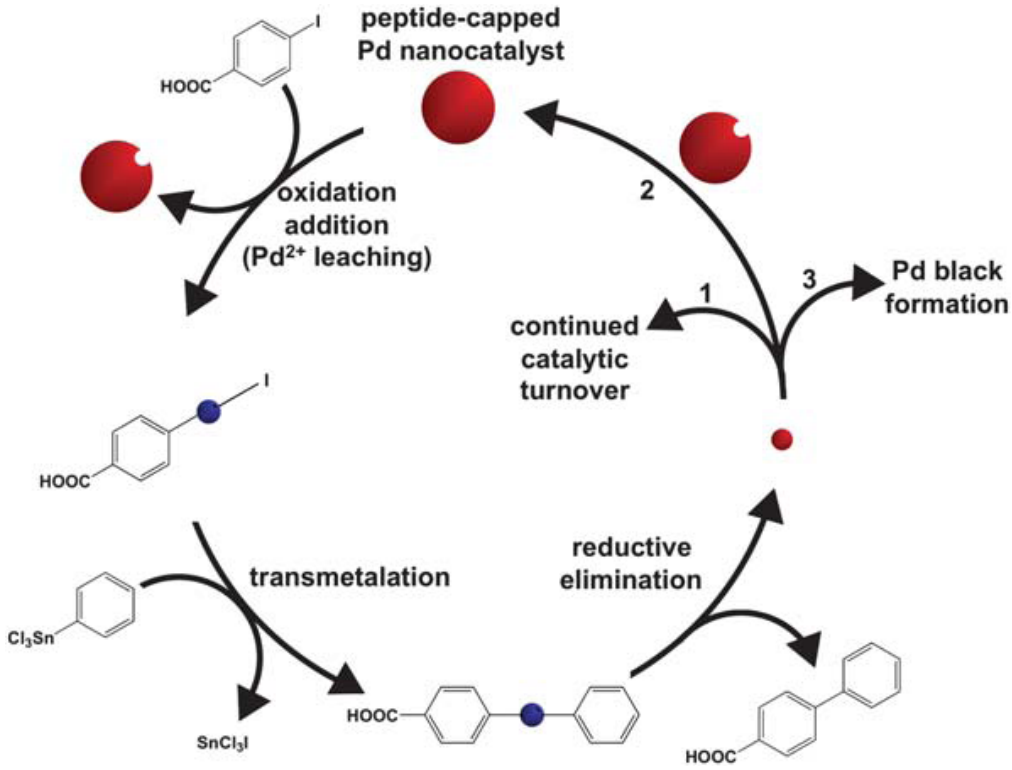

Figure 1.10. The atom-leaching Stille coupling of 4-IBA and phenyltin trichloride [Pacardo, D. B.; Slocik, J. M.; Kirk, K. C.; Naik, R. R.; Knecht, M. R. *Nanoscale* **2011**, *3*, 2194.] (Reproduced with permission of the Royal Society of Chemistry).

By comparing different reagents and Pd catalyst loading, it was observed that the Stille coupling reaction is highly sensitive to both Pd concentration and temperature. For example, a titration study demonstrated that increased Pd loading resulted in lower overall yields for the Stille coupling of 4-iodobenzoic acid with phenyltin trichloride in **Figure 1.11**.

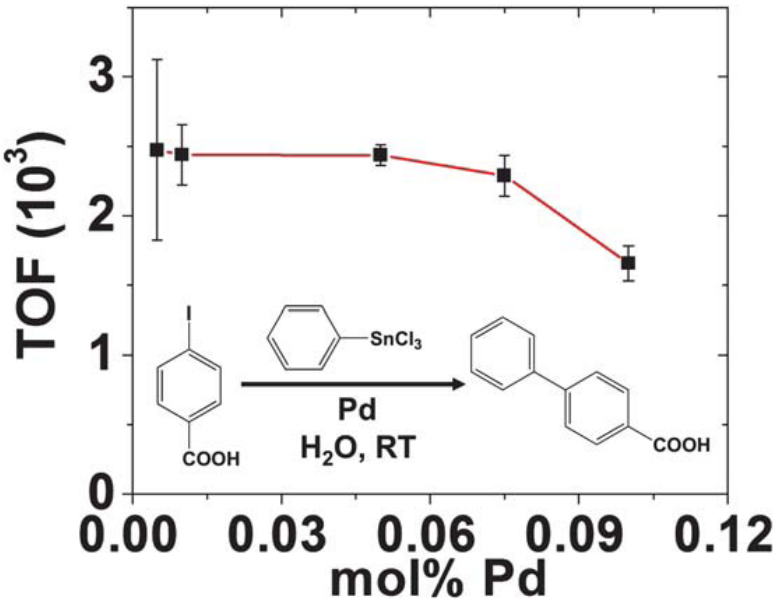

Figure 1.11. Pd loading analysis of the Stille coupling reaction with biomimetic Pd nanoparticles [Pacardo, D. B.; Slocik, J. M.; Kirk, K. C.; Naik, R. R.; Knecht, M. R. *Nanoscale* **2011**, *3*, 2194.] (Reproduced with permission of the Royal Society of Chemistry).

Surprisingly, the TOF is observed to decrease at loadings > 0.05 mol%. Prior to this catalyst loading, TOF values of ~2400 were consistently observed.[83] At Pd loadings higher than 0.05 mol%, the decrease in activity suggests that Pd aggregation may be favored, which is the formation of Pd black. This increased rate of Pd black formation would explain the decrease in TOF, as less free Pd^0 atoms are available to re-enter the catalytic cycle.

To complement this work, temperature studies were also performed in addition to varying reagents. In addition to 4-IBA as a starting material, both 4-bromobenzoicacid (4-BBA) and 4-bromophenol (4-BP) were employed in the coupling as less reactive starting materials. These materials lack the reactivity of iodine-containing aryl groups, due to the slower insertion of Pd in the aryl-bromide bond. To that end, reactivity

differences could be more easily distinguished with respect to temperature and starting reagents. Reactions were performed between 20 and 90 °C, over Pd loadings ranging from .005 – 0.1 mol%, in **Figure 1.12a,b**.

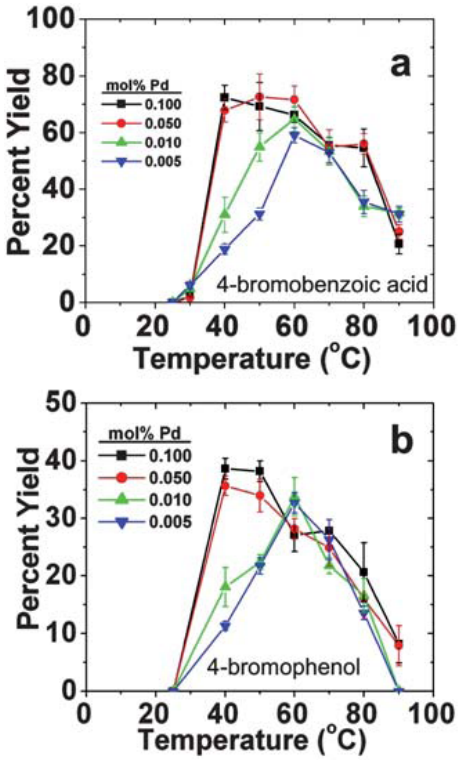

Figure 1.12. Temperature and loading studies of 4-BBA (a) and 4-BP (b) in the Stille coupling reaction [Pacardo, D. B.; Slocik, J. M.; Kirk, K. C.; Naik, R. R.; Knecht, M. R. *Nanoscale* **2011**, *3*, 2194.] (Reproduced with permission of the Royal Society of Chemistry).

As is evident for 4-BBA, a maximum yield (72.4 ± 4.3%) is achieved at 40 °C among higher loadings and maintained through 60 °C.[83] At temperatures > 60 °C, the yields are observed to decrease continually through 90 °C, where a value of 20.6 ± 3.5%% is noted. For the 4-BP, an early plateau is reached for higher loadings at 50 °C (38.7 ± 1.8%), while lower catalyst loading yields reach a maximum again at 60 °C. For both systems,

loading > 0.05 Pd mol% and > 60 °C demonstrated diminished yields for both reagents, which is likely due to Pd black formation.

To further test this possibility of substrate leaching and the presence of free atoms in solution, Quartz Crystal Microbalance (QCM) was employed with 4-IBA over a Pd-coated sensor. This measurement showed an increase in frequency (a loss of mass) for the Pd surface, indicating Pd atom leaching in the presence of the 4-IBA reagent. This increase in frequency is indicative of atom-abstraction via the oxidative addition step in the Stille coupling reaction (**Figure 1.13**).

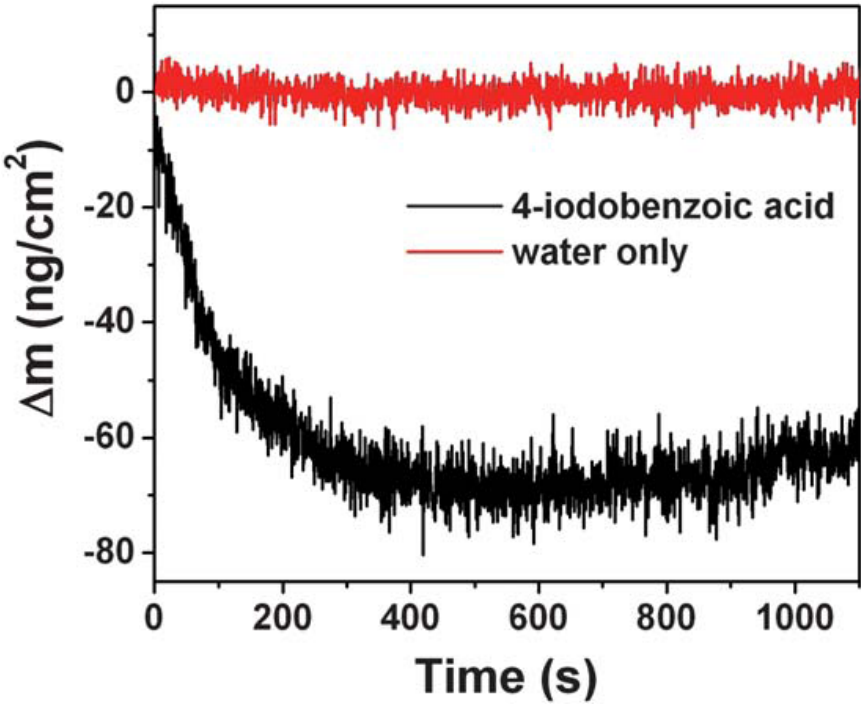

Figure 1.13. QCM analysis demonstrating the mass loss from a bare planar Pd surface during oxidative addition with 4-iodobenzoic acid. As a control, when no aryl halide reagent is added to the system, no change in the mass of the Pd surface is noted [Pacardo, D. B.; Slocik, J. M.; Kirk, K. C.; Naik, R. R.; Knecht, M. R. *Nanoscale* **2011**, *3*, 2194.] (Reproduced with permission of the Royal Society of Chemistry).

As is evident in **Figure 1.13,** mass is observed to decrease over time, with a maximum loss of mass observed at ~400 seconds. This gradual mass decrease is also indicative of oxidative addition, which is typically considered to be a slow step. At increased temperatures and Pd loading, Pd black formation is favored, which would compete with the catalytic reactions for the leached Pd atoms in the reaction mixture. Upon formation of Pd black, the catalytic activity of Pd^0 atoms decreases significantly, as atoms are buried and incredibly low surface area:volume ratios are likely.

In additional work, Pacardo *et. al.* also performed studies elucidating the reactivity leaching mechanism through reagent selectivity for the Stille coupling reaction with biomimetic nanocatalysts.[84] Stille coupling reactions with varying starting materials were performed at 0.05 mol% Pd loading, similar with previous reports. Differences in bond strength among aryl-halides are key to this study, as carbon-iodine is the weakest and demonstrates the greatest reactivity for this coupling.[85] From this, differences in oxidative addition at the Pd surface between aryl bromides and aryl iodides have been reported, while both undergo addition to free Pd^0 atoms in solution. While no reaction is observed with aryl bromides at room temperature with the Pd4-based Pd nanoparticles, these reagents have been observed to be active with Pd^0 leached atoms.[83] To that end, mixtures of these reagents were employed in the Stille coupling reaction (**Figure 1.22a**) with the intent that the aryl iodide would initiate the reaction by leaching Pd atoms. With Pd^0 atoms then released in solution, the aryl bromide could undergo oxidative addition and form C-C bonds, which is demonstrated in **Figure 1.14a**. The reaction was heated after a 2.0 h period to 40 °C, which demonstrated an increase in 4-bromobenzoic acid reactivity, seen in (**Figure 1.14b**).

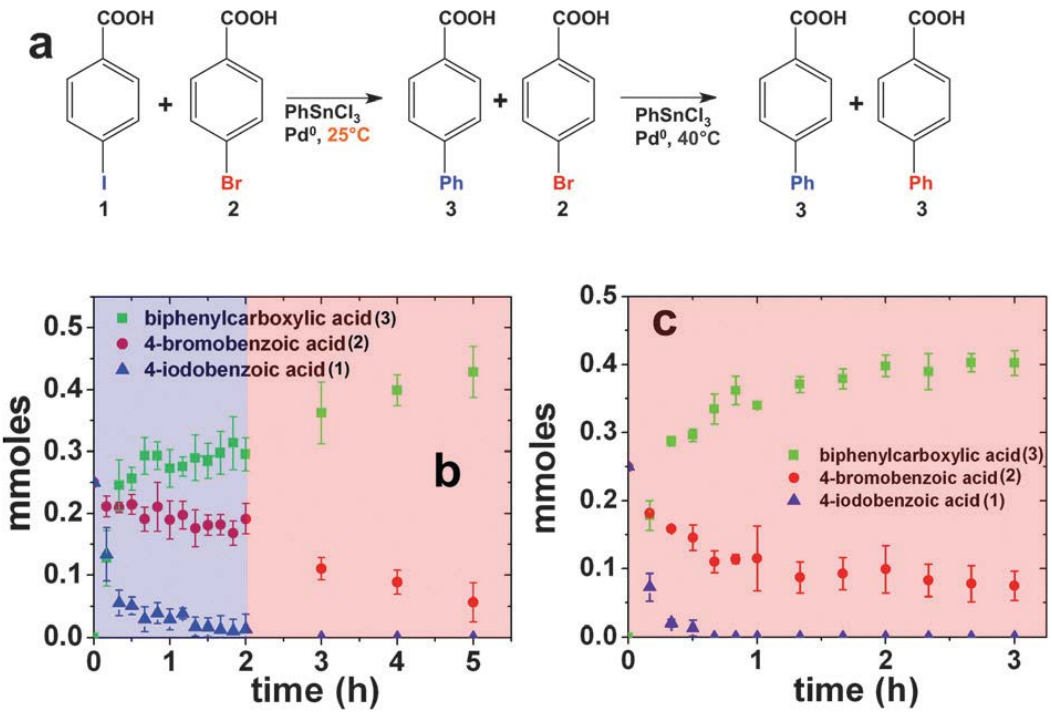

Figure 1.14. The proposed Stille coupling scheme (a) under which the initial reaction takes place at 25 °C and is increased to 40 °C at 2.0 h (b). The reaction is also carried out at 40 °C (c) as a comparison [Pacardo, D. B.; Knecht, M. R. *Catal. Sci. Technol.* **2013**, *3*, 745.] (Reproduced by permission of the Royal Society of Chemistry).

As seen in **Figure 1.14b**, the reaction is started at room temperature, which allows for the aryl-iodides to undergo oxidative addition and release free Pd atoms. When the reaction is heated to 40 °C, a significant increase in bisphenyl carboxylic acid (BPCA) was observed, which correlates to an immediate decrease in 4-BBA. This indicates that the 4-BBA is reactive with the free Pd^0 atoms in solution when heated to 40 °C. When the reaction is started at 40 °C (**Figure 1.14c**), reagent selectivity is lost as mixed reactivity is observed for both of the aryl-halides. Additionally, A similar study was performed with 4-IBA and 4-chlorobenzoic acid (4-CBA).[84] Similar results were observed, but 4-CBA required temperatures of 60 °C for quantitative yields.

Finally, di-substituted aryl halides were employed in the Stille coupling reaction at 25 °C, through the use of 3-bromo-5-iodobenzoic acid.[84] This reagent contains both an iodide for Pd leaching and a bromide for reaction with the free Pd^0 atoms. Ideally, the iodide would undergo coupling first and eject a Pd^0 atom with one catalytic cycle. Next, the bromide could then react with the free Pd^0 atom, producing 3,5-diphenylbenzoic acid (**Figure 1.15a**). The use of this reagent produced an intermediate, in which 3-bromo-5-phenylbenzoic acid was observed (**Figure 1.15a**).

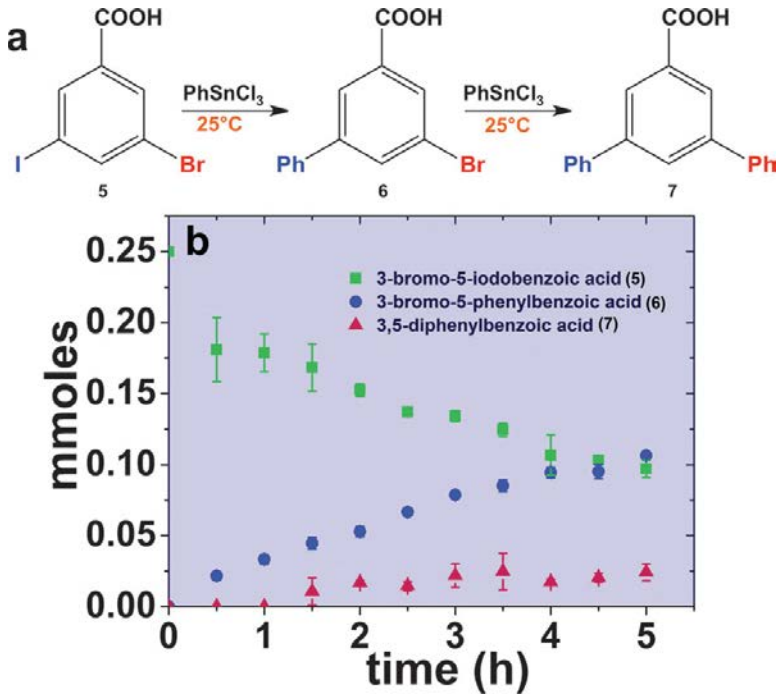

Figure 1.15. A disubstituted Stille coupling analysis scheme (a) with both bromo and iodo halogens and the reaction analysis (b) over 5.0 h [Pacardo, D. B.; Knecht, M. R. *Catal. Sci. Technol.* **2013**, *3*, 745.] (Reproduced by permission of the Royal Society of Chemistry).

From this, products were analyzed over 5.0 h, showing the decrease of starting materials and production of both the intermediate and final material, 3,5-diphenylbenzoic acid (**Figure 1.15b**). It should be noted that no 3-iodo-5-phenylbenzoic acid was detected,

suggesting that oxidative addition is dependent on the halogen identity. After allowing the reaction to proceed for 24.0 h at 0.05 mol% Pd, products were quantified at 70.8 ± 0.9% of intermediate and 22.1 ± 2.5% of the 3,5-diphenylbenzoicacid (3,5-DPBA). This suggests that the iodo halogen preferentially undergoes Stille coupling at 25.0 °C, leading to the intermediate product. Surprisingly, the minor generation of the di-substituted product at low temperatures suggests that the phenyl group may activate the remaining bromo for oxidative addition and eventual Stille coupling.

Taken together, these studies suggest that the di-substituion of aryl groups leads to somewhat lower activity for the aryl-iodide coupling; however, this reagent demonstrated higher bromo- activity, likely due to C-Br activation for eventual Stille coupling. This suggests that coupling of di-substituted aryl compounds results in changes to the electronics of the system. The electron-donating phenyl ring in the intermediate may activate the bromine position, weakening the C-Br bond and promote coupling and formation of the di-substuted product. This work suggests that thermal or electronic activation is required for the C-Br bond to undergo Stille coupling. These requirements demonstrate precise conditions over which reagent selectivity can be tuned for Pd nanocatalyst materials. The activity data reflects C-halogen bond strength with respect to starting material reactivity, while also outlining reagent selectivity and possible modes of activation. Most importantly, these reactions provide valuable insight into the Stille coupling mechanism, which would be valuable for optimizing catalyst-based, energy-efficient systems.

1.6 Peptide-Capped Multicomponent Nanomaterials

Though monometallic nanoparticles possess well-known catalytic activity, combinations of noble metals with electronegativity differences have been demonstrated to possess increased catalytic activity as compared to single-material systems.[28,86] A more electronegative element under a catalytically active one has been demonstrated to increase overall activity of the exposed metal component.[87] Bimetallic catalysts have been demonstrated with AuPt,[88] AuPd,[89] MnCu,[90] PdCu,[91] and CuRu[92] materials with core-shell,[93] nanowire,[41] and other geometries.[94] This increase in activity is proposed to be a function of two different effects- electronic changes in the system and changes in geometric configuration of metal atoms in the material.[95] These electronic changes likely occur through differences in electronegativity among metals, such that an underlying metal may cause a surface metal to be more electrophilic in catalysis. Additionally, variations in geometric configuration can easily take place with different atomic radii, causing changes in electronegativity as a function of coordination environment.[96]

Bicomponent nanocatalysts have been prepared using a multifunctional materials-binding peptide based upon two sequences known to bind noble metal nanoparticles.[28] For this, the A3 peptide (AYSSGAPPMPPF) isolated with an affinity to Au was integrated into a single sequence with the Flg (DYKDDDDK), which was also known to bind noble metal particles. With these two components, a single, multifunctional fusion peptide was generated to form the Flg-A3 sequence.[28] Interestingly, the order of the sequences directly affect material binding, where positioning of the Flg and A3 regions at the N- and C-terminal portions were required to optimized material binding for nanoparticle formation in **Figure 1.16**. For this, the A3 region was anticipated to bind to

Au nanoparticles, thus displaying the Flg region, which exposes multiple aspartic acid moieties to solution to bind Pd^{4+} ions. Au nanoparticles were formed by the combination of the FlgA3 peptide with Au^{3+} ions in a HEPES buffer and incubated for 30 min, which resulted in Au nanoparticles. To a solution of the resulting, purified Au nanoparticles was added Pd^{4+} and sodium borohydride, which created the ~3.0 nm Pd nanoparticles attached to the original Au materials via FlgA3.

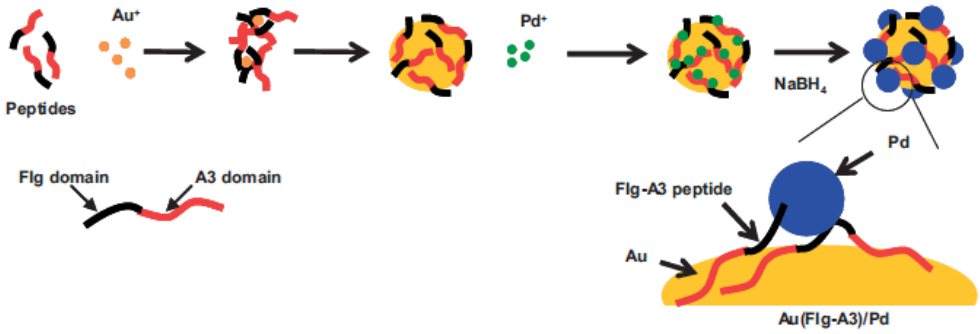

Figure 1.16. Synthesis scheme of Pd nanoparticles synthesisized at Au nanoparticles with the Flg-A3 fusion peptide (Reproduced from ref. 28 with permission).

TEM analysis of the bimetallic materials reveals the formation of Au nanoparticles encircled with smaller Pd nanoparticles at the surface, as shown in **Figure 1.17a**. Prior to Pd nanoparticle production, the Flg-A3-capped Au nanoparticles were observed to be 10.7 ± 0.6 nm. The overall diameter increased to 15.5 ± 3.9 nm after Pd nanoparticle incorporation due to the presence of the smaller Pd particles at the Au nanoparticle surface. Visible in **Figure 1.17b**, various lattices are distinguishable on the surface of the Au nanoparticle, which is indicative of the smaller Pd nanoparticles at the gold surface.

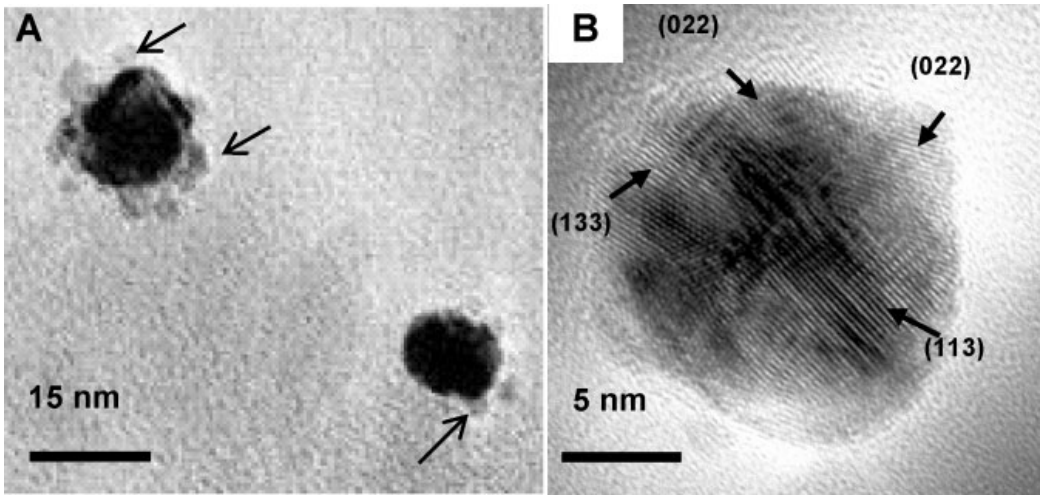

Figure 1.17. TEM images of the bimetallic PdAu NP. These include the smaller Pd NP encircling AuNP (a) and the different crystal lattices of Pd around Au (b) (Reproduced from ref. 28 with permission).

With this combination of metal species, a catalytic increase was observed via the surface Pd nanoparticles. The more electronegative Au metal has been demonstrated to pull electron density from the surface Pd particles, thus increasing their catalytic reactivity for olefin hydrogenation.[89,97] To determine if such effects were observed from the biomimetic bimetallic materials, their activity was tested via the hydrogenation of 3-buten-1-ol to 1-butanol. With the peptide-capped materials, a TOF value of 1016 mol product (mol Pd × h)$^{-1}$ was observed, which is greater than double the value observed when using commercially available Pd nanoparticles under the same reaction conditions. As such, increased reactivity was observed, indicating an intimate contact between the two metallic components to drive the optimized functionality. This indicates that the biomolecules can be used to guide material production without adversely inhibiting the desired final activity.

In a second study, the Flg-A3 peptide was employed by Slocik *et. al.* for the synthesis of Pt-CdS nanomaterials as a non-natural mimic of the enzyme nitrate reductase.[86] This enzyme is known to reduce nitrate to nitrite, which is important for the development of biomimetic systems,[98] as this system was demonstrated to be >23 fold more active than the enzyme nitrate reductase. For these studies, the Flg-A3 peptide was modified by the addition of a cysteine residue at the C terminus, yielding Flg-A3C. The thiol functional group caps the growth of the CdS quantum dots, with the remainder of the peptide exposed to solution for Pt nanoparticle production, as shown in **Figure 1.18**.

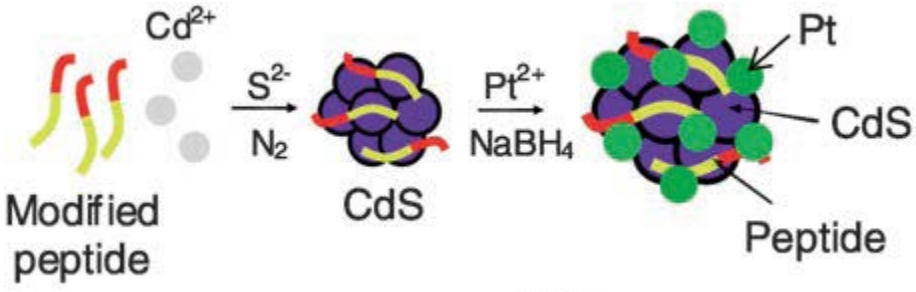

Figure 1.18. Synthesis scheme of Pt-CdS biotemplated nanoparticles (Reproduced from ref. 85 with permission).

After introduction to Pt^{2+} ions and reduction, the multicomponent materials are generated, which were observed to possess a chain-like structure, though the reason for this assembly is unclear. These materials are consistent with other Pt materials produced, with sizes of 13 nm for the CdS materials, 1.5 nm for that of the Pt nanoparticles, and ~15 nm for the overall nanoassemblies via TEM imaging in **Figure 1.19**.[86] The assembly of this multi-component nanomaterial is likely controlled by the peptide domain interaction while bound to the quantum dot via thiol-binding.

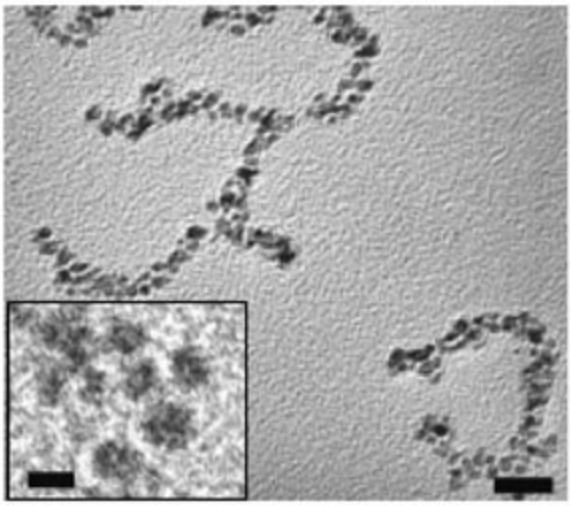

Figure 1.19. TEM analysis of the Pt-CdS nanomaterials. Scale bars are 13 nm and 4 nm for the inset (Reproduced from ref. 85 with permission).

The Pt and CdS proximity via Flg-A3C can elicit rapid electron transfer upon exposure to UV light, which proceeds to complete nitrate reduction. Furthermore, the tyrosine residue in each A3 domain can act as an electron donor for the CdS surface holes, eliminating the need for another electron donor.

After TEM analysis, the Pt-CdS materials were employed as catalysts for nitrate reduction, which can be readily monitored via UV-vis. This is achieved by monitoring the 431 nm wavelength for fluorescent intensity, which is indicative of nitrite production.[86] From this study, the activity of the excited (250 nm) multicomponent Pt-CdS materials was observed to be at least 20 times greater than the activity of an original nitrate reductase enzyme for the same reaction. As controls, two other materials were tested for reactivity, including the excited CdS nanoparticles and the Pt-CdS system without excitation. Among these systems, the excited Pt-CdS nanoassemblies were observed to possess the highest activity with 3.7×10^4 mol NO_2^-/g catalyst, even beyond that of the nitrate reductase enzyme, in **Figure 1.20**. Additionally, a final control of just

Pt nanomaterials showed no nitrate reduction activity at all, demonstrating the need for the semiconductor materials. These results suggest that the overall proximity of the Pt materials to the CdS surface and photo-excited hole/electron interaction plays a vital part in the increased nitrate reduction activity.

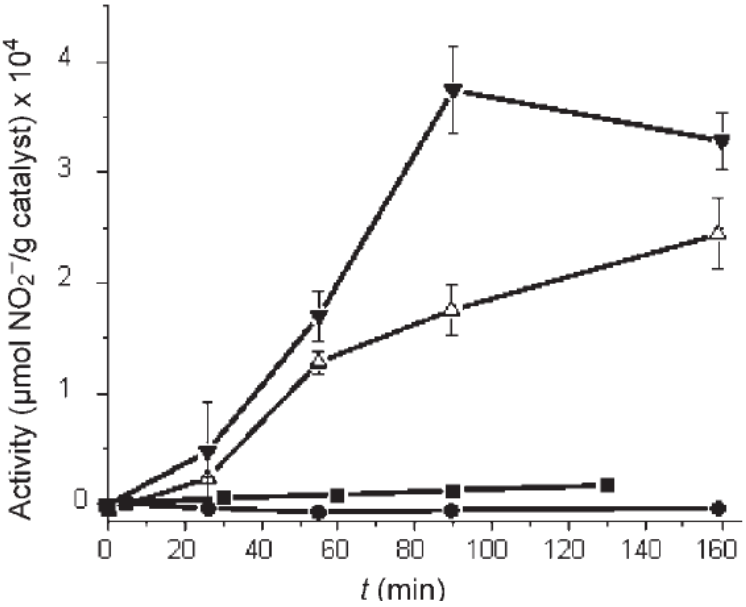

Figure 1.20. Activity comparison for various systems for the reduction of nitrate with Pt-CdS (▼), CdS nanoparticles (Δ) when excited at 250 nm, nitrate reductase (cofactor added) enzyme (■), and Pt-CdS nanoparticles without excitation (●) (Reproduced from ref. 28 with permission).

Similar activites were observed between the enzyme (with cofactor) and the Pt-CdS quantum dots (without excitation). The incorporation of the Flg-A3C peptide allowed for the combination of smaller Pt nanoparticles and the CdS quantum dots. With these nanoassembly materials, the highest activity of 3.7×10^4 mol NO_2^-/g catalyst was observed with excitation, which was demonstrated to be higher than the CdS excited quantum dots (1.5×10^4 mol NO_2^-/g catalyst). The addition of the smaller, Pt nanoparticles at the CdS surface lead to increased activity, due to material proximity and sequence identity. This is likely due to the presence of tyrosine and the role it plays in

electron shuffling. This nanoassembly demonstrates that peptides can be used to generate systems in which an advantageous proximity can be modulated between materials, further enhancing their functionality. This provides multiple solutions to CdS catalysis shortcomings,[99] such that higher activity is observed while the necessity of electron mediators is not necessary for these quantum dots.

1.7 Pd Bio-Nanoparticle Networks

In addition to spherical, peptide-capped nanoparticles, Bhandari *et. al.* have reported on nanoparticle networks, templated by the R5 peptide.[25,100,101] This sequence is a derived from the repeat units of the NatSil gene of the diatom *Cylindrotheca fusiformis*.[102] Known for the production of titania and silica, the R5 peptide sequence possesses an RRIL motif which facilitates biomolecular self-assemble to form a large 3D scaffold.[103] With this peptide sequence, a variety of Pd nanoscale morphologies can be synthesized, ranging from spheres and ribbons to nanoparticle networks.[25] The Pd systems were observed to be loading-dependent, as illustrated in **Figure 1.21a-c**. At Pd:peptide ratios of 60, 90 and 120, stable nanostructured materials were observed; however, at ratios of 150 and above bulk precipitation was noted. In solution, these bioscaffolds first self-assemble into larger constructs. Next, the Pd^{2+} ions are complexed within the bioscaffold through individual LMCT interactions. The internal peptide assembly acts as a template for the metal nanoparticles, in addition to stabilizing the final materials against aggregation via encapsulation. From this approach, nanomaterial morphologies ranging from spherical nanoparticles and fused ribbons to large 3D

nanoparticle networks can be achieved based upon the Pd:R5 ratio employed during the synthesis.

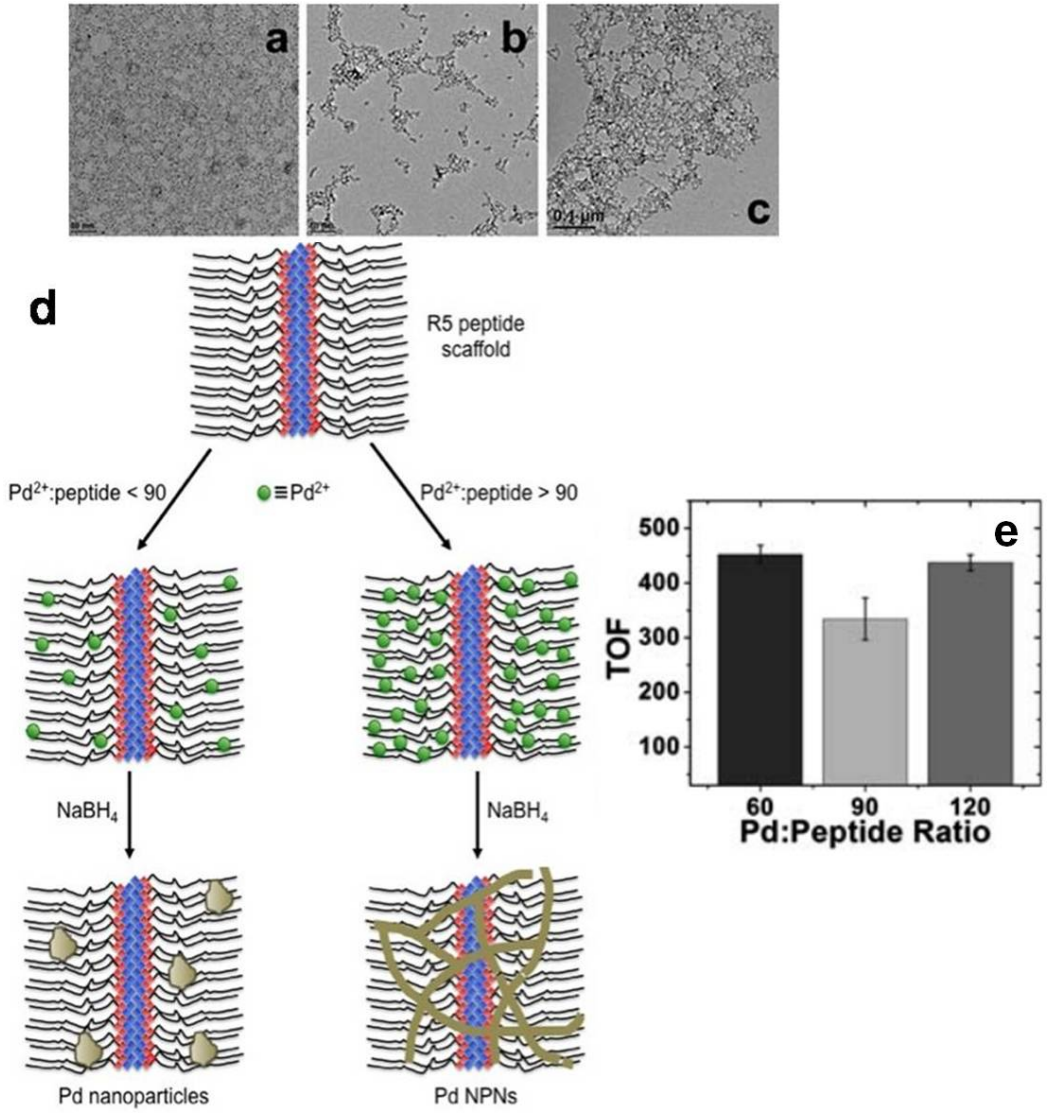

Figure 1.21. TEM images of a) 60, b) 90, and c) 120 Pd:peptide ratio Pd nanostructures, (d) the proposed mechanism of their formation, and e) their catalytic activity in the Stille coupling reaction [Jakhmola, A.; Bhandari, R.; Pacardo, D. B.; Knecht, M. R. *J. Mater. Chem.* **2010**, *20*, 1522.] (Reproduced by permission of the Royal Society of Chemistry).

From TEM image analysis, particle sizes were observed to be 2.9 ± 0.6 nm, 3.9 ± 0.8 nm, and 4.1± 1.2 nm for the Pd 60, 90, and 120 materials, respectively (**Figure 1.21a-c**). HR-

TEM images revealed various lattices which shows the ribbons and nanoparticle networks to be polycrystalline, where single nanoparticles were initially formed and fused together, depending on particle proximity (**Figure 1.21d**). Once the materials were characterized, they were employed as catalysts for the Stille coupling reaction. Here, activities were observed to be dependent on the bioscaffold present from R5, with values of 452.4 ± 16.4 mol product (mol Pd × h)$^{-1}$, while the other systems demonstrated TOF values of 334.3 ± 38.3 mol product (mol Pd × h)$^{-1}$ and 437.1 ± 14.3 mol product (mol Pd × h)$^{-1}$, for Pd90 and Pd120 materials, respectively (**Figure 1.21e**).[25]

For each system, the metallic catalyst is contained within the peptide bioscaffold. Spherical particles are observed in the Pd60 materials, which are likely to possess the greatest surface area and demonstrate a comparatively higher TOF value. For the Pd90 materials, a decrease in activity is observed, likely due to a loss in Pd surface area. Finally, an increase in activity is observed for the Pd120 materials, which does not follow the previous surface area trend. This final increase is likely a function of the self-assembled structure reaching Pd saturation, such that the fused nanoparticle networks are closer to the assembly surface. With a greater loading of Pd materials in the bioscaffold, a more shallow penetration depth is required for oxidative addition of the starting materials, which resulted in higher TOF.

While the R5 peptide demonstrates a self-assembled structure to template Pd nanomaterials, the effect of the peptide sequence and assembly structure with respect to the synthesis and eventual properties is not fully understood. Two factors contribute to the catalytic activity of this system- inorganic surface area and reagent diffusion through the bio framework. As such, modulation of these factors could be used to optimize the

reaction efficiency. To probe this effect for template changes, Pd materials were synthesized employing four peptide truncates of the R5: T1 (SSKKSGSY), T2 (SGSKGSKRRIL), T1A (SSKKSGSYRRIL), and T2A (SGSKGSK).[101] The first two peptides were obtained by cleaving the R5 peptide at the tyrosine residue, thus isolating the RRIL motif in the T2. Additionally, the T1A and T2A sequences are modifications of T1 and T2, with and without the RRIL motif at the C-terminus, respectively. Each of these peptides were employed to form stable materials at 30, 60, and 90 Pd:peptide ratios. These resulting Pd nanomaterials were characterized via TEM analysis and tested for catalytic activity in the Stille coupling reaction. At the lowest Pd loading, the nanomaterials were observed to be spheres of single-crystalline domains within the bioscaffold. At ratios of 60, some material elgonated and nonspherical morphologies were observed, with larger nanoparticle diameters as compared to the materials prepared with a Pd:peptide ratio of 30. For the materials prepared at a ratio of 90, mostly fused nanoparticle networks were observed, with higher diameter dimensions. TEM images of the Pd materials prepared with each peptide in 30, 60, and 90 Pd:peptide ratios is presented in **Figure 1.22**. Unlike previous work, the materials prepared at a Pd:peptide ratio of 120 aggregated, thus the 30 ratio was included in the study.

Various material morphologies prepared with T1 were observed to be 3.2 ± 0.8 nm (spheres), 3.1 ± 0.7 nm (elongated materials), and 4.3 ± 0.6 nm (networks) for Pd:peptide ratios of 30, 60, and 90, respectively. Materials prepared with the T2 peptide were observed to be 3.0 ± 0.5 nm (spheres), 3.7 ± 0.6 nm (nanoribbons), and 4.2 ± 0.6 nm (networks) for ratios of 30, 60, and 90, respectively.[101] The materials prepared with T1A, (with the added RRIL motif) demonstrated sizes of 3.4 ± 0.7 nm (spheres), 4.0 ± 0.5 nm

(nanoribbons), and 5.2 ± 0.7 nm (networks) for materials prepared with ratios of 30, 60, and 90, respectively.

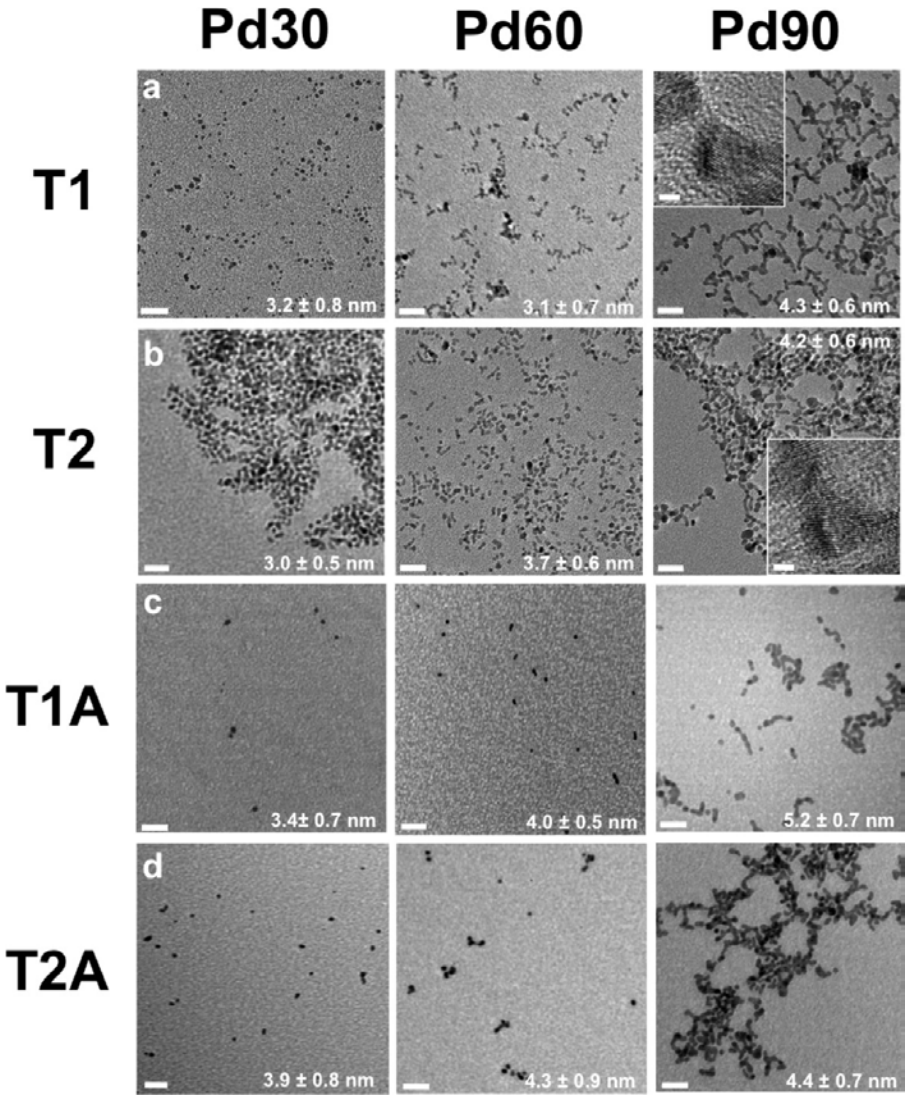

Figure 1.22. TEM analysis of materials prepared with a) T1, b) T2, c) T1A, and d) T2A peptides at 30, 60, and 90 Pd:peptide ratios. Regular scale bar is 20 nm and inset scale bar is 2 nm (Reproduced from ref. 100 with permission).

For the materials generated with the T2A (without RRIL), sizes of 3.9 ± 0.8 nm (spheres), 4.3 ± 0.8 nm (larger spheres), and 4.4 ± 0.7 nm (networks) were observed for ratios of 30, 60, and 90, respectively. It should be noted that these materials were very

similar in morphology with respect to Pd:peptide ratios, which suggests a similar mechanism for the assembly of these systems. It is surprising that all truncates were responsible for stable materials, as the RRIL motif is missing from the T1 and T2A peptides. Here, DLS sizing analysis was performed on the Pd^{2+}-complexed bioscaffolds, which demonstrated an increasing size trend with respect to increased Pd^{2+} loading. These sizing results indicate that all peptides can assemble into bioscaffolds, independent of the RRIL motif; however, the peptides that contain RRIL were observed to form larger templates. This suggests that the RRIL does participate in self-assembly, but other factors in peptide sequence can also drive self-assembly. To that end, there is a high similarity between truncate sequence identity, such that similar behavior could be expected.

To probe the reactivity of materials prepared with these truncates, the twelve different systems were employed as catalysts in the Stille coupling reaction of 4-IBA and $PhSnCl_3$. TOF analysis of the materials is shown in **Figure 1.23**.

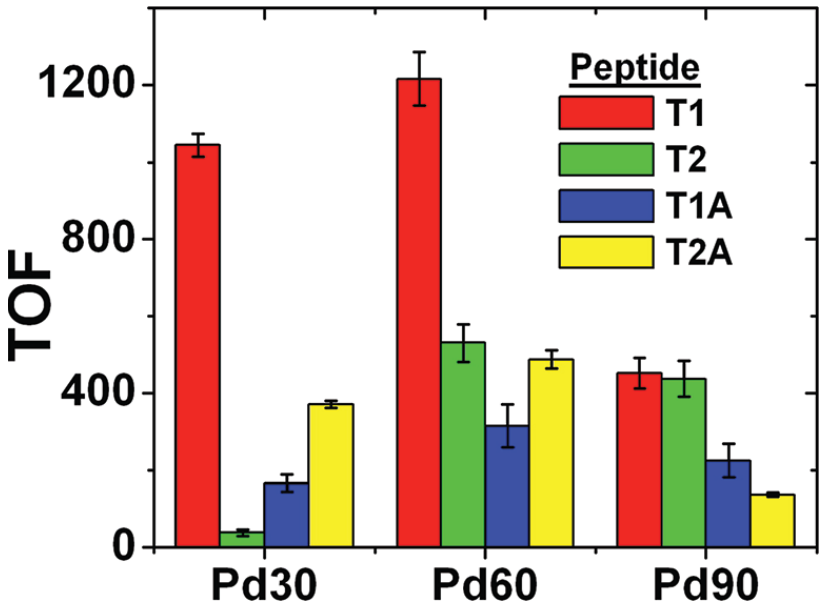

Figure 1.23. TOF analysis of the peptide truncates in Pd:peptide ratios of 30, 60, and 90 (Reproduced from ref. 100 with permission).

The materials prepared with T1 peptide showed a two-to three-fold increase in reactivity among the 30 and 60 Pd:peptide ratios, with TOF values of 1030 ± 26 mol product (mol Pd × h)$^{-1}$ and 1215 ± 70 mol product (mol Pd × h)$^{-1}$, respectively. Additionally, a lower TOF value of 451 ± 40 mol product (mol Pd × h)$^{-1}$ was observed for the T1-Pd90 NPNs. For the T2 materials, TOF values of 38 ± 9 mol product (mol Pd × h) $^{-1}$, 530 ± 49 mol product (mol Pd × h) $^{-1}$, and 437 ± 46 mol product (mol Pd × h) $^{-1}$ were observed for ratios 30, 60, and 90, respectively. The materials prepared with T1A demonstrated TOF values of 166 ± 23 mol product (mol Pd × h) $^{-1}$, 315 ± 56 mol product (mol Pd × h)$^{-}$1, and 224 ± 44 mol product (mol Pd × h)$^{-1}$ for ratios 30, 60, and 90, respectively. Finally, the materials prepared with T2A demonstrated TOF values of 166 ± 23 mol product (mol Pd × h)$^{-1}$ for the spheres, 315 ± 56 mol product (mol Pd × h)$^{-1}$ for the elongated spheres, and 224 ± 44 mol product (mol Pd × h)$^{-1}$ for the networks for ratios 30, 60, and 90, respectively. Due to the structural similarity of the Pd components for each system, the differences in the peptide scaffold are likely responsible for the variations observed in catalytic activity.. This scaffolding effect may allow greater access to the Pd materials, in which the T1 peptide self-assembly is more permeable than the other three sequences.

Beyond Pd-based materials, the R5 peptide has demonstrated the ability to form networked Au nanomaterials that are catalytically active.[100] Such Au nanoparticle networks have become of interest due to their high metallic surface area, tunable optical properties, and large frameworks for a variety of applications.[104] Both the functionality and net reactivity of these materials typically depend on the initial size of the Au particles and their passivant identity;[18] however, recent biomimetic synthesis approaches have allowed for their production with peptides (**Figure 1.24**).

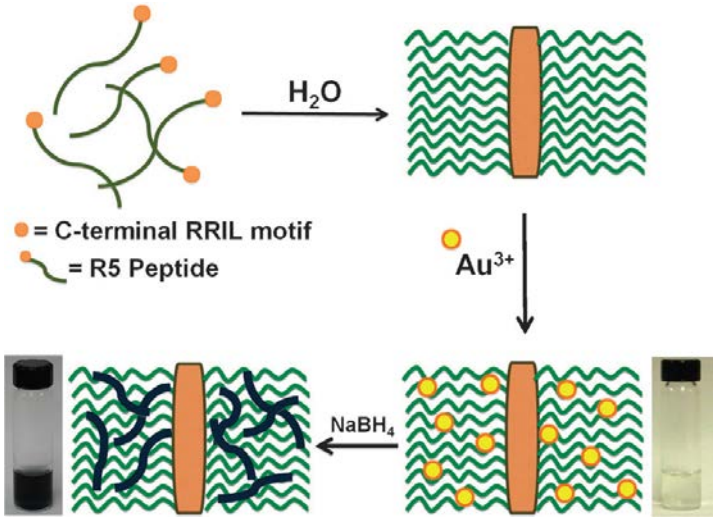

Figure 1.24. Synthesis scheme of Au Nanoparticle networks with the R5 self-assembling peptide [Bhandari, R.; Knecht, M. R. *Catal. Sci. Technol.* **2012**, *2*, 1360.] (Reproduced by permission of the Royal Society of Chemistry).

These Au nanoparticle networks were prepared at Au^{3+}:peptide ratios of 30 and 60, where ratios of 90 were observed to form bulk materials and precipitate. Au nanoparticle networks were prepared by stirring the R5 peptide in the presence of 30 or 60-fold excess $HAuCl_4$ for 15 minutes, followed by the addition of $NaBH_4$. Solutions were stirred for 1.0 h during reduction and dialyzed for 24.0 h to remove excess R5 peptide. This contrasts the synthesis of the Pd materials, as ratios of 120 were observed to be stable as Pd nanoparticle networks.[25] This difference in loading stability demonstrates changes that must occur as a function of the metal ion precursor. The prepared Au30 and Au60 materials were characterized via TEM (**Figure 1.25**) and employed as catalysts for the reduction of 4-nitrophenol.[100]

TEM analysis of the materials shows similarities between the Au30 and Au60 materials, as shown in **Figure 1.25**.

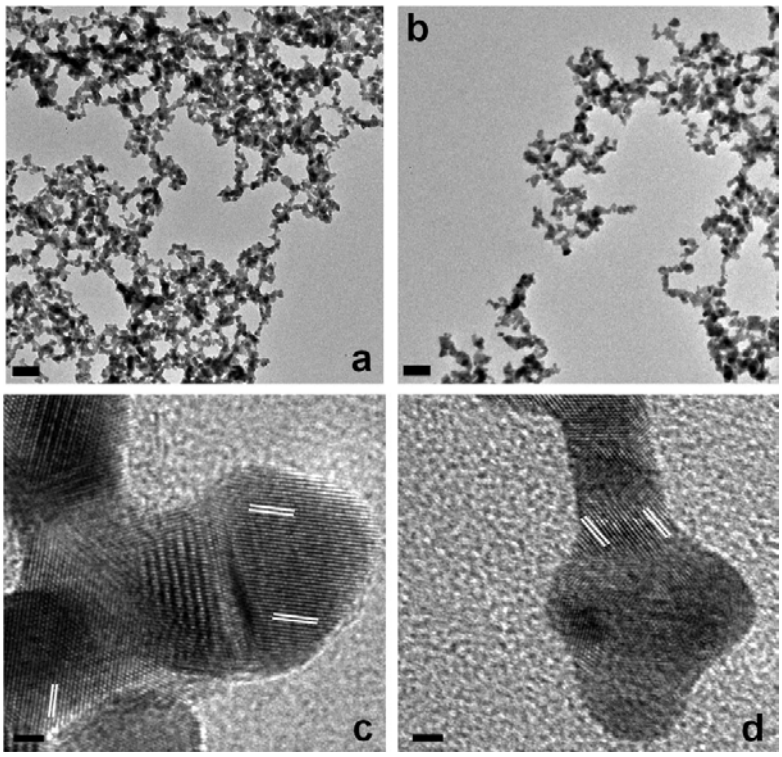

Figure 1.25. TEM analysis of the Au30 (a and c) and the Au60 (b and d) materials. Scale bars are 50 nm (a and b) and 2 nm (c and d) [Bhandari, R.; Knecht, M. R. *Catal. Sci. Technol.* **2012**, *2*, 1360.] (Reproduced by permission of the Royal Society of Chemistry).

These materials consist of fused nanoparticle networks, with nanoribbon thickness diameters of 7.6 ± 1.1 nm and 7.1 ± 1.3 nm, for the Au30 and Au60 systems, respectively. The Au nanoparticle networks were observed to be polycrystalline, similar to the Pd nanostructures and is consistent with the template-based growth mechanism. HR-TEM images showed multiple lattices present in the network structure, the spacing of which correspond to the (111) *fcc* Au crystalline materials. This suggests that the R5 self-assembles similarly to the what is observed with Pd materials, sequesters Au^{3+} ions, and acts as a scaffold during reduction, in which nucleates fuse into nanoparticle networks.

Recently, Au nanostructures have demonstrated remarkable reactivity for a variety of catalytic reactions, including reduction reactions,[105] electrocatalytic

properties,[106] hydroarylation,[107] and cycloaddition reactions.[108] For the biotemplated Au nanoparticle networks, their reactivity for the reduction of 4-nitrophenol was studied via UV-vis analysis.[100] For this, the consumption of 4-nitrophenol and production of p-hydroxyaniline, the final product, are visible at 400 nm and 300 nm, respectively, as shown in **Figure 1.26a**.

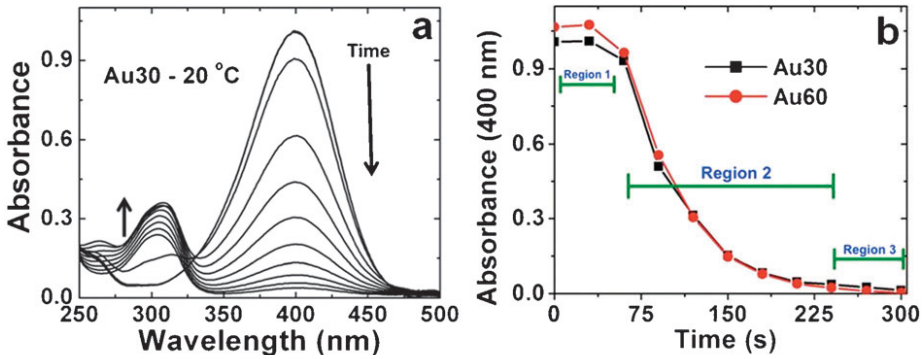

Figure 1.26. Use of the Au NPN in the reduction of 4-nitrophenol. The reaction was monitored a) via UV-vis with b) the observed change in absorbance as a function of time [Bhandari, R.; Knecht, M. R. *Catal. Sci. Technol.* **2012**, *2*, 1360.] (Reproduced by permission of the Royal Society of Chemistry).

Over the reaction time, a decrease in the 400 nm peak was observed, correlating to the consumption of the 4-nitrophenol substrate (**Figure 1.26b**). Simultaneously, an increase is observed for the product at 300 nm. Of the Au30 and Au60 materials, a similar decrease was observed, which demonstrated comparable rates for the reduction of 4-nitrophenol. For the reaction mechanism, the initial decrease in peak intensity at 400 nm is indicative of the materials first undergoing an induction period. This is when both substrates absorb to the metal surface. Next, reduction of 4-nitrophenol occurs on the surface, which was saturated with surface hydrogens. Finally, the 4-aminophenol product desorbs from the material surface, leaving an active site open for the next 4-nitrophenol reagent. While both the Au- and Pd-loaded R5 materials were observed to be stable at the

60 ratio, the same is not true for the 90 and 120 ratios. Where Pd formed stable networks, Au materials were observed to aggregate and form bulk materials. Additionally, the Au:peptide materials formed at a ratio of 60 produced densely fused networks, where the Pd-materials at the same concentration formed spherical nanoparticles. These properties suggest that the Au nanoparticle networks may alter the bioscaffold as the Au^{3+} ions are reduced, nucleate, grow, and fuse. This could allow for heightened diffusion through the scaffold and thus increased reactivity. To that end, it should be noted that the differences between these self-assembled structures allow for activity- and morphology-tunable systems. These peptide self-assembly and materials scaffolding among different systems provide insight into inorganic-directing materials, for which both the functionality and morphology can be modulated.

1.8 Virus-Templated Materials for Catalysis

In addition to their use in display methods, M13 bacteriophage have been exploited for a number of other applications, ranging from complex materials framework to nanowire (NW) scaffolding.[109,110] To that end, binding motifs can be programmed into the coat protein ends to assemble their natural nanowires structure, forming complex assemblies that could be exploited for catalytic applications.[38] Gene modifications (PVIII) allows for peptide additions along the entire phage length. Since the pVIII major coat protein is 50 amino acids in length, only small pVIII gene modifications have been possible. Larger modifications have resulted in failed virus assembly.[111]

Of the possible modifications made to the pVIII protein, a simple addition that complexes metal ions has been demonstrated to be advantageous for the synthesis of phage-based nanomaterials. To this end, Belcher and coworkers made an E4 substitution

(four glutamic acid residues) to the pVIII coat protein through gene modification, resulting in the EEEE tetrapeptide expression along the viral capsid.[40] This substitution allowed for enhanced metal ion binding along the phage backbone, which can be exploited for the template-based production of multiple inorganic nanowires.[39,41]

Both the stability and catalytic activity of Au make it ideal for nanomaterial fabrication. To that end, phage-based Au nanomaterials have been demonstrated as an excellent precursor for bimetallic materials.[112,113] Additionally, Pt has been demonstrated to possess enhanced activity when combined with Au materials.[114] Here, Au-Pt core-shell nanomaterials have been prepared that demonstrated enhanced activity for a number of catalytic applications.[41] These enhanced properties have been attributed to electronic and geometric effects. To achieve such structures, the M13 bacteriophage have been genetically engineered to generate Au nanowires at room temperature, as presented in **Figure 1.27**. Previously selected with affinity for Au,[111] the VSGSSPDS peptide was expressed on the pVIII coat proteins of a phage clone, named p8#9. The capsid shell of this engineered virus allows for the adsorption of both Au^0 and Au^{3+} ions through complexation with the moieties of the amino acid side chains. The Au^{3+} ions are complexed by the capsid-modified virus, resulting in an M13 virus coated with Au ions. The addition of a reductant results in the formation of Au^0 materials at these sites leading to the formation of Au nanoparticles that evolve to generate Au nanowires; however, some aggregation problems were observed. The formation of bulk nanowires aggregates was observed for the Au materials, likely due to insufficient surface passivation. The formation of stable nanowires, however, was observed from the stepwise reduction of Au^{3+} with Ag^+ in the presence of cetyltrimethyl ammoniumbromide (CTAB) surfactant,

in **Figure 1.27**. The Ag^{+} ions were found as homogenous deposits within the Au material, as a 10% alloy due to their low concentration in the reaction mixture. Previously, wildtype Au nanowire materials were synthesized in more random structures with polydispersed morphologies.[115] The presence of the Au-binding sequence and CTAB surfactant likely creates a more stable passivant shell, resulting in consistent nanowires structures. Also, it is likely that the peptide-gold affinity is strong enough such that gold ions move through the surfactant layer to the M13 phage. Noticeably, the nanowires are approximately five times the length of the M13 phage precursor.[41]

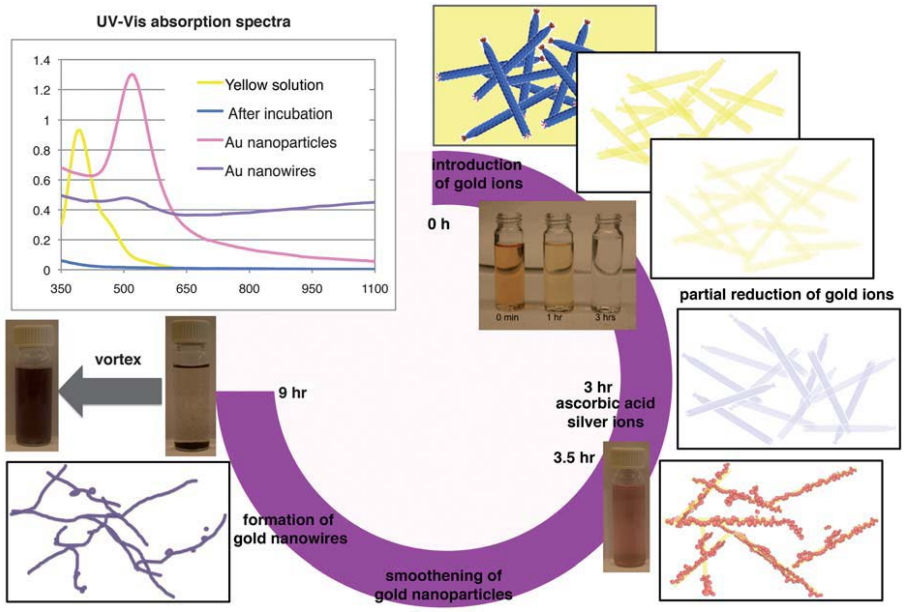

Figure 1.27. Synthesis steps for homogeneous Au-Ag nanowires with the p8#9 M13 phage. This process results in nanowires coated in surfactant, which can be redispersed upon mixing of the violet precipitate [Lee, Y.; Kim, J.; Yun, D. S.; Nam, Y. S.; Shao-Horn, Y.; Belcher, A. M. *Energy Environ. Sci.* **2012**, *5*, 8328.] (Reproduced by permission of the Royal Society of Chemistry).

This length difference is likely due to an end-growth mechanism caused by CTAB on the growing phage-nanowire surface, directing growth where the passivant layer is less uniform.[116] From these nanowires, core-shell materials were synthesized, in which Au-

coated phage were coated with Pt nanoparticles that eventually fused to form the shell. This was performed by controlling the Pt feeding ratios, with varying amounts of Pt^{4+} added to the CTAB-stabilized Au nanowires solution. After incubation, ascorbic acid (a weaker reductant) was added to the solution and heated to 50 °C overnight, resulting in Au-Pt core-shell nanowires, shown in **Figure 1.28**.

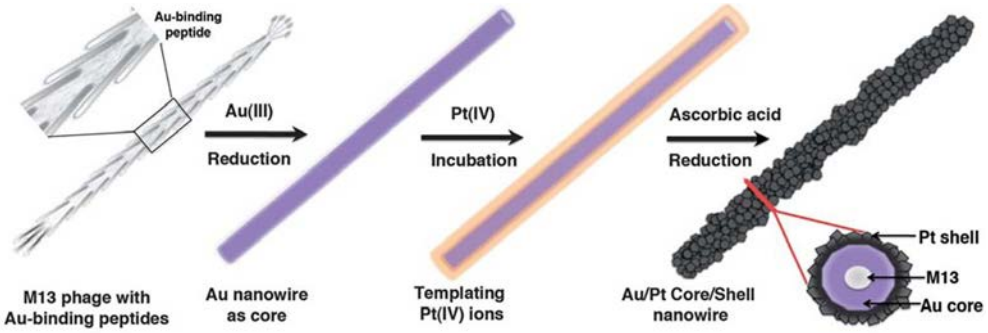

Figure 1.28. Synthesis diagram of Au-Pt core-shell NWs [Lee, Y.; Kim, J.; Yun, D. S.; Nam, Y. S.; Shao-Horn, Y.; Belcher, A. M. *Energy Environ. Sci.* **2012**, *5*, 8328.] (Reproduced by permission of the Royal Society of Chemistry).

TEM imaging revealed that very fine Pt nanoparticles were present on the surface of the Au nanowire core. Overall, the AuPt nanowires were observed to contain polycrystalline, fused Pt nanoparticles on the surface of the structures giving rise to the unique morphology (**Figure 1.29**).

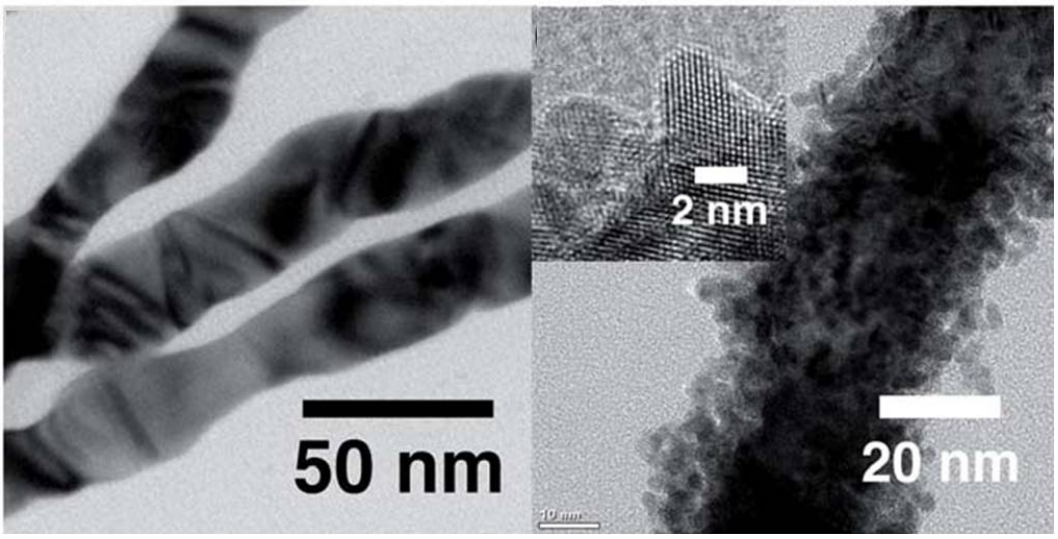

Figure 1.29. TEM images of the Au NWs on the left and then the Au-Pt core-shell nanowires on the right [Lee, Y.; Kim, J.; Yun, D. S.; Nam, Y. S.; Shao-Horn, Y.; Belcher, A. M. *Energy Environ. Sci.* **2012**, *5*, 8328.] (Reproduced by permission of the Royal Society of Chemistry).

Three sets of materials were prepared and tested, where the Au:Pt ratio employed to generate the materials was 2.6:1.0, 1.8:1.0, and 1.0:1.0. The nanowire precursor diameters were observed to be controllable from 10-50 nm with varying ratios or phage, CTAB, and Au^{3+}. Resulting core-shell materials were observed to be ~30 nm, on which fine Pt nanoparticles were deposited. A minimal increase in nanowires diameter was observed for these systems, with the most surface coverage present in the 1.0:1.0 system (**Figure 1.29**, right). STEM analysis of the 1.0:1.0 materials was performed, with compositional mapping observed in **Figure 1.30**.

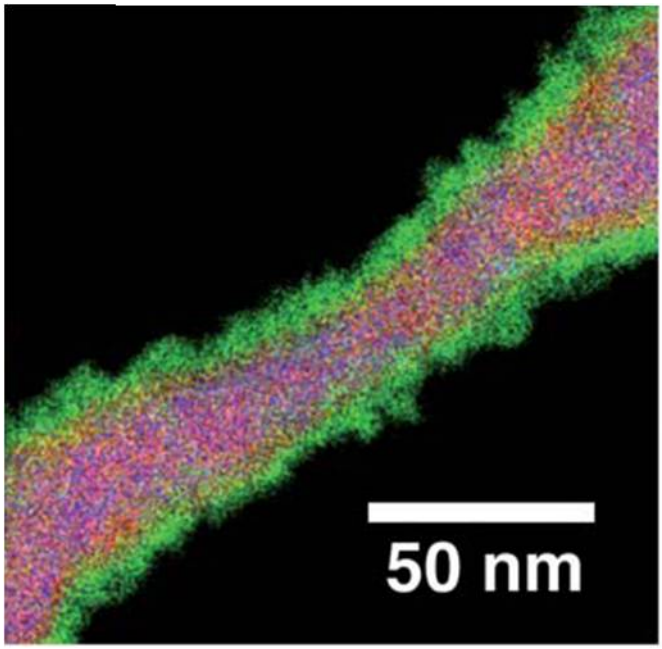

Figure 1.30. STEM analysis of AuPt core-shell NWs. Red corresponds to Au, blue to Ag, and green to Pt [Lee, Y.; Kim, J.; Yun, D. S.; Nam, Y. S.; Shao-Horn, Y.; Belcher, A. M. *Energy Environ. Sci.* **2012**, *5*, 8328.] (Reproduced by permission of the Royal Society of Chemistry).

Nanowire composition by STEM analysis with selective atomic mapping showed the Au core to be comprised of a mixture of Au(~90%) and Ag(~10%). The surface was observed to be primarily smaller nanoparticles of Pt, which was observed to be polycrystalline. These various ratios of Au:Pt materials were tested for their activity for the oxidation of ethanol in **Figure 1.31**.

As expected, increasing the quantity of Pt loading resulted in an increased Pt surface coverage, as a greater quantity of metal was available for integration at the nanowire surface. This was confirmed via CV (**Figure 1.31a**), as decreasing currents of Au oxide ~1.0 V (RHE) and increasing currents of Pt oxide ~0.7 V (RHE) were observed for the 1.0:1.0 materials.[41]

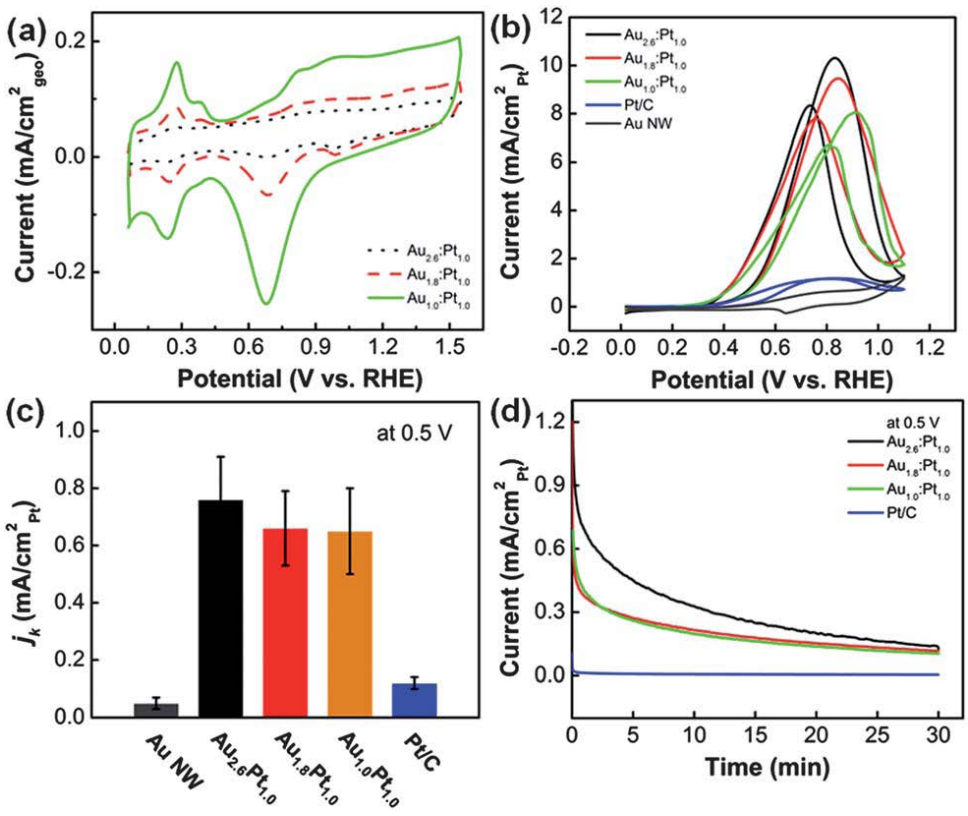

Figure 1.31. Comparison of ethanol oxidation of the materials by a) CV measurements, b) ethanol oxidation polarization curves of Au–Pt core–shell NWs, Au NWs, and a commercial Pt–C catalyst, c) comparison of materials reactivity, and d) chronoamperometry measurements of the materials [Lee, Y.; Kim, J.; Yun, D. S.; Nam, Y. S.; Shao-Horn, Y.; Belcher, A. M. *Energy Environ. Sci.* **2012**, *5*, 8328.] (Reproduced by permission of the Royal Society of Chemistry).

These current changes with respect to other ratio materials demonstrates less available gold (formation of gold oxide) at the surface of the nanowires in addition to more available Pt (formation of platinum oxide) via CV.

For the catalytic analysis, all of the Au-Pt core-shell nanowires demonstrated significantly higher ethanol oxidation currents than that of the monometallic Au nanowires, as shown in in **Figure 1.31c**. The ethanol oxidation reaction (EOR) activities of core–shell nanowires with atomic ratios of Au:Pt as 2.6:1.0, 1.8:1.0, and 1.0:1.0 are observed to be 0.72, 0.60, 0.65 (mA cm^{-2}_{Pt}) of the Pt catalyst, respectively (**Figure**

1.31c). Noticably, the lowest ratio of Pt demonstrated the highest average activity for EOR, but error overlap shows these values to be statistically equivalent. Furthermore, these materials were observed to be > 6.0, 5.0, and 5.4 times more reactive than commercially available (TKK) Pt–C catalyst (0.12 mA cm^{-2}_{Pt}), respectively. It should be noted that the various materials were roughly similar in their activity for EOR. This suggests that the presence of Pt on the Au nanowires is necessary for enhanced activity, but not largely reflective of the material composition. Additionally, the highest Pt ratio materials demonstrated the lowest average for EOR activity, though the values were still statistically equivalent. This may be a function of surface Pt atoms becoming less affected by the core Au as the distance between the two increases, causing a further decrease in EOR activity.

In addition to bimetallic nanowires employed as catalysts for the oxidation of ethanol, phage functionalized with porphyrin-containing pigments have been used as nanoantennae, demonstrating optical properties as a function of the modified pVIII coat proteins.[117] M13 nanoantennae were prepared by conjugation of the ZnDPEG to the pVIII coat protein via a carbodiimide coupling reaction. These materials were characterized by fluorescence spectroscopy, which demonstrated porphyrin synergy on the phage surface. Due to the proximity of pVIII coat proteins, it is likely that energy transfer can occur between neighboring functionalized pigments. Additionally, the flexibility of the coat protein may allow for the attached moieties to undergo interactions among neighboring porphyrin groups. Initially, these materials were prepared in different ratios of ZnDPEG:M13 virus at 1564 (ZP-M13-1) and 2900 (ZP-M13-2).[117] Fluorescent intensity of tryptophan (excited at 295 nm) was observed to be severely

diminished for the ZnDPEG-functionalized M13 as compared to native M13 in **Figure 1.32a**. Additionally, a small red shift found in the Q-bands is indicative of the formation of electronic coupling among pigments when the materials are excited at 400 nm (**Figure 1.32b**).

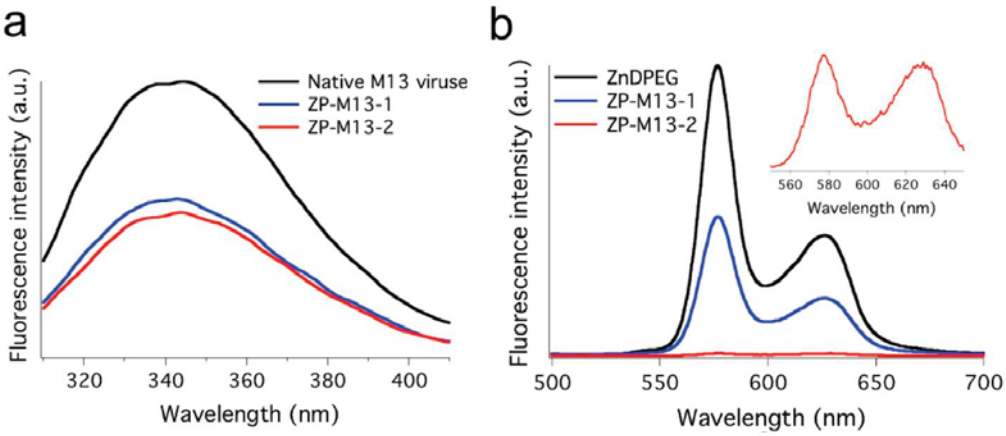

Figure 1.32. Spectra obtained of a) tryptophan fluorescence emission of native M13 viruses and ZP-M13 with excitation at 295 nm and d) fluorescence emission with excitation at 400 nm of ZnDPEG, ZP-M13-1, and ZP-M13-2 (Reproduced from ref. 116 with permission).

The quenching of fluorescence emission may not be very strong in the ZP-M13, as ZnDPEG lacks meso substitutents. This is supported by the presence of fluorescent quenching increasing with increasing conjugation, which implies that close-proximity pigment-pigment electronic interactions are necessary for efficient quenching. The decrease in Trp fluorescence intensity is an effect of interaction with porphyrin moieties, which results in exposed Trp residues to the outer aqueous environment. Additionally, the red shift observed upon excitation at 400 nm supports the presence of porphyrin-porphyrin electronic interactions, such that these nanoantennae may facilitate and optimize light-harvesting, catalytic mechanisms. These materials provide valuable

information in regard to understanding energy transfer occurring in supramolecular porphyrin structures and molecular pigments.

Similarly, phage-based IrO_2 nanowires have also been developed as catalysts for energy production via photochemical water-splitting.[118] Belcher and coworkers developed multiple functional inorganic structures for this reaction by integrating a photosensitizer and metal oxide catalyst together on M13 phage. For these materials, iridium oxide (IrO_2) was chosen as it is known to be quite stable and catalytically reactive for water splitting. For the development of a material with affinity to IrO_2, phage display was performed with IrO_2 substrate. Phage were isolated that contained the octameric sequence AGETQQAM, which was observed to show a strong affinity to IrO_2 surfaces. These engineered phage were then used as supports for nanoscale organization including both IrO2 and the photosensitizer Zn(II) deuteroporphyrin IX-2,4-bis-ethylene glycol (ZnDPEG). The IrO_2-binding phage were introduced to a ZnDPEG solution, yielding porphyrin nanoantennae structures, as previously described. To prepare IrO_2 material precursors, Na_2IrCl_6 was first hydrolyzed to form Ir nanoclusters with citrate as a ligand. To the phage-porphyrin solution, Ir hydrosol clusters were added in the presence of H_2O_2, which yielded the final product, IrO_2-porphyrin nanowires.

TEM studies were used to confirm the structure and composition of the hybrid materials. From this study, it showed compositional and structural differences throughout the material synthesis. Here, materials were prepared with various IrO_2:nanoantennae loading ratios, which demonstrated morphologies ranging from networks to more obvious nanowires (**Figure 1.33**).

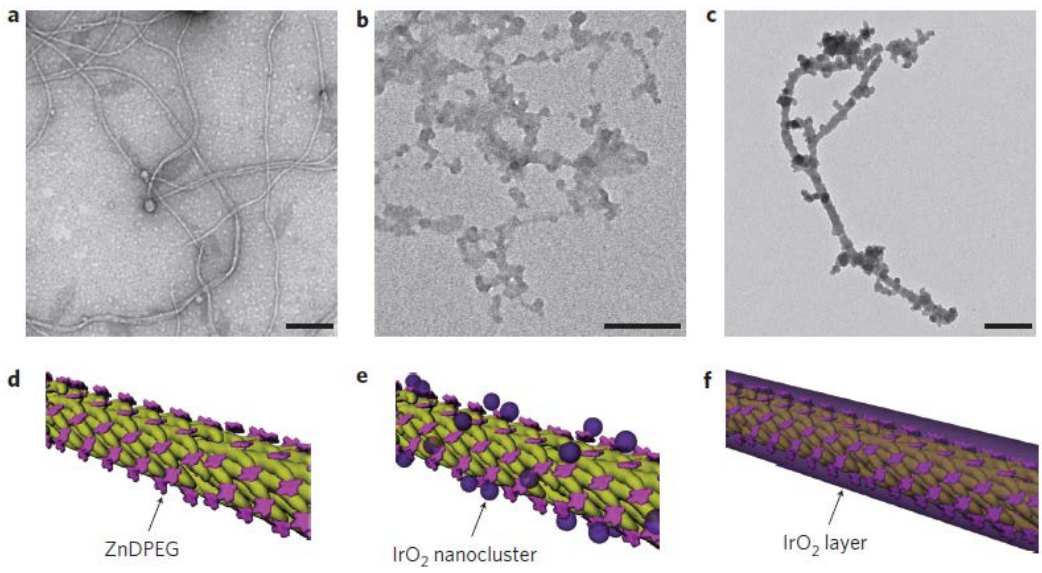

Figure 1.33. TEM images of the engineered M13 virus a) functionalized with ZnDPEG, b) with the IrO_2 nanoclusters at 15:1 IrO_2:ZnDPEG ratios, and c) IrO_2 nanowires at 224:1 IrO2:ZnDPEG ratio. The graphic representations in d, e, and f correspond to the materials in a, b, and c, respectively. Scale bars are 200 nm (Reproduced from ref. 117 with permission).

As displayed in **Figure 1.33**, materials prepared with the IrO_2:ZnDPEG 15:1 ratio of IrO2 were observed to show more cluster-like morphologies, which resemble fused networks of particles. As the ratio increased to 224:1, a greater amount of IrO_2 is present in the system and available for binding to the phage surface. This excess IrO_2 results in morphologies that produce a more fully-developed layer abound the nanoantennae, resulting in recognizable, wire-like structures. Visible in **Figure 33c** and **f**, nanowires are visible when materials are prepared at the 224:1 ratio.

After the materials were characterized, other ratios were prepared, ranging from 15, 41, 72, and 224 IrO_2:ZnDPEG loading. Materials were prepared at a ratio of 42 with both conjugated and unconjugated ZnDPEG and as photocatalytic materials for water-splitting. These include IrO_2 with unconjugated ZnDPEG, IrO_2 with ZnDPEG-virus, IrO_2 wires with unconjugated ZnDPEG, and IrO2-ZnDPEG hybrid wires. For this

analysis, the production of O_2 was used to measure material reactivity. Of the systems prepared, the IrO_2-ZnDPEG hybrid wires demonstrated the highest amount of oxygen produced with respect to moles of catalyst, turnover number (TON) (**Figure 1.34a**).

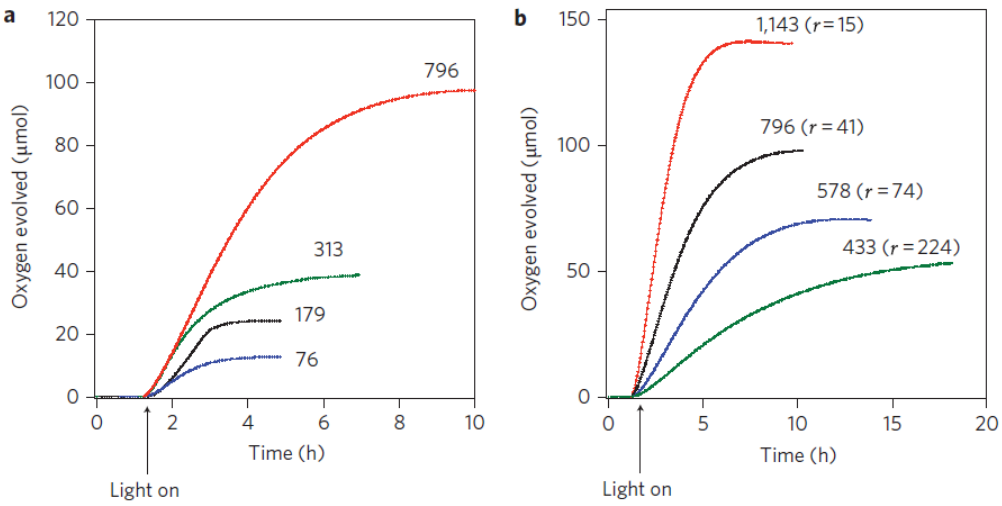

Figure 1.34. Water-splitting efficiency TON values. The left (a) represents ratios of 42 of the (black) IrO_2 with unconjugated ZnDPEG, (green) IrO_2 with ZnDPEG-virus, (blue) IrO_2 wires with unconjugated ZnDPEG, and (red) IrO2-ZnDPEG hybrid wires. The right (b) represents IrO2-ZnDPEG NWs at the corresponding ratios (Reproduced from ref. 117 with permission).

For this analysis, the materials prepared at IrO_2:ZnDPEG ratios of 15, 41, 72, and 224, demonstrated TON values of 1143, 796, 578, and 433 for the production of oxygen, respectively. As such, the lowest IrO_2:ZnDPEG ratios resulted in the highest activity, indicating that larger amounts of ZnDPEG resulted in increased reactivity. Additionally, the TONs associated with the amount of photosensitizer employed were observed to be indicative of the porphyrin stability trend, which is opposite of the TON trend observed above. The use of excess catalyst can prolong the stability of the photosensitizer, as charges generated from oxidation can be transferred to the nearby catalyst, resulting in a catalysis delay. This means that higher overall catalyst loading can result in lower activity for these systems.

In addition to M13-templated photocatalysts, the virus-based assembly of materials for the conversion of H_2 from ethanol have also been shown to be reactive for this catalytic process.[119] Previously, Rh@CeO_2 materials have been used for the conversion of water/ethanol mixtures into H_2 for use as a fuel.[120] While this is somewhat effective, the addition of Ni enhances the ability to oxidatively reform ethanol to generate the final H_2 product.[121] To that end, cleavage of the C-C bond occurs, leading to the degradation products CH_4, CO, and H_2O to H_2 and CO_2. In addition to Rh@CeO2 materials, Ni has also been employed as a dopant, further enhancing catalytic activity. To that end, the M13 phage was created with an AEEE addition to the major coat protein, which could complex metal ions and act as a nucleation site for the formation of CeO_2 NWs with Ni/Rh dopants.[119] To a 1 mM metal precursor solution, materials were prepared first without M13 as a control and then with 10^7 M13/mL, 10^{10} M13/mL, and 10^{13} M13/ mL additions. This solution underwent nucleation and growth by an addition of NaOH and H_2O_2, which formed Ni/Rh@CeO_2 networks. From this, the phage-templated materials were produced and imaged via TEM in **Figure 1.35**. Prior to catalytic testing, these materials were heated to 400 °C to burn off any residual phage.

For catalytic purposes, greater surface area is desired for reactivity, which was shown to be controlled as a function of the pore size. To that end, 90% of pore were observed to be 4.5 nm, leading to a surface area of 180 m^2/g for the M13-based materials. This is quite important when compared to the control materials generated in the absence of the biomimetic template, which possessed 5.9 nm pore sizes with a surface area of 143 m^2/g.

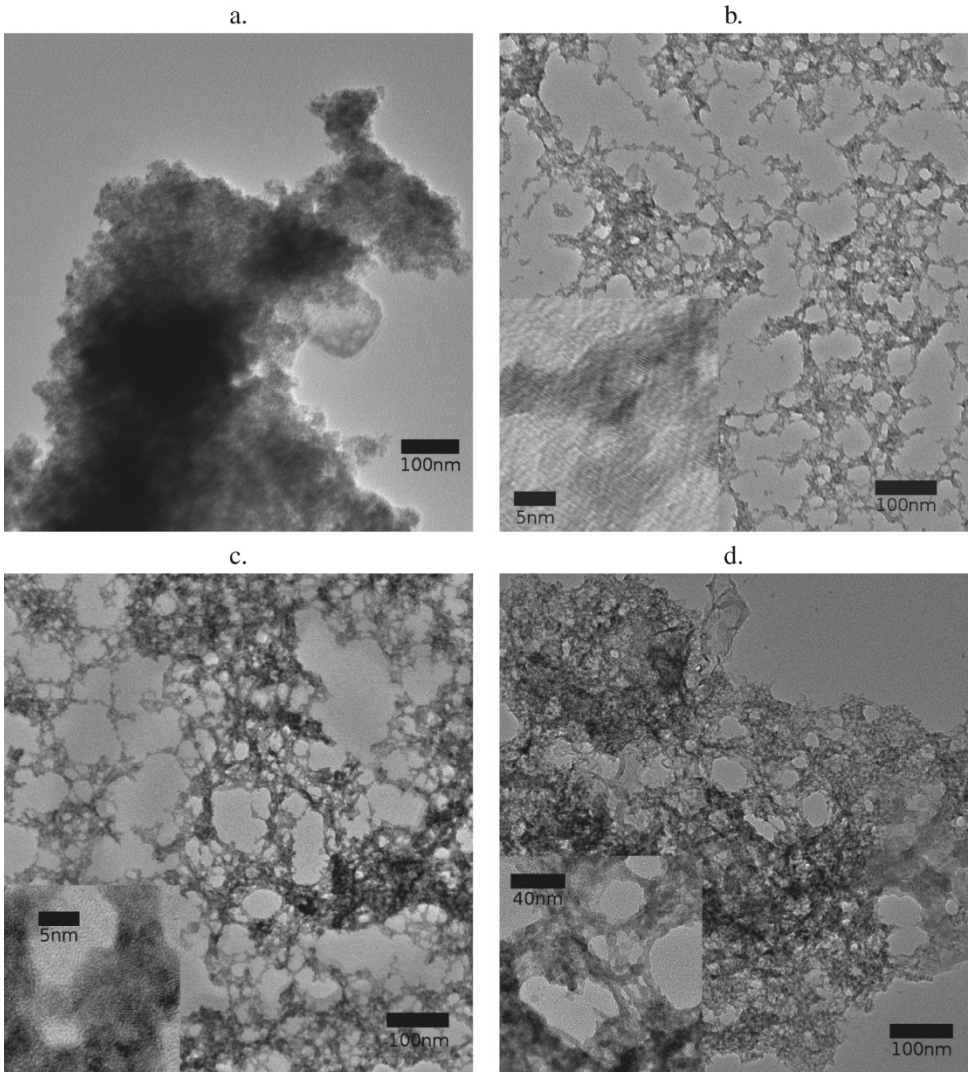

Figure 1.35. TEM analysis of AEEE-modified M13 phage-templated materials. Catalyst made at 1 mM metal precursor, (a) without M13, (b) with 10^7 M13/mL, (c) with 10^{10} M13/mL, (d) with 10^{13} M13/ mL. Insets show higher magnification images (Reproduced from ref. 117 with permission).

Once confirmed, these materials were employed as catalysts for the steam reform reaction with ethanol. For this, a 1.7:1:10:11 air/ethanol/H_2O/Ar mixture was flowed over 100 mg of the nanostructures, where product generation was monitored via GC. Conversion rates were calculated as a ratio of ethanol consumed versus ethanol injected, with N_2 as an internal standard. Conversion rates were calculated for both the M13-templated materials and untemplated materials, in **Figure 1.36**.

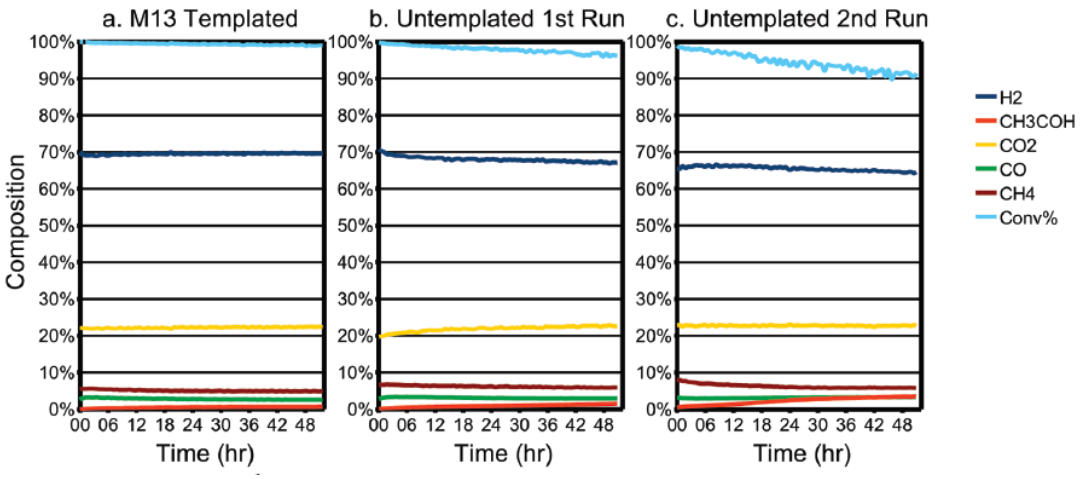

Figure 1.36. Product conversion from the reagent mixture for a) M13-templated, b) untemplated first run, and c) untemplated second run materials (Reproduced from ref. 117 with permission).

For the template materials, an initial 100% conversion of ethanol was observed, with only a 1% loss in conversion observed after 52.0 h. Additionally, steady degradation was observed for other materials with product yields of 70% H_2, 5% CH_4, 3% CO, and 1% acetaldehyde. The untemplated materials showed very similar initial values, but they also demonstrated diminished substrate conversion over time. These materials were observed to regain some amount of activity when exposed to air; however, their rate reactivity diminishment increased over subsequent runs. It is likely that the virus template allows for more uniform and ordered formation of these networks. This uniformity allows for a more ordered structure, which yields pores in the material structure and thus a greater surface area. These structures demonstrated increased stability, decreased vulnerability to deactivation, smaller pore size, and higher catalytic activity.

These engineered-phage materials provide valuable progress toward the synthesis of biomimetic catalytic materials, in which the biological structures can direct the organization of the inorganic components for increased reactivity. These materials allow

for more efficient catalysts, with less precious metal waste and the ability to function in ambient conditions. While other bio-nanomaterial systems have been demonstrated to be advantageous, bacteriophage virus assembly methods are invaluable as nanowire precursors and nanowire-framework protocols. The M13 pIII, pVIII, and pIX coat proteins allow for highly versatile modifications, assemblies, and various metal-coordinating precursors. Additionally, the use of phage for both the isolation of materials-specific peptide sequences and with the use of these sequence makes phage incredibly valuable for the continued development of superior nanomaterials.

1.9 Conclusions

Despite the current development of biomimetic nanomaterial systems, the binding interactions that drive the synthesis and surface reactivity of these materials still remain unclear. While individual amino acids can be observed to possess binding effects, the binding interaction of longer sequences is significantly more complex and difficult to characterize. A delicate balance of peptide structure, binding, and surface assembly govern the final size, shape, and functionality of nanomaterials. To that end, these properties can all potentially be modulated through rational peptide design and bio-ligand concentration. The selective tuning of these characteristics can lead to the development of optimized catalytic materials, with specific functionality obtained through size and surface effects. Additionally, the design of peptide-modulated activity on inorganic surfaces allows for selective shapes through directed facet growth and thus the exposure of high-energy edge and vertex atoms. The optimization of inorganic surfaces and sequence-controllable activity through biomimetic nanomaterial synthesis could lead to

superior nanomaterials with functionality over a wide range of applications. To that end, the continued pursuit of superior materials inspired from biological organisms and their efficiency is economically and ecologically beneficial.

Chapter 2. Alanine Substitutions to the Histidine Sites of a Pd Surface-Specific Peptide Sequence.

2.1 Overview of Study

The study of naturally-occurring bio-inorganic processes has lead to the development of materials-directing biomolecules, for exacting control over complex structures. These biomolecules have been used to effectively act as surface ligands, either directing the growth of specific facets or assembling on the material and governing access to the passivated surface. This study employs a peptide which was isolated via phage display with affinity for Pd surfaces and its alanine analogues for the synthesis of Pd nanoparticles. The substitution of the binding histidines with alanine amino acids resulted in a range of effects, which likely modulated the biotic/abiotic interfacial properties of the resulting materials. Upon alanine substitution of the Pd4 sequence, particle diameter was observed to increase with respect to substitution placement. Along these lines, these substitutions could modulate peptide binding strength, which could in turn cap particle growth at slightly different time points. These Pd nanoparticles were employed as catalysts in the C-C Stille coupling reaction. By varying the histidine placement and/or presence in the peptide sequence, a range of TOF values were observed, which can provide valuable information about the peptide-metal binding interaction.

2.2 Introductory Remarks

Natural processes have been developed to produce nanostructures that involve recognition between biomolecules and inorganic surfaces.[22] Such methods have been exploited in the production of nanomaterials for use as catalysts,[26,28,86] biosensors,[122]

batteries,[40,123] and components for directed assembly;[86,124] however, the interactions at the biotic/abiotic interface remain unclear. These interactions are likely to control the activity of the nanostructures, which could be optimized based upon the peptide sequence and arrangement on the nanomaterial surface. Whilst these studies have demonstrated the unique activity of such bio-enabled materials,[26,28,86,122] to the best of our knowledge, no research is available that probes the critical effects of the surface peptide on nanomaterial activity. Previous reports have suggested that peptides bind to surfaces in a different manner to individual amino acids;[60,80,125] therefore, by understanding these interactions, the design of bionanomaterials that have superior functionality may be possible. The Pd4 peptide (Table 1), was isolated using a phage display technique with an affinity for palladium.[26,80] Using this sequence, palladium particles, which have a diameter of approximately 1.9 nm, were prepared that were active for Stille coupling reactions in water, at room temperature, with palladium loadings of ~0.005 mol%. Modeling of the peptide–nanoparticle interactions suggested that the histidine residues at positions 6 and 11 were most likely responsible for the binding as they form a kinked structure that exposes the palladium surface,[80] in **Figure 1.8**.

Herein, we show that by selectively replacing the histidine residues with alanine, the catalytic activity can be modulated to affect the reactivity while maintaining the particle size. These results are critical in understanding the activity of biomimetic materials for two key reasons: First, they suggest that the activity of bionanomaterials can be modulated by the peptide sequence. Second, these studies highlight the underlying cause of the catalytic activity of bionanomaterials, which could be used for the rational design of peptides for the production of functional nanomaterials. Whilst the changes and

enhancements in the catalytic capabilities are intriguing, the main focus of this study is to understand the activity of peptide-based materials. The peptides used in this study were all synthesized, purified, and confirmed as previously described.[26] Four peptides were prepared (**Table 2.1**), based on the parental Pd4 sequence.

Peptide	Sequence	pI[a]	Size (nm)	TOF[b]
Pd4	TSNAVHPTLRHL	9.47	1.9 ± 0.3	2234 ± 99
A6	TSNAVAPTLRHL	9.44	2.2 ± 0.4	5224 ± 381
A11	TSNAVHPTLRAL	9.44	2.4 ± 0.5	1298 ± 107
A6,11	TSNAVAPTLRAL	9.41	3.7 ± 0.9	361 ± 21

[a] pI calculated at http://ca.expasy.org, [b] $\frac{\text{mol BPCA}}{\text{mol Pd} * \text{h}}$

Table 2.1. Pd4 and alanine analogues with corresponding pI, size and TOF analysis.

These included peptides in which the histidine residues were substituted with alanine at positions 6, 11, or 6 and 11, termed A6, A11, and A6,11, respectively. These substitutions were performed with the intent to both isolate and characterize binding properties of the peptide sequence, which are likely histidine-dependent. For nanoparticle fabrication, each peptide was co-dissolved with 3.3 equivalents of K_2PdCl_4 and allowed to sit at room temperature. After 30 minutes, $NaBH_4$ was added to form Pd^0. No precipitation of the bulk metal was observed in any of the cases, which suggests that all of the sequences were capable of controlling the synthesis of the palladium nanoparticles.

2.3 Methods

2.3.1 Chemicals

All FMOC-protected amino acids and Wang resins used for peptide synthesis were purchased from Advanced ChemTech (Louisville, KY). $NaBH_4$ was purchased from EMD (Gibbstown, NJ), K_2PdCl_4 was purchased from Sigma-Aldrich (Milwaukee, WI), and 4-iodobenzoic acid was purchased from TCI America (Wellesley Hills, MA). Phenyltin trichloride (PhSnCl3), $CDCl_3$, anhydrous Na_2SO_4, NaCl, and KOH were purchased from Fisher (Pittsburgh, PA). All reagents were used as received. Milli-Q water (18 mΩ·cm; Millipore, Bedford, MA) was used for all experiments.

2.3.2 Peptide Synthesis

The Pd4, A6, A11 and A6,11 peptides were prepared using a Tetras peptide synthesizer (CreoSalus; Louisville, KY) employing standard FMOC peptide synthesis protocols. Wang resins were employed that were substituted with the last amino acid in sequence (leucine). After synthesis, the peptides were cleaved from the resins using a cleavage cocktail of 95% trifluoroacetic acid, 2.5% triisopropyl silane, and 2.5% water, purified via HPLC employing a water/acetonitrile gradient, and confirmed by MALDI-TOF mass spectrometry.

2.3.3 Biomimetic Nanoparticle Synthesis

Particles were synthesized in 1.00 mL quantities. Individual peptide stock solutions were prepared by dissolving 1 mg of peptide into 100 μL of water. The Pd stock solution (100 mM) was produced by dissolving 16 mg of K_2PdCl_4 into 500 μL of water. To a 10.0 mL vial, 20.0 μL of the peptide stock, 5.00 μL of the Pd solution, and 955 μL of water were allowed to incubate for 30.0 min. Upon completion, 20.0 μL of a freshly prepared 100

mM $NaBH_4$ solution was added and allowed to incubate for 60.0 min to ensure full Pd reduction.

2.3.4 Catalytic Reaction

The coupling of 4-iodobenzoic acid and phenyltin trichloride was employed as the standard Stille reaction to probe the catalytic activity of the nanoparticles prepared using the different peptides. For this reaction, 62 mg (0.250 mmol) of 4-iodobenzoic acid and 49.3 μL (0.300 mmol) of $PhSnCl_3$ were co-dissolved in 4.00 mL of 2.25 M aqueous KOH. Different volumes of the prepared Pd nanoparticle catalysts were then added to the reactions to reach the desired Pd loading. For this, 0.5 mL (0.100 mol %), 250 μL (0.050 mol %), 50 μL (0.010 mol %), 25.0 μL (0.005 mol %), 5.0 μL (0.001 mol %), 2.50 μL (0.0005 mol %), and 0.50 μL (0.0001 mol %) were added in a single injection. To ensure that the 5.0, 2.50 and 0.50 μL volumes were analytically transferred, they were diluted by a factor of ten and then transferred by pipette. Each reaction was finally diluted with appropriate volumes of water so that all were studied using the same reaction volume. The reactions were then allowed to vigorously stir for 24.0 h at room temperature. Upon completion, the reactions were quenched with 25.0 mL of a 5.00 % aqueous HCl solution. The product was extracted from the reaction mixture using three 30.0 mL washes of diethyl ether. The organic layer was then treated with two 20.0 mL washes of a saturated NaCl solution, dried with anhydrous Na_2SO_4, and filtered. To the extracted organic layer, 75.0 mg (0.500 mmol) of 4-tert-butylphenol was added to serve as the internal standard for reaction quantitation. The organic solvent was then removed using a rotary evaporator. Once dried, ~1 mg of the product was dissolved in $CDCl_3$, which was analyzed and quantitated using ^1H NMR.

2.3.5 Turnover Frequency (TOF) Measurement

In determining the TOF value of the catalyst, the reaction was monitored for 1.00 h at time intervals of 0.00, 5.00, 10.0, 15.0, 20.0, 25.0, 30.0, 40.0, 50.0, and 60.0 min. The coupling reaction between 4-iodobenzoic acid and $PhSnCl_3$ was scaled up by 5.0-fold, and 2.00 mL aliquots were obtained after each time interval. In a 250 mL beaker, 0.310 g of 4-iodobenzoic acid (1.25 mmol) and 246.5 μL of $PhSnCl_3$ (1.50 mmol) were co-dissolved in 20.0 mL of 2.25 M aqueous KOH. Then, 1.25 mL of the Pd nanoparticle catalyst, which represents a Pd loading of 0.050 mol %, was added to the reaction mixture. Immediately after catalyst addition, a 2.00 mL aliquot was extracted and quenched with 12.5 mL of 5.00% aqueous HCl. Aliquots were then taken after the specified time intervals, quenched, and extracted as described above.

2.3.6 Characterization

UV−vis spectrometry of all materials was obtained using an Agilent 8453 UV−vis spectrometer employing a 1.00 cm path length quartz cuvette (Starna). All spectra of the Pd^{2+}/peptide complexes were background subtracted against the appropriate peptide dissolved in water at the reaction concentration, while spectra of the nanoparticles were background corrected against water. Binding constants were obtained for all sequences through QCM-D analysis of each peptide with a Q-Sense E4 QCM-D system with standard flow modules. Pd-coated chips were prepared by sputter-coating Pd onto Au QCM chips (QSX301) for 180 seconds with a Cressington 108-auto sputter coater. The chips were inspected for defect prior to use. Surfaces of the chips were cleaned with a BIOForce UV/ozone cleaner by exposure to UV/ozone for 10.0 min, a deionized water rinse, and a final 10.0 min UV/ozone exposure. A bulk stock solution of each peptide was

created at 10 mg/mL by dissolution of the peptide in Milli-Q deionized water, and diluted to concentrations of 2.5, 5.0, 7.5, 10.0, and 15.0 μg/mL. Frequency changes were observed for each chip in water for ~ 5.0 min, to ensure chip integrity and then peptide stock solutions were added after a baseline had been obtained. Measurements were performed at a flow rate of 0.15 mL/min throughout for each analysis. The third overtone frequency was observed for all measurements. The reciprocal of this change in frequency was used for Langmuir model fitting. This equation was derived to be applicable to a multi-concentration system, such that k_{obs} values can be obtained, allowing for the isolation of the k_a and k_d for each peptide.

Transmission electron microscopy images were obtained using a JEOL 2010F TEM operating at 200 keV with a point-to-point resolution of 0.19 nm. Samples were prepared on 400 mesh Cu grids coated with a thin layer of carbon (EM Sciences). The solution (5.00 μL) was pipetted onto the surface of the grid and allowed to dry in air and stored in a desiccator until analyzed. NMR spectra of the reaction products were obtained using a Varian 200 MHz NMR. The product and the internal standard (1.0−2.0 mg) were dissolved in 1.00 mL of $CDCl_3$ and added to a 5.00 mm NMR tube (Wilmad). The integration of the peak at δ 8.2 ppm (product) was compared with the integration of the peak at δ 6.8 ppm (internal standard; *tert*-butylphenol, TBP) to obtain the reaction yield. Circular dichroism spectra were collected on a Jasco J-815 CD spectrometer using a quartz cuvette. Free peptides were dissolved in water at a concentration of 16 μM, while peptide functionalized Pd NPs were prepared as above and then diluted to a 16 μM peptide concentration.

2.4 Results and Discussion

2.4.1 Peptide sequence and NP synthesis

While the overall improvement of catalytic nanomaterials is significant, the focus of this work is to realize the interfacial binding of peptide-based materials to inorganic surfaces. Each peptide analogue was based on the parent, Pd4, sequence, such that histidine residues were substituted with alanine moieties at positions 6, 11, or 6 and 11, termed A6, A11, and A6,11, respectively in **Table 2.1**.

Using these peptides, nanoparticles were synthesized with K_2PdCl_4 and $NaBH_4$ and allowed to incubate at room temperature for 1.0 h. Previous Pd4-based materials were prepared at 3.3:1 ratio,[26] so this ratio was employed for the other materials. No precipitation of bulk Pd was observed for any of the peptides at a ratio of 3.3:1 of K_2PdCl_4 to peptide, which suggests the capability of controlling the synthesis of Pd NP.

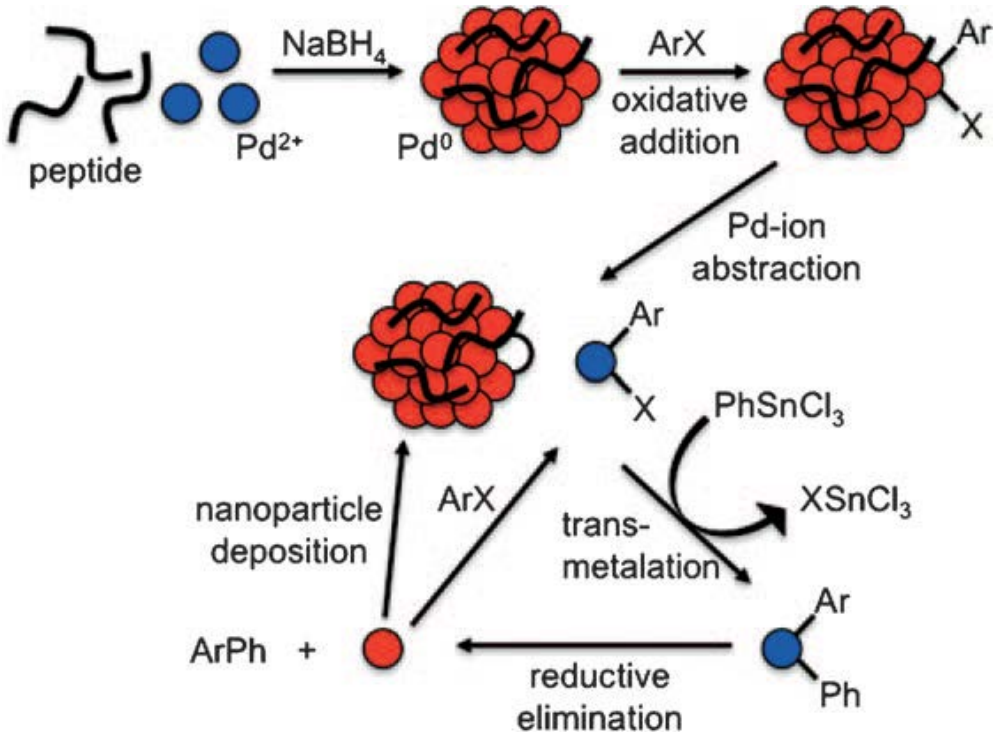

Figure 2.1. Catalytic cycle of the Stille coupling reaction with peptide-passivated Pd nanoparticles.

These materials were used as a catalytic Pd source for the Stille coupling reaction, which is suggested to employ an atom-leaching mechanism that is controlled by the binding interaction and free structure of the peptide passivant on the nanoparticle surface, in **Figure 2.1**. These materials were further characterized by a range of techniques and employed as carbon-carbon coupling catalysts, from which catalytic activity differences provided valuable surface interaction information.

2.4.2 Spectroscopic Materials Characterization

Characterization of the peptide-capped Pd nanoparticles was performed with various techniques imaging, with spectroscopic measurements and electron microscopy. UV-vis analysis of the peptides are recorded in **Figure A2.1**, while spectra of the complexes and nanoparticles can be seen in **Figure 2.2**. Upon addition of the K_2PdCl_4 stock to the peptide solution, the reaction was observed to turn pale yellow. The spectra of the reactions prior to reduction showed an absorbance shoulder at approximately 224 nm. This absorbance is consistent with the palladium–amine ligand-to-metal charge transfer band (LMCT), which indicates that Pd^{2+} binds to the peptide.[26,126] After the addition of $NaBH_4$ and Pd reduction, a color change from yellow to brown was observed, with an increase in absorbance at lower wavelengths.

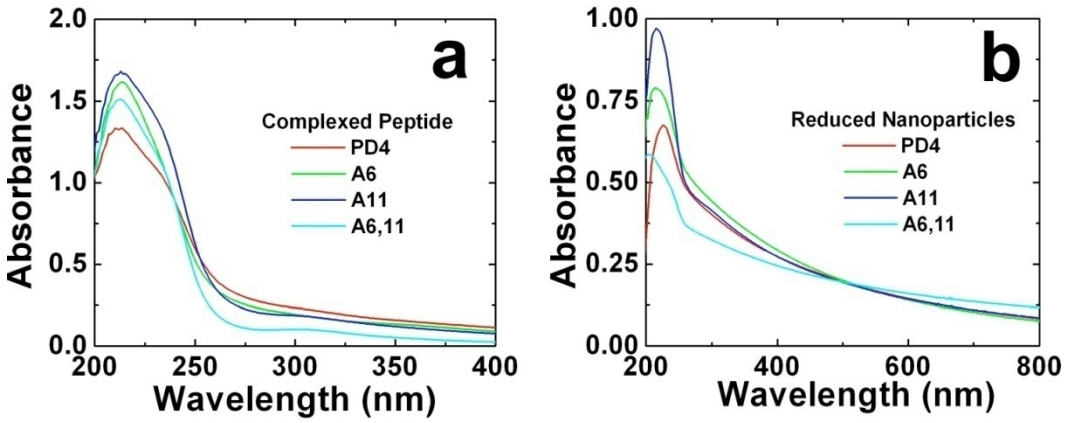

Figure 2.2. UV-vis spectra of the Pd4 and analogue peptides a) when complexed with Pd^{2+} and b) the resulting nanoparticles upon reduction with $NaBH_4$.

Nearly identical spectra were noted for the materials prepared using the Pd4, A6, and A11 peptides; however, the materials prepared using the A6,11 peptide demonstrated a larger degree of scattering at longer wavelengths. This change in absorbance and lack of Pd black formation is indicative of the presence of stable Pd nanoparticles.

2.4.3 QCM Analysis of Pd4 and Ala-Analogues

Binding of small molecules and biological components has been observed via QCM for gold and other inorganic surfaces.[61,127] These binding properties are valuable, as they can begin to provide information about the interfacial orientation of these molecules, which could lead to the understanding of surface control by biological components. Binding affinity values (k_a, k_d, and Keq) were obtained for each peptide sequence via QCM analysis, through the measurement of five incremental concentrations of Pd4, A6, A11, and A6,11 on Pd-coated QSX sensors. For this work, peptide adsorption was monitored for each peptide concentration over 30.0 min, the frequency change recorded, and the inverse of this change fit with a modified Langmuir model equation (**Figure A1.1**).[61] The

Langmuir model was derived to be applicable to a multiple-concentration system, such that the k_a and k_d are both unknown, in **Figure 2.3a** . The surface coverage, θ(t), is directly proportional to the change in frequency of the QCM sensor, via the adsorbed mass-frequency relationship in the Sauerbrey equation. Fitting the Langmuir model system, derived to **Figure 2.3e**, to the positive reciprocal of each spectra at the respective concentrations, yields a respective k_{obs} value to each peptide concentration (**Figure A1.2**). A series of five k_{obs} values were obtained for each peptide and plotted against their respective concentrations in **Figure 2.4** for the Pd4 peptide. From the Langmuir model, the k_{obs} can be plotted against peptide concentration to obtain k_a and k_d values via a linear fit, as seen in **Figure 2.3e**.

a $$\frac{d\theta}{dt} = k_a\,(1-\theta)C - k_d\theta$$

b $$\theta(t) = \frac{C}{C + \frac{k_d}{k_a}}\,(1 - e^{-(k_aC + k_d)t})$$

c $$k_{obs} = k_aC + k_d$$

d $$k' = \frac{C}{C + \frac{k_d}{k_a}}$$

e $$\theta(t) = k'(1 - e^{-k_{obs}t})$$

Figure 2.3. The Langmuir model equation (a) and equation rearrangement for QCM analysis of peptide affinity (b-d), such that k_{obs} values can be obtained, yielding k_a and k_d values for each peptide (e).

From the frequency change obtained in the form of reciprocal frequency vs time, the Langmuir model equation was fit for each spectra, as seen for Pd4 in **Figure 2.4a**. These were then plotted as a function of concentration and a linear fit assigned, such that the slope and intercept provide the k_a and k_d, respectively (**Figure 2.4b**).

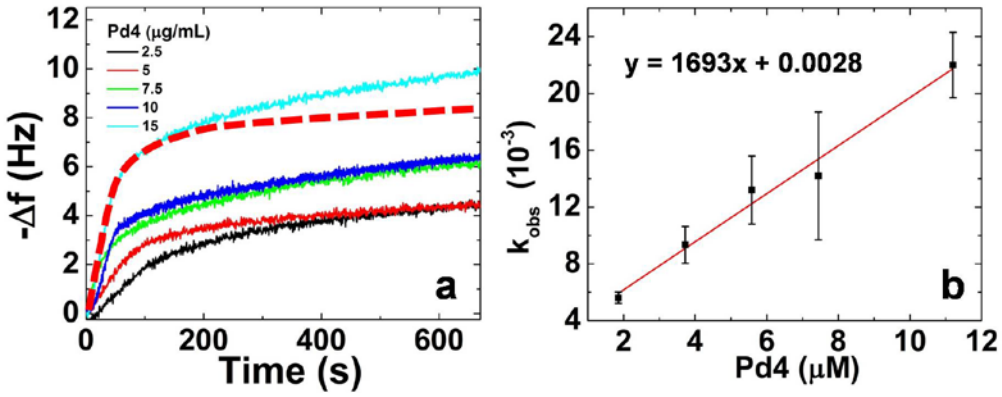

Figure 2.4. Reciprocal QCM measurements of incremental concentrations of a) five concentrations of the Pd4 peptide, with a Langmuir model fit example for the 15 µg/mL concentration and b) the kobs values plotted as a function of concentration and a linear fit assigned.

In **Figure 2.4a**, the inverse frequency change is plotted vs time for concentrations of 2.5, 5.0, 7.5, 10, and 15 µg/mL of the Pd4 peptide on Pd-coated chips. The dotted red line represents an example fit Langmuir model, of which the intensity of the initial slope is indicative of the resulting k_{obs} value. Each of these values for Pd4 are plotted as a function of their concentration in **Figure 2.4b**, and a linear fit assigned, which yields the equation y = 1693x + 0.0028. Similar figures are present for the QCM measurements and Langmuir model fitting for A6, A11, and A6,11 peptides in **Figure A1.2**. From this linear equation, the slope is extracted as the k_a value and the intercept as the k_d. From these values, the K_{eq} can be calculated by k_a / k_d and the ΔG by the equation ΔG = –RT ln

(K_{eq}). For Pd4 and the ala-analogue peptides, the k_a, k_d, K_{eq}, and ΔG values are visible in **Table 2.2**.

Peptide	k_a ($M^{-1}s^{-1}$)	$k_d \times 10^{-3}$ (s^{-1})	$K_{eq} \times 10^5$ (M^{-1})	ΔG (kJ/mol)
Pd4	1693 ± 169	2.8 ± 0.6	6.1 ± 1.3	-33.0 ± 0.5
A6	2215 ± 368	2.9 ± 1.8	7.6 ± 4.8	-33.5 ± 1.5
A11	1960 ± 449	2.3 ± 2.0	8.3 ± 7.8	-33.8 ± 2.2
A6,11	1075 ± 164	4.8 ± 2.0	2.2 ± 1.0	-30.5 ± 1.1

Table 2.2. QCM analysis of peptides Pd4, A6, A11, and A6,11, of which the k_a and k_d were extracted via the Langmuir model equation and the K_{eq} and ΔG could then be calculated.

QCM analysis and Langmuir model fitting of the resulting spectra revealed a k_a value of 1693 ± 76 $M^{-1}s^{-1}$ for the Pd4 peptide on Pd-coated chips. This value is similar to that of other surface-binding peptides previously reported. Upon substitution of the 6-position histidine, the k_a was observed to increase to 2215 ± 368 $M^{-1}s^{-1}$ for A6, which is statistically higher than that of the Pd4 peptide. Substitution of the 11-position histidine resulted in a slight increase in average k_a to 1960 ± 449 $M^{-1}s^{-1}$, though the error overlaps that of Pd4. Finally, the A6,11 peptide, was observed to possess the lowest overall k_a value at 1075 ± 164 $M^{-1}s^{-1}$, which is not surprising considering the removal of the binding histidine groups. The dissociation constants observed were similar among Pd4 and A6 peptides, with values of 0.0028 ± .0002 s^{-1} and 0.0029 ± .0018 s^{-1}, respectively. A decrease in the k_d average was observed for the A11 peptide, with a value of .0023 ± .0020 s^{-1}, which is still statistically similar to Pd4 and A6. For the double alanine-substituted A6,11, a significant increase was observed with a k_d value of 0.0048 ± .0020 s^{-1} for Pd surfaces. Similar to the trend observed with the k_a values, this may be attributed

to the removal of both binding histidine residues, which would leave the A6,11 peptide dependent on its less interactive amino acids, backbone, and N-terminus, resulting in a diminished ability to retain binding and an increased dissociation constant. The K_{eq} values follow the k_a and k_d trends, with values of $6.05 \times 10^5 \pm 5.1 \times 10^4$ M^{-1}, $7.64 \times 10^5 \pm 4.80 \times 10^5$ M^{-1}, $8.25 \times 10^5 \pm 7.76 \times 10^5$ M^{-1}, and $2.24 \times 10^5 \pm 1.02 \times 10^5$ M^{-1} for Pd4, A6, A11, and A6,11 peptides, respectively. As expected, the K_{eq} values of Pd4, A6, and A11 are similar, while A6,11 is observed to possess a diminished K_{eq} value average. This is expected with the removal of two histidine groups, while the retention of a still somewhat significant K_{eq} indicates that some binding interaction must be facilitated through other means. These values are indicative of binding affinity of each sequence, suggesting that a single histidine results in a stronger binding event and that the A11's 6-position histidine demonstrates the highest overall binding among these sequences. The free energy values follow the K_{eq} trend, with values of $-3.30 \times 10^4 \pm 2.77 \times 10^3$ J/mol, $-3.35 \times 10^4 \pm 2.12 \times 10^4$ J/mol, $-3.38 \times 10^4 \pm 3.04 \times 10^4$ J/mol, and $-3.05 \times 10^4 \pm 1.38 \times 10^4$ J/mol for peptides Pd4, A6, A11, and A6,11, respectively. These values are all statistically equivalent within error, but the average values provide insight into the binding interaction of a peptide, with respect to sequence substitution. Overall, these data provide valuable information regarding the changes in binding strength with respect to sequence ordering and substitutions. While Pd4 was originally isolated *via* phage display for Pd surfaces, we observe here that the presence of just one histidine results in an increased binding event, possibly due to a more free peptide structural motif at the biotic/abiotic interface. A6, lacking the 6-position histidine, demonstrated a slight increase from Pd4, but retained similar k_d and K_{eq} values. The A11 peptide, still possessing the 6-position histidine,

demonstrated a greater increase in k_a and K_{eq} values, in addition to a decrease in k_d. This suggests that a stronger binding event is likely at the 6-position. The removal of both histidine residues resulted in a significantly diminished k_a, increased k_d, and a corresponding decrease in K_{eq} as compared to the parent Pd4 peptide. Though a binding affinity increase was observed among A6 and A11, these values were comparable to those of Pd4, with minimal differences. This suggests that combined binding effects are present between the 6 and 11 positions in the Pd4 peptide, and the heightened A11 affinity suggests that the 6-position likely possesses binding priority in the sequence.

2.4.4 TEM Sizing of Nanomaterials

Sizing analysis of these samples were performed via transmission electron microscopy (TEM) and particles are visible in **Figure 2.5**. For each sample, multiple images were analyzed with >100 total particles measured. Sizing analysis was performed with Adobe Photoshop CS5.5 by pixel sizing,[26] revealing particle sizes of 1.9 ± 0.3 nm, 2.2 ± 0.4 nm, 2.4 ± 0.5 nm, and 3.7 ± 0.9 nm for the materials prepared from Pd4, A6, A11, and A6,11, respectively in **Figure 2.5**. It is interesting that the parent Pd4 peptide generated particles that were statistically equivalent in size to those prepared from the A6 and A11 peptides, whilst the A6,11 sequence, which does not contain the predicted binding residues, results in only slightly larger particles.

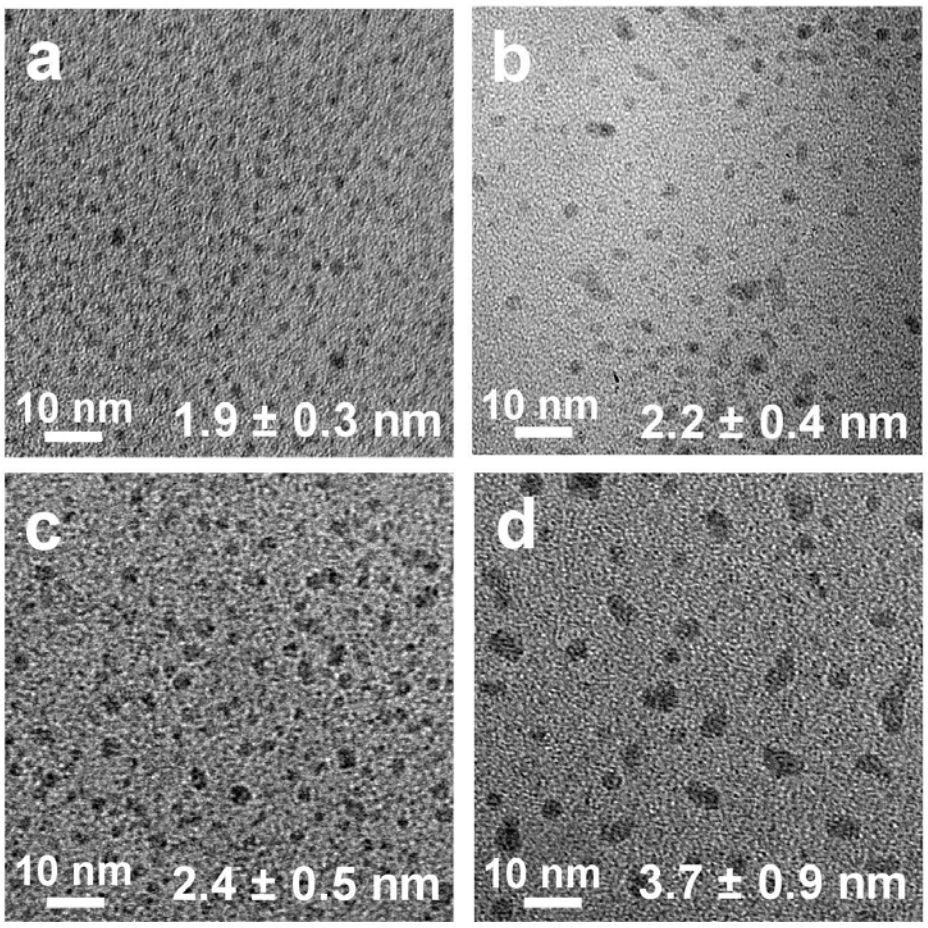

Figure 2.5. TEM analysis of Pd nanoparticles formed from a) Pd4, b) A6, c) A11, and d) A6,11 peptides.

This indicates that the histidine residues are important for nanoparticle growth; however, their presence in the sequence is not critical. Since nanoparticles of statistically equivalent sizes were prepared when the binding residues were replaced suggests that the peptides are bound to the nanoparticle surface in different orientations.

2.4.5 CD Analysis of Free and Bound Peptides

Indeed, CD spectra (**Figure 2.6**) of the prepared nanoparticles[128] demonstrated altered peptide motifs on the surface, based upon the modifications in the sequence. Collectively, peptides Pd4, A6, and A6,11 became less structured when bound to the nanoparticle

surface, as shown by a decrease in ellipticity; whereas the A11 peptide became more helical relative to the free peptides (**Figure 2.6a–f**).

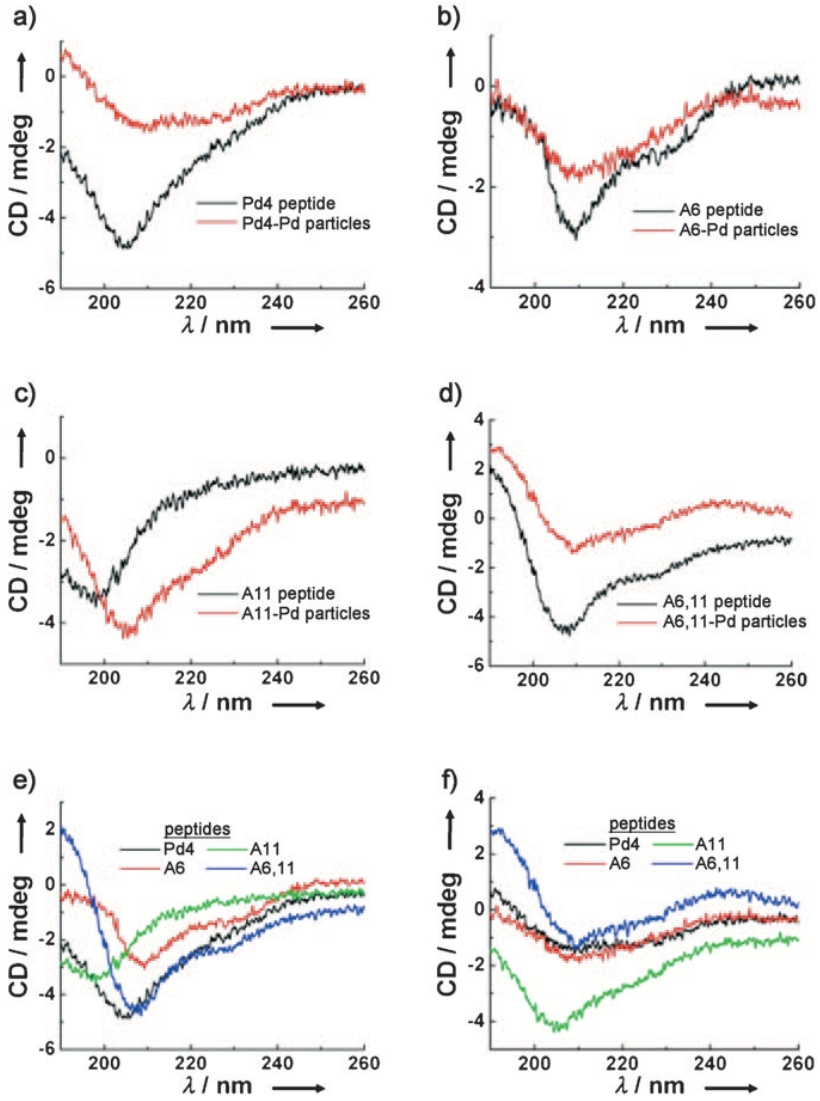

Figure 2.6. CD spectra analysis of peptides both free and bound to nanoparticle surfaces for a) Pd4, b) A6, c) A11, d) A6,11, e) all free peptides, and f) all bound peptides.

Notably, the free peptides of A6,11 and A6 adopted an a-helical structure, whilst A11 and Pd4 adopted random coil and mostly 310 helix structures, respectively (**Figure 2.6e**); however, on binding to the nanoparticle surface, the A11 peptide became more helical in structure, while Pd4 and A6 shared similar secondary structures with subtle differences.

2.4.6 Catalytic Activity through the Stille Coupling Reaction

To probe the catalytic activity of these particle systems with respect to peptide control of the inorganic surface, Stille coupling reactions were conducted on the Pd nanoparticles in water and at room temperature.[26,129] This coupling of 4-iodobenzoic acid (4-IBA) to a phenyl group takes place through a palladium atom insertion between the benzene-iodine bond, followed by transmetallation via $PhSnCl_3$, reductive elimination, and ejection of the Pd^0 atom. This generates an atom for the next cycle and biphenylcarboxylic acid (BPCA). The accessibility of high-energy edge and vertex atoms on the nanoparticle surface is directly correlated to catalytic activity of a nanoparticle system, which is modulated by the peptide layer passivant in this case. These substitutions and thus conformational and binding changes can therefore inhibit or facilitate nanoparticle activity. In each reaction, 0.25 mmol of 4-iodobenzoic acid was dissolved in 4.0 mL of 2.25m KOH. $PhSnCl_3$ (0.30 mmol) was added to the mixture to generate biphenylcarboxylic acid (BPCA). The nanoparticles were then added at concentrations of <0.5 mol% palladium and the mixture was stirred for 24 hours at room temperature. Upon completion, the reactions were quenched and the products were quantified via ^1H NMR. Analysis of the palladium loading as a function of product yield is presented in **Figure 2.7a**. The native Pd4 peptide demonstrated quantitative yields in 24 hours at a palladium loading of 0.005 mol%, consistent with previous results. Analysis of the material prepared with the A6 peptide found that the loading to achieve quantitative yield shifted to 0.001 mol%. Interestingly, with the other nanoparticles passivated with the A11 and A6,11 peptides, higher catalyst loadings of 0.01 mol% palladium were required for

the reaction to reach completion in 24 hours. Studies were performed which demonstrated various turnover frequency (TOF) values of the prepared materials. For these studies, the reactions were scaled up and then aliquots were extracted and quantified at various time intervals; the average of triplicate samples are shown in **Figure 2.7b**.

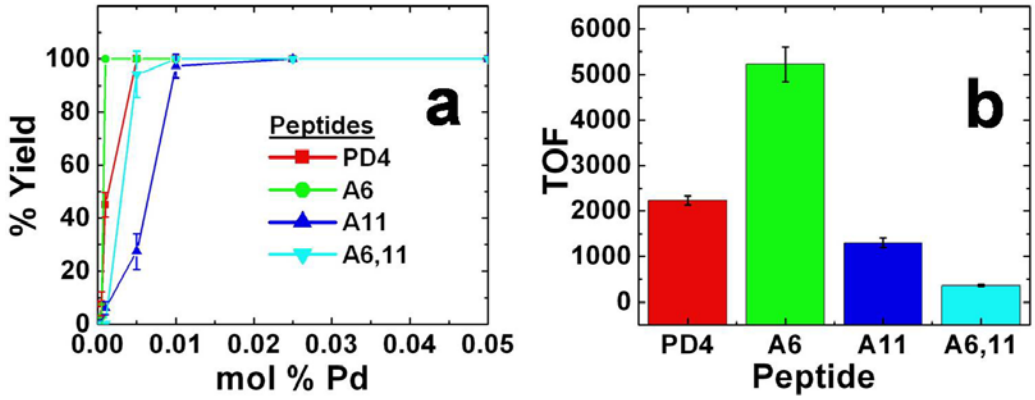

Figure 2.7. Catalytic activity studies for Pd4 and analogues for the Stille coupling reaction for a) 24 hour loading studies and b) 1-hour TOF analyses.

For the materials prepared using the Pd4 peptide, a TOF value of 2234 ± 99 mol BPCA $(molPd)^{-1}h^{-1}$ was observed. The TOF values are calculated using the total palladium concentration, consistent with previous studies.[130,131] A TOF of 2234 is slightly lower than previously reported;[26] this is likely due to slight changes in the reaction conditions. Surprisingly, analysis of the A6-based materials demonstrated a TOF of 5224 ± 381 mol BPCA $(molPd)^{-1}h^{-1}$, which corresponds to a > twofold increase in reactivity. When the A11 sample was probed, a decrease in the TOF was observed to 1298 ± 107 mol BPCA $(molPd)^{-1}h^{-1}$, which was further decreased to 361 ± 21 mol BPCA $(molPd)^{-1}h^{-1}$ for the A6,11-derived nanoparticles.

2.5 Summary

The QCM, catalysis, and TEM data suggest that the peptide sequence on the particle surface controls both the structure and reactivity of the palladium nanoparticles. The Pd4 sequence was optimized for palladium surface binding, which has been suggested to occur mainly through the histidine residues.[80] Alanine substitution of either of the histidine units demonstrated minimal changes in particle size, within the error of the measurement, which indicates that other amino acids in the sequence, asparagine and arginine, may be involved in surface binding to maintain the particle size and stability. When both histidine residues are replaced with alanine, the particle size marginally increased, which also supports binding through the other residues. Additionally, single substitutions demonstrated small binding affinity differences for the A6 and A11 peptides, but a large difference was observed for the A6,11 peptide. Once the nanoparticles are decorated with the different sequences on the surface, different confirmations and arrangements are possible based upon the individual binding capabilities. As such, changes to the palladium surface may occur, which could result in the different degrees of catalytic reactivity observed. This theory is supported by the CD spectra of the different peptides on the nanoparticle surface, which adopted different structures based upon the individual sequence. The catalytic reactivity of the biomimetic materials likely follows an atom-leaching mechanism (**Figure 2.2**); during the initial oxidative addition step, Pd^{2+} is abstracted from the surface to drive the reaction, which is controlled by the peptides.[8,130-132] Under this process, as discussed by Astruc and co-workers, if the peptides played no role in the reactivity, regardless of slight particle size differences, the TOF values should be constant for the different particles;[130,131] however,

they are drastically different, which suggests that the surface peptides modulate the reactivity. For instance, when dendrimer-based palladium nanoparticles of similar sizes to the peptide-capped particles were used, equivalent TOF values were observed, which is attributed to the lack of involvement of the dendrimer passivant in the reaction.[130,131] For the biomimetic materials, the peptide sequence is critically important to the overall TOF value. The replacement of histidine at position 6 improves the catalytic activity while histidine at position 11 is required for generating highly reactive nanoparticles. Furthermore, since nanoparticles of similar sizes were prepared, the number of moles of surface palladium atoms is similar, thus suggesting that the major difference between the particles is the biotic/abiotic interface, which is controlled by different peptide binding motifs. As the atom-leaching method would likely alter particle morphologies, we attempted to observe the materials by using TEM after the reaction. Unfortunately, at the very dilute nanocatalyst concentrations that were employed in these reactions, we were unable to observe any nanoparticles on the TEM grid. From this, two peptide-mediated events are possible to modulate the ability to abstract palladium atoms from the nanoparticle surface: First, the surface structure may be such that the orientation of the A6 peptide maximally exposes the palladium surface, thus enhancing the initial oxidative addition step and releasing Pd^{2+} faster. As a result, more palladium would react in a shorter time to result in higher TOF values. Second, by removal of specific histidine residues, other residues are likely to bind to the surface to maintain particle stability. As such, the electronic character of the palladium surface could vary based upon the individual binding, which is known to inhibit the initial oxidative addition at the particle surface.[130] This would result in varied TOF values as a function of the electronic effects

of the binding motifs of the peptides. At present, we are unable to fully distinguish between these events; however, both are controlled by the peptide.

2.6 Conclusions

In conclusion, significant modulations in the reactivity of biomimetic nanomaterials have been demonstrated by subtle modifications to the peptide sequence. This suggests that the peptide and its binding effects control the functionality of the nanomaterials. Peptides that are isolated by phage display are optimized for binding. While this is useful for structural stability, such attributes may cause a decrease in activity. The results presented here indicate that by altering the sequence, particle stability may be maintained with desirable increases in nanoparticle reactivity, which could be used as a basis for the rational design of optimized peptide sequences employed in the synthesis of nanomaterials of superior functionality.

Chapter 3. Material-Passivant Relationships among Pd Nanoparticles and their Surface-Specific Peptide Ligands

3.1 Overview of Study

The ability to control the size, shape, composition, and activity of nanomaterials presents a formidable challenge. New peptide approaches represent avenues to achieve such control at the synthetic level; however, the critical interactions at the bio/nano interface that direct such precision remain poorly understood. Here evidence is presented which suggests that materials-directing peptides bind at specific time points during Pd nanoparticle (NP) growth, dictated by material crystallinity. As such surfaces are presented, rapid peptide binding occurs, resulting in the stabilization and size control of single-crystal NPs. Such specificity suggests that peptides could be engineered to direct the structure of nanomaterials at the atomic level, thus enhancing their activity. Along these lines, catalytic results suggest that peptide concentrations may also play a vital role in materials reactivity, indicating that a balance exists between particle passivation and activity. Additionally, nanoparticle composition differences were observed among these systems, which also correlate to catalytic activities of the Pd nanoparticles. To this end, the binding properties of the peptide sequence may affect the reduction potential of the precursor metal salt, resulting in changes to the reduced materials, which can greatly modulate catalytic activity.

3.2 Introductory Remarks

Nature has evolved varied approaches to fabricate complex inorganic architectures composed of nanoscale building blocks, all of which are mediated at the molecular level.[43,133-135] Control over these processes is achieved through peptide and protein

chemical interactions with the inorganic component for defensive, structural, and bioremediation functions at ambient conditions, which contrasts conditions traditionally employed for materials synthesis.[133] By mimicking biological processes, translation of desirable ambient methods toward fabrication routes for nonbiological materials could be achieved to advance current technological applications. This has been addressed by the virus and peptide-based fabrication of batteries,[40,123] catalysts,[25,26,28,136-138] sensors,[122,139] and complex nanoparticle assemblies.[124,140-142] While biological approaches represent new avenues to realize next-generation materials, a fundamental understanding of the structure/function relationship of the peptide/inorganic surface is required, where minor modifications could be used to fine-tune the structure, shape, composition, and functionality of the final materials.

Accessing an atomically resolved image of the peptide conformation on the surface of nanoparticles remains a significant challenge. While biocombinatorial approaches have isolated numerous peptides with affinities for different inorganic compositions,[22] such methods provide little information concerning how the peptides interact at the molecular level formaterials specificity. Additionally, these approaches are likely toisolate sequences with the greatest affinity for the target; however, such sequences may not be optimal for the intended functionality/application of the material. It is likely that select amino acid residues and the peptide secondary structure work in combination to control the binding, stability, and final activity of the nanoparticle. By accessing such information, new sequences could be rationally designed that can direct the fabrication of materials with control over the structure, composition, and functionality. Computational models are available that probe peptide binding of target 2D flat surfaces;[36,80,143]

however, modeling studies of binding to 3D dispersed materials in an aqueous environment remain limited.[144] While these analyses are integral to understanding the bio/nano surface, experimental evidence is required to refine this structural level. Unfortunately, only a handful of experimental methods are available to achieve these goals, where the limit of resolution complicates such analyses. Computational modeling was employed for the peptide binding as a foundation for the development of experimental approaches to probe the peptide/inorganic interface.[26,80,137,138] Using phage display, the Pd4 peptide (TSNAVHPTLRHL) was isolated with affinity for Pd.[26] Pandey et al. have employed Monte Carlo modeling of Pd4 binding to a 2D surface, which indicated that the histidines at the 6 and 11 positions anchor to Pd to create a kinked-loop structure.[80] Upon the basis of these theoretical results, a series of four peptides, listed in **Table 3.1**, were synthetically prepared that modified peptide binding at these selected sites.[138]

			Pd/peptide ratio size(nm)			
peptide	sequence	pI[a]	1	2	3	4
Pd4	TSNAVHPTLRHL	9.47	1.9 ± 0.3	1.9 ± 0.3	2.1 ± 0.4	2.0 ± 0.3
A6	TSNAV**A**PTLRHL	9.44	2.4 ± 0.6	2.1 ± 0.5	2.2 ± 0.7	2.1 ± 0.4
A11	TSNAVHPTLR**A**L	9.44	2.3 ± 0.4	2.4 ± 0.5	2.6 ± 0.4	2.4 ± 0.5
A6,11	TSNAV**A**PTLR**A**L	9.41	2.8 ± 0.7	3.0 ± 0.6	2.8 ± 0.7	3.1 ± 0.7

Table 3.1. TEM sizing analysis and pI calculation of the nanomaterials formed from Pd4 and alanine-analogue peptides in Pd:peptide ratios 1 – 4.

To that end, the A6, A11, and A6,11 peptides were prepared that swapped histidine with alanine at the 6, 11, and 6 and 11 positions, respectively. This resulted in the removal of

binding at these locations to alter the peptide conformation once bound to a Pd nanoparticle.[138]

Interestingly, the Pd nanoparticles fabricated using these different sequences are highly catalytically active for Stille C-C coupling and suggest that the bio/nano surface plays a role in controlling the reactivity. The structure and the functionality of the materials are anticipated to arise from the strict interactions of the peptide on the nanoparticle surface, which is likely embedded during the peptide isolation process for the parent sequence. Such interactions are potentially modulated based upon changes to the peptide sequence that are reflected in the functionality. Furthermore, the peptides could play a significant role throughout nanoparticle synthesis. In this regard, the Pd^{2+} ions bind the peptide to form Pd^{2+}/peptide complexes that could contribute to the structure of the final materials. These complexes are anticipated to change based upon the peptide sequence, which controls the binding stoichiometry and motifs, as well as through the number of Pd^{2+} ions bound to the peptide. Such interactions could alter the structure of the zerovalent materials fabricated upon reduction where minimal understanding of the interplay between peptide sequence, metal ion complexes, and the final materials is known. In this contribution, changes in the particle size and functionality can be directly achieved via minor variations in the materials-directing

peptide sequence. This was achieved by a complete experimental analysis of the fabrication and catalytic activity of Pd nanoparticles using the peptide library of **Table 3.1** from Pd^{2+}/peptide complexation prior to reduction to the final Pd^{0} nanoparticles. By using UV-vis and X-ray absorbance analyses of the loading of Pd^{2+} in the reaction mixture, monitoring of metal/peptide complexation can be achieved to determine the

maximum Pd/peptide ratios that can be used for materials synthesis as a function of the peptide sequence. The formation of different peptide secondary structures are also observed, based upon the peptide sequence and number of Pd^{2+} ions per peptide, which has implications on nanoparticle formation. Upon reduction, the fabrication of single-crystal Pd nanoparticles occurs where fine-tuning of the particle size is achievable based on the peptide sequence. For instance,

minor modifications that replace only a single amino acid residue can have observable changes on the particle morphology. Furthermore, the sequence position of the modifications to the peptide is also critically important in controlling the structure/function relationship of the final particle. To that end, modifications at the 11 position result in larger particles with diminished catalytic functionalities, while

variation at the 6 position produces smaller particles that possess the highest degree of activity. This change in activity is attributed to the surface structure of the materials, which is directly tuned by the peptides at the biotic/abiotic interface. This analysis is important for three key reasons. First, it demonstrates a high level of structural/size control over nearly monodisperse, single-crystal nanoparticles at significantly small sizes by simple changes to the materials directing sequence; such control remains challenging using standard ligand-based nanoparticle synthetic approaches. Second, the morphology of the metal ion/peptide complex prior to reduction is shown to be important to the final structure and function of the materials as a result of the degree of metal ion complexation. Third, the results present key peptide sequence effects information, which could be used in the foundation of principles for the de novo design of materials-directing peptides that control the structure/function relationship of nanomaterials.

Lastly, these results represent key peptide sequence effects information, that could be further exploited for the design of materials-directing peptides to further elucidate and improve upon the structure-function relationship of nanomaterials. These systems were fully characterized using UV-vis, high-resolution transmission electron microscopy (HR-TEM), circular dichroism (CD), ζ-potential analysis, and X-ray absorption fine structure (XAFS) spectroscopy, while the catalytic properties were analyzed via Stille coupling.

3.3 Methods

3.3.1 Chemicals

Wang resins, substituted with an FMOC-protected leucine residue, FMOC-protected amino acids, piperidine, diisopropyl ethylamine (DIPEA), O-benzotriazole-N,N,N',N'-tetramethyl-uronium-hexafluoro-phosphate (HBTU) and N-hydroxy benzotriazole (HoBT) were purchased from Advanced Chemtech (Louisville, KY). K_2PdCl_4 and triisopropylsilane were purchased from Sigma-Aldrich (Milwaukee, WI), while $NaBH_4$ was acquired from EMD Chemicals (Gibbstown, NJ). Phenyltin trichloride ($PhSnCl_3$), $CDCl_3$, trifluoroacetic acid (TFA), anhydrous Na_2SO_4, NaCl, and KOH were purchased from Fisher (Pittsburgh, PA), while 4-iodobenzoic acid (4-IBA) and 4-*t*-butylphenol (4-TBP) was acquired from TCI America (Wellesley Hills, MA). N,N-dimethylformamide (DMF), acetonitrile, diethyl ether and methanol were purchased from Pharmco-AAper (Shephardsville, KY). All chemicals were used as received. Milli-Q water (18 mΩ•cm; Millipore, Bedford, MA) was used throughout for all experiments.

3.3.2 Peptide Isolation and Synthesis

The Pd4 peptide was isolated using standard phage display methods. The phage was isolated by panning against a commercially available Pd nanopowder (sub-micron particles; Aldrich). Binding of the isolated phage to the Pd nanoparticles was confirmed by immunofluorescence, while peptide interactions with a Pd surface was confirmed by quartz crystal microbalance. The synthetic peptide was prepared using a TETRAS peptide synthesizer (CreoSalus; Louisville, KY) employing standard FMOC peptide synthesis protocols. To facilitate peptide production, leucine-functionalized Wang resins were used. The peptides were cleaved from the resin using a cocktail of 95% TFA, 2.5% triisopropylsilane, and 2.5% water, followed by precipitation by cold diethyl ether. The precipitated materials were then purified via reverse-phase HPLC with a water/acetonitrile gradient, and confirmed by MALDI-TOF mass spectrometry.

3.3.3 Nanoparticle Synthesis

Peptide-capped Pd nanoparticles were synthesized following a modified standard preparation. A peptide stock solution (10.0 mg/mL) was prepared by dissolving 1.00 mg of peptide into 100 μL of water, while a K_2PdCl_4 stock solution (0.1 M) was made by dissolving 16.3 mg of the metal salt into 500 μL of water. For a 1.00 mL volume particle synthesis, 20.0 μL of the peptide stock was diluted with 955.0 μL of water. To this, either 1.56 μL, 3.13 μL, 4.64 μL, or 6.25 μL of the Pd stock was added to form reactions with a Pd:peptide ratio of 1, 2, 3, or 4, respectively. After incubating for 30.0 min, 20.0 μL of a freshly prepared 0.1 M $NaBH_4$ solution was added and the reaction was allowed to reduce for 60.0 min.

3.3.4 Stille Coupling

The C-C coupling Stille reaction was employed to probe the catalytic activity of nanoparticles prepared at the different Pd:peptide ratios. For each reaction, 0.310 mg (1.25 mmol) of 4-iodobenzoic acid and 246.5 μL (1.50 mmol) of $PhSnCl_3$ were dissolved in 2.25 M aqueous KOH. The volume of KOH was adjusted to reach a final reaction volume of 20.0 mL based upon the volume of Pd particles used in the reaction. To this solution, either a 1.00 mL, 1.33 mL, 2.00 mL, or 4.00 mL volume of the Pd nanoparticle solution prepared at Pd:peptide ratios of 1, 2, 3, or 4, respectively, was added such that a Pd reaction loading of 0.05 mol% was achieved. The reactions were allowed to stir vigorously for 1.00 h at room temperature, with 2.00 mL aliquots removed at time points of 0.00, 5.00, 10.0, 15.0, 20.0, 25.0, 30.0, 40.0, 50.0, and 60.0 min. Each aliquot was immediately quenched with 12.5 mL of 5.00% aqueous HCl, extracted using three 30.0 mL washes of diethyl ether, followed by two 20.0 mL washes with a saturated NaCl solution. The extracted material was dried with anhydrous Na_2SO_4 and filtered. To each sample, 75.0 mg (0.500 mmol) of 4-TBP was added as an internal standard for product quantitation, after which the ether was removed using a rotary evaporator. For quantitation, ~1.0 mg of the product was dissolved in $CDCl_3$, which was analyzed using ^1H NMR.

3.3.5 Characterization

UV−vis spectroscopy of the Pd nanomaterials was obtained on an Agilent 8453 UV−vis spectrometer employing a 0.20 cm path length quartz cuvette (Starna). All complexation and reduced particle spectra were background subtracted against the Pd4 peptide in water at the reaction concentration. Transmission electron microscopy (TEM) images were

obtained using a JEOL 2010F TEM operating at 200 kV with a point-to-point resolution of 0.19 nm. The nanoparticle samples were prepared on standard 400 mesh Cu grids coated with a thin layer of carbon (EM Sciences). A 5.00 μL volume of each particle sample was pipetted onto the surface of the grid and allowed to dry in air and stored in a desiccator. NMR spectra of the reaction products were obtained using a Varian 200 MHz NMR spectrometer. The product and the internal standard (~1.0 mg) were dissolved in 1.00 mL of $CDCl_3$ and added to a 5.00 mm NMR tube (Wilmad). The peak integration at δ 8.17 ppm of the product was compared with the peak integration at δ 6.8 ppm of the internal standard (4-TBP) to obtain the reaction yield. XAFS data was collected at the National Synchrotron Light Source (NSLS) at Brookhaven National Laboratory (BNL) on beamline X18B. For this analysis, nanoparticles were synthesized in 75.0 mL volumes and lyophilized to generate a dry powder. These solid samples were applied to adhesive tape and folded multiple times to ensure sample homogeneity. The materials were then analyzed in fluorescence mode using a Lytle detector from energy ranges of 40.0 eV below and 120 eV above the K-edge absorption wavelength of zerovalent Pd (24,353 eV). Fourier transformation of the energy space data was performed using FEFF theory to generate the R-space data from which the nearest neighbor coordination numbers can be achieved. Briefly, Pd K-edge XAFS studies were performed at the X18B beamline at the National Synchrotron Light Source at Brookhaven National Laboratory. All samples, both unreduced Pd^{2+}/peptide complex and reduced Pd nanoparticles, were dried via lyophilization to form a powder. The powders were then uniformly spread on adhesive tape, and their X-ray absorption coefficient was measured in transmission mode between 150 eV below and 1350 eV above the Pd K-edge (24353 eV). The Artemis program from

the IFEFFIT XAFS analysis software suite was used to analyze the EXAFS data by fitting theoretical contributions to the experimental spectrum.[145] The theoretical signal was obtained using FEFF6 code that calculates photoelectron scattering amplitudes and phases for a given atomic configuration. In the fits, the amplitude factor (S0 2 = 0.885) was added, which was obtained from analysis of Pd foil. Also added are coordination numbers of nearest neighbors to Pd, their distances, and mean square disorders (σ^2) in those distances. In addition, photoelectron energy origin corrections were varied for different contributions, as described in greater detail below. To construct theoretical contributions for Pd-O/N, a reference crystal structure of PdO was used. To construct Pd-Cl, the structure of K_2PdCl_4 was used, and to construct Pd-Pd theory, the structure of bulk Pd was used. These contributions, each carrying its own energy origin correction (since they were obtained from different structures), were combined in Artemis into the total theoretical signal. The data from all reduced and complexed species were processed using this modeling strategy. CD spectra were obtained on a Jasco J-815 CD spectrometer using a quartz cuvette. Peptides were dissolved in double deionized water with varying amounts of Pd^{2+} (6.25, 12.5, 18.75, and 25.0 μL) to reach desired Pd^{2+}/peptide ratio and diluted to a peptide concentration of 16 μM in water for CD measurements. Nanoparticles were prepared at equivalent ratios and likewise diluted for CD. The CDPro software package was used for analysis of CD spectra to deconvolute secondary structure contributions.

3.3.6 Simulation

Molecular dynamics simulation was carried out to investigate the structure and stability of small Pd nanoparticles and their interfaces with the Pd4 peptide in aqueous solution.

We employed the CHARMM-METAL force field which contains Lennard-Jones parameters for *fcc* metals and reproduces key interfacial properties in agreement with experiment, including surface energies of (111), (100), and (110) facets, interfacial energies with water, layer structures of metal-water interfaces and the corresponding increase in dielectric constant of water to the bulk value, the density of the metals, as well as adsorption energies of amino acids and peptides. Models were prepared of spherical Pd shape of 1, 1.5, 2, and 3 nm diameter starting with an *fcc* Pd bulk structure according to X-ray data by definition of a center atom and application of a spherical cutoff at 0.5, 0.75, 1, and 1.5 nm. Subsequently, the model nanoparticles were equilibrated in an open box under NVT conditions using a time step 1 fs, a spherical cutoff at 1.2 nm for van-der-Waals interactions, a temperature of 298 K, and a total simulation. The simulation showed structural instability and transition to an amorphous, non-*fcc* structure for the 1 nm particle, significant structural fluctuation of the 1.5 nm particle, and stable *fcc* structures of the 2 nm and 3 nm particles. To ascertain the thermodynamic stability of the structures in the simulation, several simulations were carried out at an increased temperature of 800 K for 300 ps, followed by cooling to 298 K over a period of 70 ps. The 1 nm particle remained amorphous and did not assume *fcc* structure. For the 1.5 nm particle, a non-*fcc* structure was identified to be 0.47 kcal per mol Pd atom more stable than the *fcc* structure. For the 2 nm and 3 nm particles, *fcc* structures were reversibly obtained after melting at 800 K and subsequent cooling to 298 K. Similarly, long simulations of 1 μs at 298 K were performed for the most stable structure of each nanoparticle, which confirmed their equilibrium structure (**Figure 3.5**). The existence of a critical number of atoms or molecules to form stable clusters and single crystalline

structures is also known for other materials. In aqueous solution, MD simulation on particles smaller than 1.5 nm with irregular surfaces shows that coordination of the peptide is weak in favor of water molecules. On larger particles, multiple residues of the Pd4 peptide, especially R, N, and H, coordinate with epitaxial sites of (111) facets of the Pd nanoparticles once these facets are displayed on the metal surface. On these single crystalline nanoparticles, several peptides and peptide layers could also simultaneously cover the surface. The reduction of Pd^{2+} to nanoparticles of 2 nm size (~300 atoms) with an initial Pd:peptide ratio between 1:1 and 4:1 and a peptide concentration of ~150 μmol/L in the solution leads to a molar ratio of particles to peptide between 1:300 and 1:75. Therefore, an excess of peptides is readily available to cover the nanoparticle surface, and the ratio increases for larger particle size.

3.4 Results and Discussion

The Pd4 peptide was identified by phage-display with affinity for Pd where recent results suggest that the sequence binds crystallographic features to prepare Pd nanoparticles of ~2 nm. These materials are catalytically active under desirable environmentally friendly and energy neutral conditions; however, the biotic/abiotic interface of these structures plays a significant role in mediating the reactivity. While it is clear that the peptide participates in the functionality, it remains unclear as to the mechanism by which the sequence controls the structure of the materials. The material structure, which encompasses size, shape, and composition, is critically important to the overall functionality where all three characteristics can be individually modified to have dramatic implications on the final activity. Ideally, these traits could be controlled simultaneously

by using the selected ligands; however, such ligands must be sufficiently complex to allow for this level of structural control. Peptides are optimal choices for this capability due to their facile synthesis and sequence programmability, as well as the diverse range of binding moieties and arrangements achievable by peptide secondary structure. To probe this materials synthetic capabilities, material-ligand relationships were probed for Pd4 and a set of three analogue peptides of the parent sequence that modified the binding motif at the histidine residues to result in the A6, A11, and A6,11 peptides.

3.4.1 UV-vis Characterization of the Peptide-Based Materials.

An important key factor in materials structural control lies in the metal/ligand complex prior to reduction. To determine the potential number of Pd^{2+} binding sites for each of the four sequences, a titration of a peptide solution with K_2PdCl_4 was employed, which was monitored using UV-vis spectroscopy. This was achieved by monitoring the ligand-to-metal charge transfer band (LMCT) that is observed at 215 nm, which is present for the binding of Pd^{2+} by the amines of the individual peptides.[26,146] As a control, **Figure 3.1a** presents this analysis for the K_2PdCl_4 precursor in solution in the absence of peptide.

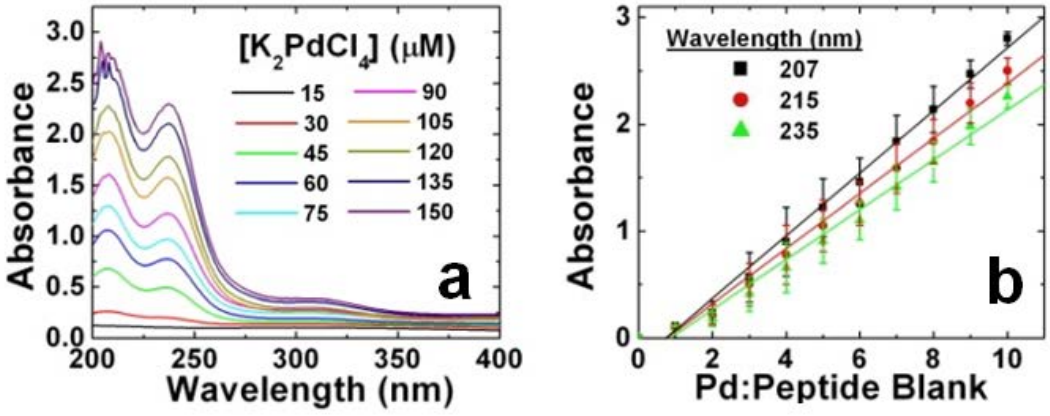

Figure 3.1. Analysis of incremental concentrations of K_2PdCl_4 in water via a) UV-vis and b) the trend observed from characteristic absorbance wavelengths.

Here, two absorbance peaks are observed at 207 and 235 nm that arise from the uncomplexed Pd^{2+} salt, whose absorbance values are dependent upon the concentration. Note that the Pd^{2+} concentrations presented are those that are employed to prepare Pd:peptide ratios between 1 and 10 in the materials synthesis reactions, thus a direct comparison can be drawn to the control study. Additionally, no peaks are evident at the two lowest Pd^{2+} concentrations due to the molar absorptivity of the metal salt. As presented in the **Figure 3.1a**, again in the absence of peptide, the 207 and 235 nm absorbance intensities increase linearly with the Pd^{2+} concentration as anticipated by Beer's Law. [147] It should be noted that absorbance observed above 2.0 is likely saturation of the photomultiplier tube; however, the spectra of interest are below this level.

Figure 3.1b presents the trends observed of the key wavelengths 207, 215, and 235 nm, respectively. For these, the absorption bands at 207 and 235 nm are indicative of Pd^{2+} absorbance in water, while 215 nm is characteristic of peptide-Pd^{2+} complexation. When these same concentrations are employed with the Pd4 peptide, UV-vis analysis of the Pd^{2+} complexation reaction demonstrates the appearance of the 215 nm absorbance band, visible in **Figure 3.2a**. In this study, the peptide concentration remained constant while the Pd^{2+} concentration varied at the values shown in **Figure 3.2a**, to result in Pd:peptide ratios of 1-10. While the peptides demonstrated minimal to no absorbance over the wavelength range of interest (Additional Information, **Figure A2.1**), all UV-vis analyses of the Pd^{2+}/peptide complexes were background subtracted against the free peptide at the reaction concentration.

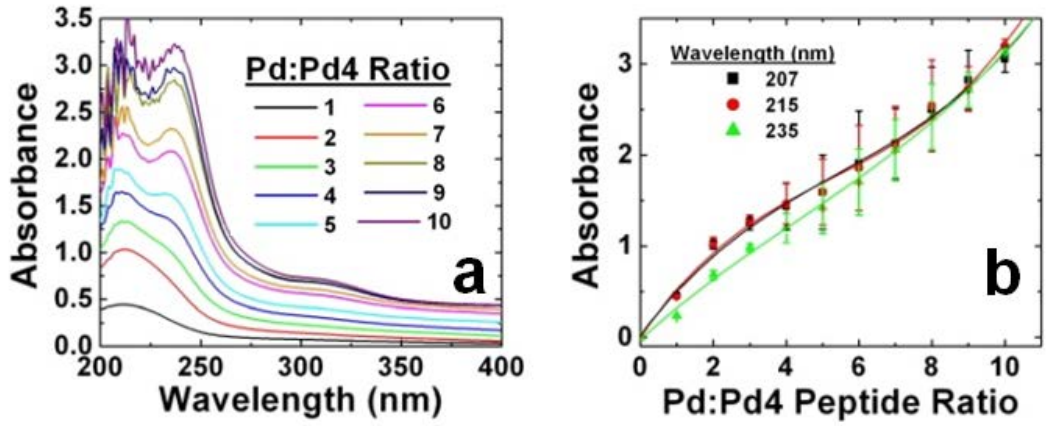

Figure 3.2. Analysis of incremental concentration ratios of K_2PdCl_4 in the presence of Pd4 peptide via a) UV-vis and b) the trend observed from characteristic absorbance wavelengths.

The black spectrum displays the reaction at a ratio of 1 where a single peak is observed at 215 nm that arises from the LMCT band of Pd^{2+}/amine binding. Note that in the absence of the peptide, no absorbance is noted for the Pd^{2+} species in solution (black spectrum, **Figure 3.1a**). As the Pd:peptide ratio is increased to 2 (red spectrum), the LMCT band intensity increases with no additional peaks being noted. This increasing trend is maintained for ratios up to 4 (blue spectrum); however, a peak shoulder is observed at 235 nm at this ratio, consistent with free Pd^{2+} in solution. At subsequently higher ratios (≥5), the 215 nm LMCT band begins to shift to 207 nm and the 235 nm peak increases in intensity, suggesting that the peptide becomes saturated with Pd^{2+} binding and excess metal salt remains uncoordinated and free in solution.

The plot of the growth of the three peaks associated with metal binding is presented in the **Figure 3.2b**. While a linear trend in absorbance growth is observed for the free Pd^{2+} salt in solution in **Figure 3.2b**, a deviated trend is noted for the reaction in the presence of the Pd4 peptide. In this system, the LMCT growth associated with peptide binding induces the 215 nm band to rapidly increase in absorbance at low Pd:peptide ratios. The

derivative of the trend line for the 215 nm plot as a function of Pd:peptide ratio demonstrates an inflection point at 5.5. This suggests that at values greater than this ratio, additional Pd^{2+} ions in solution remain unbound by the peptide. Similar observations are noted with the 207 nm absorbance, which is likely due to the broad absorptivity of the LMCT band. This also explains why only a minimal deviation is observed for the 235 nm absorbance as it is sufficiently positioned to avoid significant signal overlap. Nevertheless, these changes in the linear absorbance trend are rooted in the binding of Pd^{2+} to the peptide amines. From this, it can be estimated that ~4 or less Pd^{2+} ions can coordinate to the peptide as the deviated trend is maintained at these values. At higher ratios, the slope of the trend lines for the 207 and 235 nm absorbance of the Pd^{2+} returns to those of the peptide free solution, thus suggesting uncoordinated metal salt exists in the reaction mixture. These same procedures were performed for the alanine-analogues of Pd4 in **Figure 3.3**. **Figure 3.3a-f** present the analysis of Pd^{2+} complexation with the A6, A11, and A6,11 peptides. Interestingly, for the A6 and A11 titration studies, presented in **Figure 3.3** b and d, respectively, a similar trend to the Pd4 peptide is observed. For both samples, inflection points are observed at a Pd:peptide ratio of 4, suggesting that these samples can coordinate less Pd^{2+} ions compared to the parent Pd4 sequence. This was not surprising as a metal coordination site at the substituted histidine residue was removed. Changes in the absolute intensities for the different samples likely arise from different coordination environments (confirmed via CD, discussed below) and sample blanks (based upon the different sequences). For the A6,11 peptide that removes both histidine residues, as shown in **Figure 3.2e**, a significantly deviated trend is observed as compared to the Pd4, A6, and A11 systems.

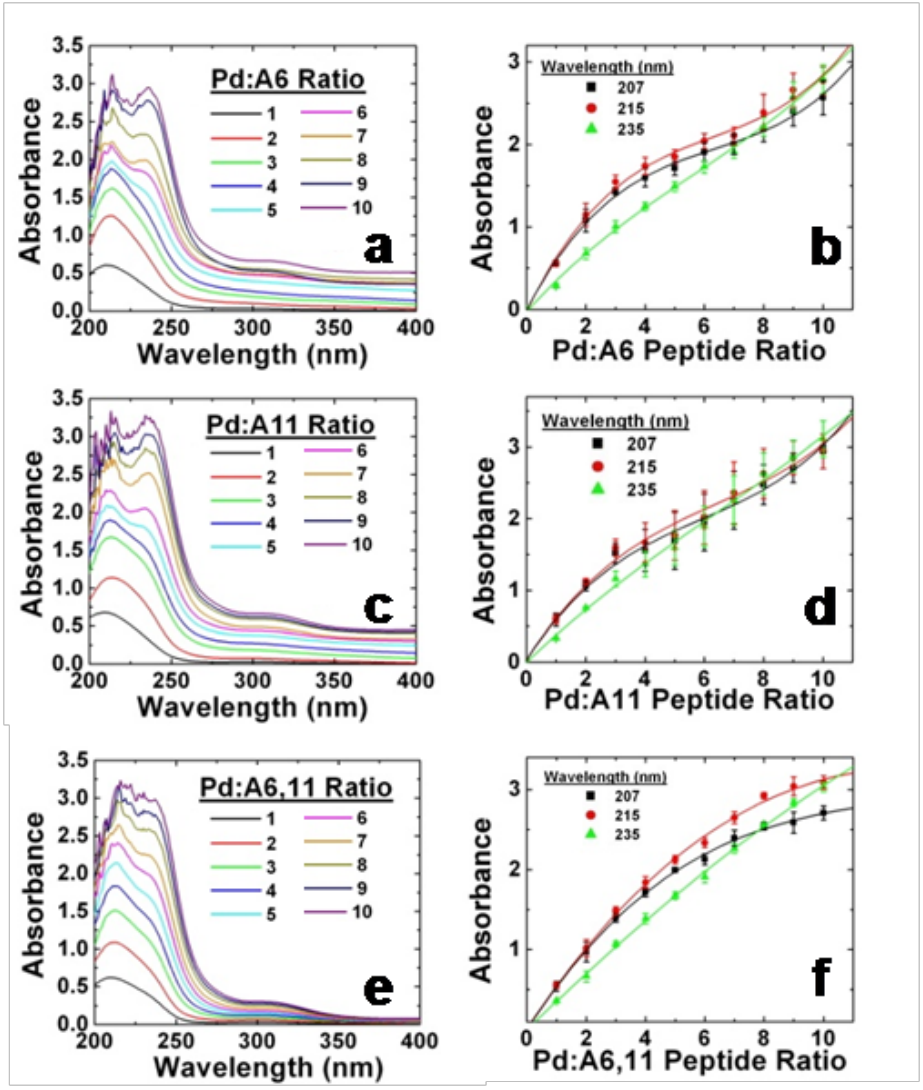

Figure 3.3. Analysis of incremental concentration ratios of K_2PdCl_4 in the presence of a) A6, c) A11, and e) A6,11 peptides and the corresponding trends observed from characteristic absorbance wavelengths.

In this system, saturation of the Pd^{2+} binding to the peptide is not spectroscopically observed at Pd:peptide ratios <10. Taken together, this suggests that the histidine, arginine, and asparagine residues, as well as the N-terminus and peptide backbone likely play a significant role in metal ion complexation prior to reduction. Furthermore, the A6,11 peptide has a significantly different solution structure (discussed below), as

compared to the other three sequences, which suggests that peptide conformation could lead to binding site exposure that may be involved in metal-ion complexation.

After peptide complexation by the metal-ions, reduction is required to drive nanoparticle nucleation and growth. As shown in **Figure A2.2** (Additional Information), images of the reactions after addition of a 10-fold excess of $NaBH_4$ to the mixtures with different Pd:peptide ratios of ≤ 7 for the four peptides are present.

For all of the materials prepared using the Pd4, A6, and A11 peptides, stable nanoparticles are generated at ratios ≤ 4; however, at greater ratios, precipitation of bulk Pd black is observed. This correlates very well with the titration experiments that indicated metal ion saturation of the peptides at a ratio of 4. Similar results were noted for the Pd nanoparticles prepared using the A6,11 sequence; however, stable nanoparticles were generated up to a ratio of 5. Precipitation of bulk Pd was not noted until ratios ≥ 6. Due to this precipitation event, only those materials that formed stable colloidal solutions of materials were further analyzed.

Initial characterization of the reduced materials was conducted by UV-vis spectroscopy and high-resolution TEM analysis. **Figure 3.4** presents the UV-vis spectra of the materials prepared at the different ratios that generated stable nanoparticles for the four different peptides. **Figure 3.4a** specifically represents the analysis for the Pd4-based materials at ratios ≤ 4.

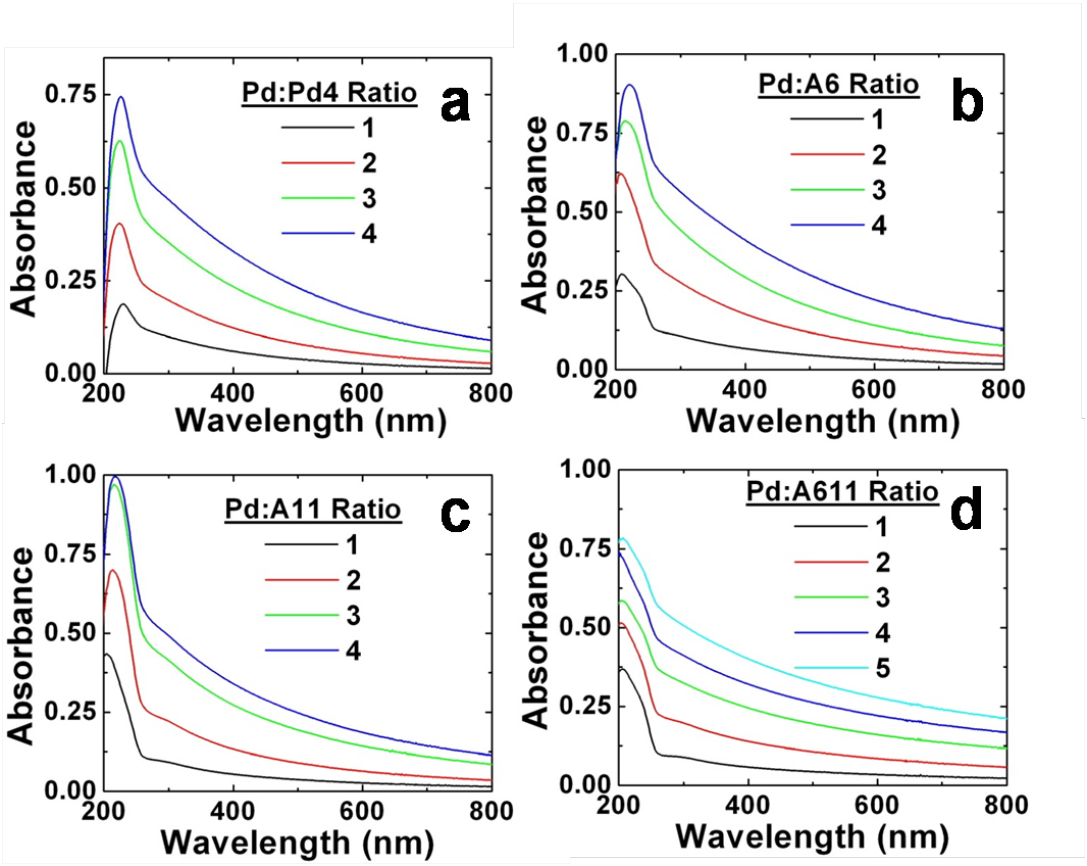

Figure 3.4. UV-vis analysis of reduced Pd nanoparticles prepared at the stable Pd:peptide ratios in the presence of the (a) Pd4, (b) A6, (c) A11, and (d) A6,11 peptides.

Here, for all four samples, an increase in absorbance towards lower wavelengths was noted, while the LMCT band and the absorbances associated with Pd^{2+} were not observed, all of which is consistent with Pd nanoparticle formation. Additionally, the intensity of the absorbance at all wavelengths increased as the Pd:peptide ratio increased such that the materials prepared at a ratio of 4 possessed the highest intensity. Identical results were observed for all materials prepared with the different peptides (**Figures 3.4b-d** for the A6, A11, and A6,11-based materials, respectively) such that no absorbance bands are observed for unreduced Pd^{2+} species and that the absorbance intensity increases proportional to the Pd:peptide ratio. This suggests that Pd nanoparticles are prepared

under the selected conditions; however, UV-vis is not able to discern changes in the Pd nanoparticle structure. To further probe the material morphology on the nanoscale, TEM analysis was conducted.

3.4.2 HR-TEM Analysis of the Peptide-Based Materials

TEM studies of the Pd4-capped Pd nanoparticles are presented in **Figure 3.4a** with a high-resolution image of an individual particle displayed in the inserts. Here, single crystal Pd nanoparticles with an average size of 1.9 – 2.1 nm are prepared regardless of the Pd:peptide ratio used during synthesis.

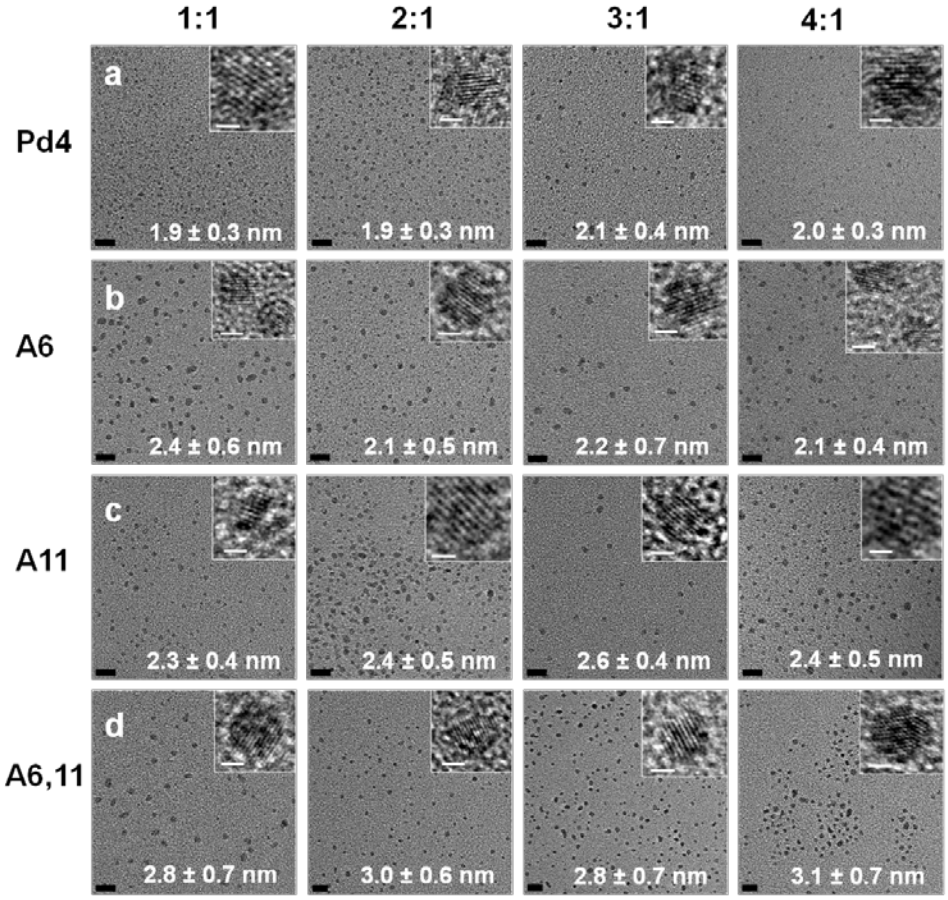

Figure 3.5. TEM analysis of materials prepared at Pd:peptide ratios 1-4 with peptides a) Pd4, b) A6, c) A11, and d) A6,11, respectively. The insets are crystalline particles observed via HR-TEM. The black scale bar is 10 nm and the white inset scale bar is 2 nm.

Specifically, particle sizes of 1.9 ± 0.3 nm, 1.9 ± 0.3 nm, 2.1 ± 0.4 nm and 2.0 ± 0.3 nm were achieved for materials prepared at ratios of 1, 2, 3, and 4, respectively, which is consistent with previous studies.[137] When the materials prepared with the A6 peptide were analyzed (**Figure 3.5b**), again single crystal Pd materials were generated; however, the average particle size shifted to between 2.1 nm and 2.4 nm. Furthermore, a narrow size distribution was achieved for these materials, especially for particles of such small sizes. Analysis of the A11-based particles, as presented in Figure 3c, indicated a further shift to slightly larger particles with average sizes between 2.3 and 2.6 nm that were again single crystal nanomaterials. Finally, the nanoparticles prepared with the A6,11 peptide (**Figure 3.5d**), which modifies both anchor residues to remove binding at these sites, demonstrated the largest particles with average sizes between 2.8 and 3.1 nm. As listed in **Table 3.1** and seen in **Figure A2.4** of the Appendix II, trends in the particle size as a function of peptide sequence and Pd:peptide ratio can be generalized. First, it is noted that regardless of the Pd:peptide ratio employed to prepare the materials, particles of approximately the same size and distribution are generated when using the same peptide. Second, a general trend of increasing average particle size is observed as a function of the capping peptide sequence (Pd4 < A6 < A11 < A6,11). Interestingly, for all materials that are produced, regardless of the nanoparticle size, Pd:peptide ratio, and passivating sequence, single crystal nanoparticles are obtained, which can be difficult to achieve for Pd particles of < 5 nm. Here, regardless of the metal concentration, Pd surface binding is dictated by precise bio/inorganic recognition, which is likely programmed during phage display. As a result, at the lowest Pd: peptide ratio, excess peptide would remain in solution; however, at the higher ratios, more NPs would be produced,

exhausting the peptide supply. Eventually, the amount of peptide in solution would not be able to fully passivate the NPs, thus leading to the production of bulk materials. Indeed, at ratios ≥5, precipitation of Pd black was observed. As a control, K_2PdCl_4 was reduced in the absence of the Pd4 peptide, which allows for rapid nucleation and particle growth. Immediately after reduction, the Pd4 peptide was added to the reaction at a Pd:peptide ratio of 4 to stabilize the growing materials. In this event, Pd NPs are stabilized with an average size of 2.5 ± 0.5 nm, which is a significant increase in diameter compared to that obtained via the standard approach (1.8 ± 0.4 nm) in **Figure A2.5**. Larger sizes are achieved as the peptide was not in solution to arrest growth at the initial crystallization point, thus allowing the crystalline particles to continue growing. When the peptide is finally added, it rapidly binds the fcc Pd surface to cap growth, correlating well with the crystalline-based capping mechanism.

3.4.3 Molecular Dynamics (MD) Pd Nanoparticle Size

Molecular dynamics (MD) simulation with the CHARMMMETAL force field shows that Pd NPs require a critical size to form stable facets (**Figure 3.6**). Both a minimum size of the particles and stable facets appear critical for Pd4 binding. Small NPs of 1.0 nm consist of only 36 atoms and exhibit a dynamically changing, non-fcc structure that could be easily influenced by the peptide (**Figure 3.6a**).

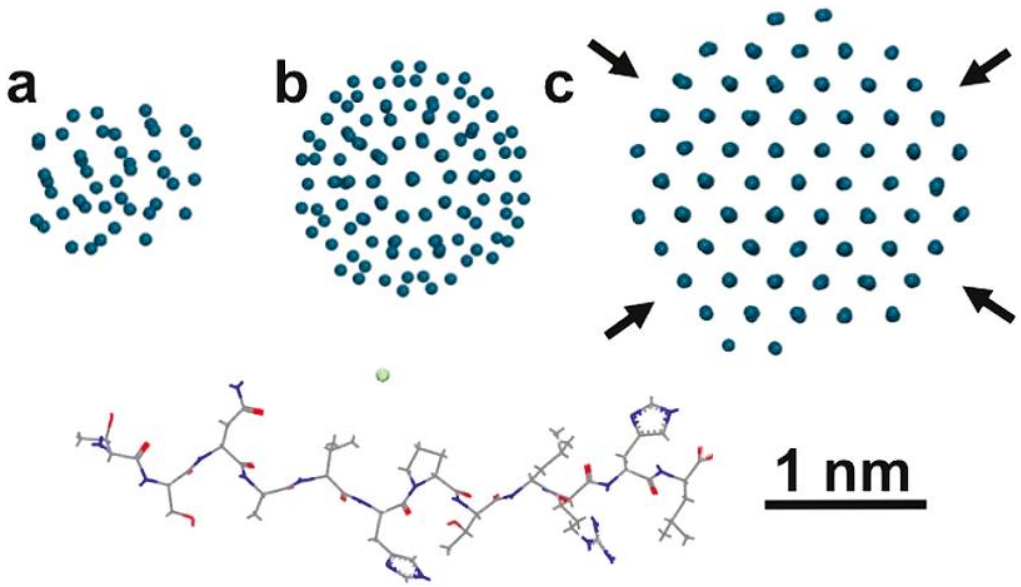

Figure 3.6. Molecular dynamics modeling of Pd nanoparticle composition at a) 1.0 nm, b) 1.5 nm, and c) 2.0 nm, such that fcc orientation is reached.

The particle is smaller than the peptide and cannot develop stable, soft epitaxial interactions. An increase in NP size to 1.5 nm increases the number of atoms to 120, increasing cohesion significantly within the particle as well as potential peptide attraction. A non-fcc structure close to spherical geometry was thermodynamically favored (**Figure 3.6b**) over an *fcc* structure of six atomic layers by 0.5 kcal/mol. The non-*fcc* structure was preferred upon annealing at 800 K and during a microsecond MD simulation at 298 K. The limited size and absence of defined *fcc* facets are not optimal for soft epitaxial binding and particle enclosure by the peptide. A further increase in particle size to 2 nm finally leads to a stable *fcc* particle that is bounded by (111) facets (**Figure 3.6c**). It contains 284 atoms, and a defect-free fcc structure is also preserved upon annealing (800 K) and cooling in the simulation. The peptide then coordinates with the locally planar (111) facets and stabilizes the particle through soft epitaxial interactions. Similarly, a larger NP of 3 nm diameter contains 960 atoms and is equally

bound by stable (111) facets for Pd4 binding. As the appropriate *fcc* orientation for Pd4 binding is displayed for 2 nm particles, peptide binding occurs at this size to arrest growth, which is fully consistent with the experimental results. At the same time, the mechanism of self-assembly of multiple peptides on the NP surface, possible surface reconstruction, and many other aspects still require detailed studies in the future.

3.4.4 CD Spectra and QCM Analysis of the Peptide-Based Materials To elucidate this unique structural trend, further spectroscopic analysis of the materials before and after reduction was conducted. CD spectra of the peptide library showed similar trends upon coordination of Pd^{2+} ions and nanoparticle formation. It should be noted that some scattering of light likely transpires at higher ratios, such that only approximate changes in ellipticity (helical character) can be suggested. Collectively, all the peptides became increasingly more unordered at higher Pd^{2+}:peptide ratios as shown by a loss in ellipticity due to Pd^{2+} coordination at multiple peptide binding sites present within the different peptides (**Figure 3.7**).

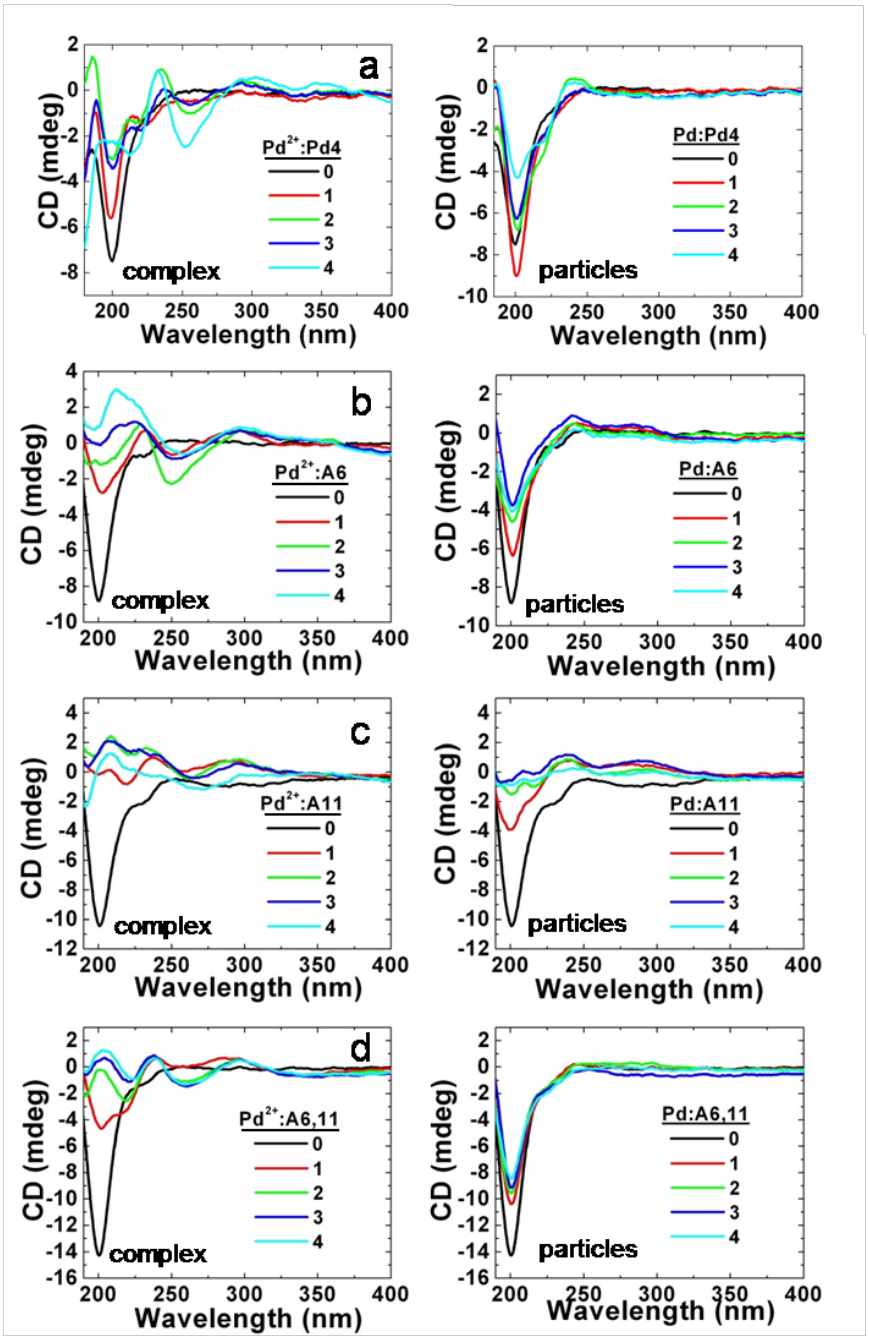

Figure 3.7. CD spectroscopy analysis of Pd2+ ions and reduced particles in the presence of a) Pd4, b) A6, c) A11, and d) A6,11 peptides, respectively.

In general, as the ratio of Pd^{2+}:peptide was increased, the negative CD band at 203 nm ($n \rightarrow \pi^*$) decreased in intensity and shifted to longer wavelengths, while a new CD peak was generated at ~250 nm for the uncomplexed Pd^{2+} salt. Alternatively, upon reduction

of Pd^{2+} ions to Pd^{0} nanoparticles, the corresponding peptides partially regained some secondary structure in order to accommodate nanoparticle binding, but moreover were independent of the Pd:peptide ratio (**Figure 3.7**). In total, deconvolution of the peptide CD spectra into individual secondary structure components using CDPro (Helix, 3_{10} helix, Strand, Turn, polyproline type II helix, and unordered) revealed that the free and NP-bound peptides were predominantly unordered (~45%) with low helical content (~6%). Notably, these structural features remained largely unchanged upon NP binding as depicted by a flat line when plotted against the different peptide:NP ratios. However, the amount of turn and strand motifs contributing to the overall peptide secondary structure were substantially affected by nanoparticle binding for the peptide set. By comparison, the Pd4 and A11 peptides exhibited the largest structural changes, while the A6,11 peptide remained mostly unaltered on the nanoparticle surface relative to its free conformation in solution. This suggests that the A6,11 peptide minimally interacts with the Pd nanoparticle through possibly only the N-terminus amine, thereby favoring the synthesis of larger sized particles as confirmed above. In contrast, the altered CD structure of Pd4 showed an increased percentage of turns and decreased number of strands in the presence of Pd metal. This suggests a strong peptide/nanoparticle interaction, which invariably affects the resulting nanoparticle size and is consistent with a peptide structure which is constrained at multiple peptide sites along the NP surface. Conversely, for the pair of peptides with single alanine substitutions (A6 and A11), we observed an increased % of strands and decreased number of turns after nanoparticle formation, although at lesser extents for A6. In the case of the nanoparticles capped with the A11 peptide, the number of turn structural motifs decreased from 24% (free) to 6%

(bound), while the strand content increased from 0% to ~32%. Similarly, the A6 peptide showed a 6% decrease in turn content and an increase of 21% for the strand component. In these cases, the peptides are less constrained along the NP and can adopt a strand motif extended from the surface. Full deconvolution of the free and bound peptides is visible in **Figure A2.6** (Additional Information II). This difference in stabilization is consistent with peptide adsorption measurements obtained QCM analysis, as shown in the Appendix II, **Figure A2.7** (Additional Information II). By QCM, the A6,11 peptide showed the lowest binding affinity to a Pd-coated crystal, while the A6 peptide had the largest affinity. Also, both the A11 and A6,11 showed more desorption from the surface and loss of mass as compared to Pd4 and A6, which remained tightly bound. These results confirm that the location of the alanine substitution is critical in defining the peptide structure on the nanoparticle surface and in modulating the catalytic activity (discussed below).

3.4.5 EXAFS Analysis of the Peptide-Based Materials

While identical NPs are prepared for each system, different catalytic TOF values were obtained. At the highest ratios, maximal activity is observed; however, the activity decreases for materials prepared at lower ratios. This suggests that, while the particles are identical in each sample, the overall reaction solution must be different to result in the varied TOFs. To probe the reaction mixture, Pd K-edge XAFS studies were conducted at beamline X18B at the National Synchrotron Light Source at Brookhaven National Laboratory. For this analysis, the Pd NPs prepared at the selected Pd:peptide ratios were synthesized and dried via lyophilization. The powders were then spread on adhesive tape, and their X-ray absorption coefficient was measured in transmission mode between 150

eV below and 1350 eV above the Pd K-edge (24 353 eV). As shown in **Figure 3.8a-b**, the X-ray Absorption Near Edge Structure (XANES) data demonstrate a strong similarity between all samples and a contrast with bulk Pd foil used as a control.

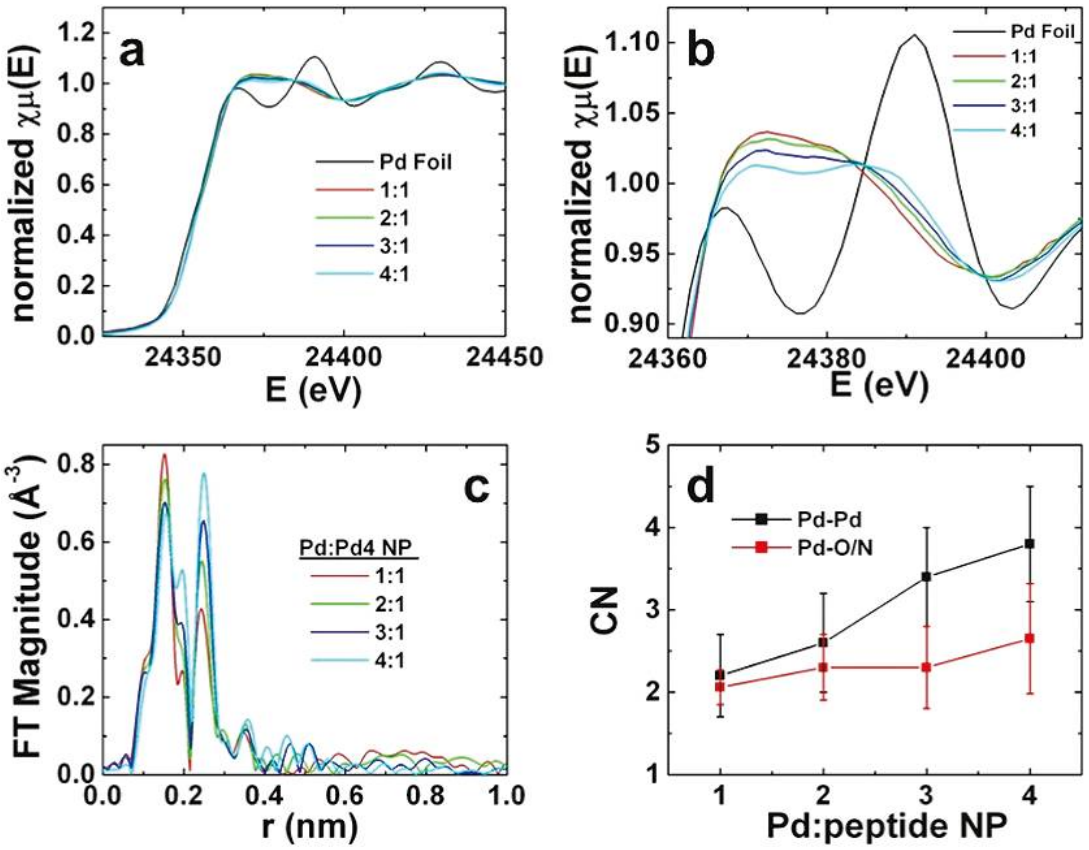

Figure 3.8. EXAFS analysis of Pd4-capped nanoparticles in incremental Pd:peptide ratios, including a) the edge step, b) an expanded view illustrating isosbestic points, c) Fourier transformed data for r-space neighbors, and d) CN value trends.

Figure 3.8b presents an expanded analysis at the near edge features, which demonstrates isosbestic points at 24384 and 24399 eV for the NP samples. This suggests that the reaction samples contain a mixture of two Pd components that vary proportionally to the ratio used during synthesis. After the background subtraction and edge-step normalization, the extended XAFS (EXAFS) data for the four samples were converted to k-space, k2-weighted, and Fourier transformed to r-space. The Fourier transform

magnitudes for the four NP samples are presented in **Figure 3.8c**, while data-fitting of the results for the NPs is presented in the Appendix II, **Figure A2.8**. From the r-space data, the peak at ~0.25 nm (uncorrected for phase shift) arises from Pd-Pd coordination within the NP sample, while the peak at ~0.15 nm represents the Pd-O/N coordination. Unfortunately, EXAFS is unable to distinguish between N and O scatterers due to their similar Z-values; thus, the data are reported as O/N. As is evident, a direct correlation between the intensity of these peaks and the Pd:peptide ratio used during synthesis is present. Here, as the ratio increases, the Pd-O/N peak decreases slightly, with an increase observed in the Pd-Pd peak. The first nearest-neighbor coordination numbers (CN) for Pd-Pd and Pd-O/N obtained from EXAFS analysis of the r-space data are presented in **Figure 3.8d**, which confirms the increase in Pd-Pd bonds with an increase in the Pd:peptide ratio. This suggests that the percent of Pd^{2+} ions reduced in the peptide/Pd^{2+} complex is highest for the sample prepared at a ratio of 4 and is lower for the NPs generated at a ratio of 1. This suggests that a mixture of unreduced complex and reduced NPs are present in the samples, which gives rise to the isosbestic points in the absorbance data. Interestingly, the Pd-O/N value remains roughly the same throughout the analysis within error bars.

To more fully characterize the materials, both the pre-reduced Pd^{2+}/peptide complexes and the zerovalent Pd4 and ala-analogue Pd nanoparticles were analyzed via XAFS spectroscopy. Experimental EXAFS spectra and best theoretical fits are shown in Appendix II, **Figure A2.8**. The nearest neighbor coordination numbers (CNs) were obtained for O/N, Cl, and Pd for the Pd4-based and ala-analogue materials, by EXAFS analysis in **Figure 3.9**.

For the three types of Pd neighbors: O/N, Cl, and Pd atoms in the sample, each were observed in the EXAFS analysis. Note that Cl was not previously observed, but the presence of the Cl neighbor in the precursor complex lead to its discovery in the final, zero-valent materials. It should be stated that these values are averaged over all Pd atoms in the sample that absorbed X-rays, thus such values are representative of the entire ensemble, not a specific nanoparticle or a complex. **Figures 3.9a** and **b** present the Pd-O/N and Pd-Cl first nearest neighbor CN values for the Pd^{2+}/peptide complexes prior to reduction. Since EXAFS is incapable of distinguishing between O and N scatterers due to their similar Z-numbers, these values are reported as O/N.

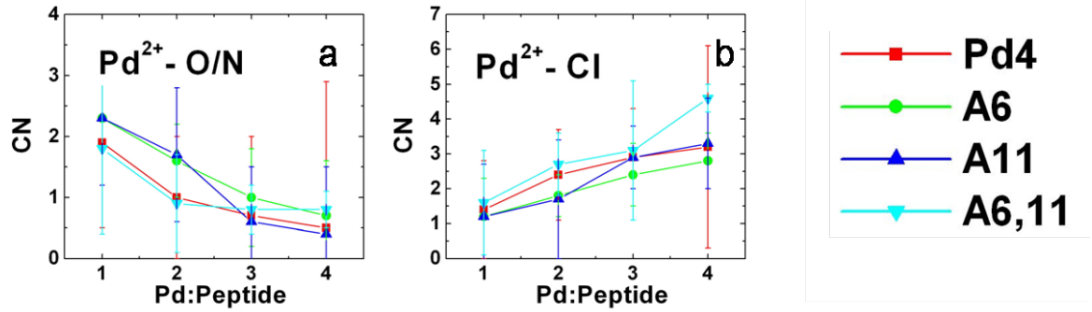

Figure 3.9. CN trends extracted from EXAFS analysis for the peptide-Pd^{2+} complexes of materials prepared at ratios 1 -4 of a) O/N and b) Cl coordination.

As shown in **Figure 3.9a** for the Pd-O/N CNs, it is clear that a trend of decreasing O/N coordination occurs as the Pd^{2+}:peptide ratio is increased from 1 to 4. Conversely, as shown in **Figure 3.9b**, the Pd-Cl CNs are shown to be directly proportional to the Pd^{2+}:peptide ratio such that they linearly increase over the ratios that are studied. This suggests that at low ratios, the Pd^{2+} ions possess more coordination with O/N from the peptide over Cl ions, while at higher ratios, more Cl coordination is present to the metal ions as compared to O/N. Furthermore, for each peptide at each ratio, the sum of the Pd-

O/N CN and Pd-Cl CN equals four, within the experimental uncertainties, which fits exactly with the number of ligands anticipated for the Pd^{2+} ions. Taken together, the data demonstrates increased peptide coordination for the Pd^{2+} ions at low ratios that decreases at higher ratios. At the higher ratios, increased Cl^- coordination to the Pd^{2+} ions is required to reach a four coordinate system. Furthermore, at the higher ratios, free Pd^{2+} species may be in solution, which would also account for the additional Pd-Cl coordination observed. This EXAFS data confirms the coordination of the peptide to the Pd^{2+} ions in solution to form the Pd^{2+}:peptide complex regardless of the peptide sequence, which plays a role in the reduction of the materials.

EXAFS analysis of the CN values for the peptide-capped zerovalent Pd nanoparticles is presented in **Figure 3.10a-c**. Specifically, **Figure 3.10a** presents the Pd-Pd nearest neighbor CNs for all four peptide-based systems. From the Pd-Pd CN, critically important information concerning the nanoparticle structure can be achieved in combination with TEM results. As shown previously,[137] for the Pd4-based materials, as the Pd:peptide ratio for the sample increases, a proportional increase in the Pd-Pd CN is observed (red plot). This trend can be attributed to either the increasing particle size[145] or the increasing degree of Pd^{2+} reduction in the sample, or both. Since the average particle size remains constant, as per TEM observations, the decreased CN values for the lower ratios can be explained solely on the degree of reduction that is lower in these systems. The degree of reduction is directly related to the coordination complex generated prior to reduction where more coordination to the peptide could shift the reduction potential, thus making the materials more difficult to reduce.[137] Indeed, EXAFS analysis of the pre-

reduced complex demonstrates increased peptide coordination to the Pd^{2+} metal ions, further supporting this hypothesis.

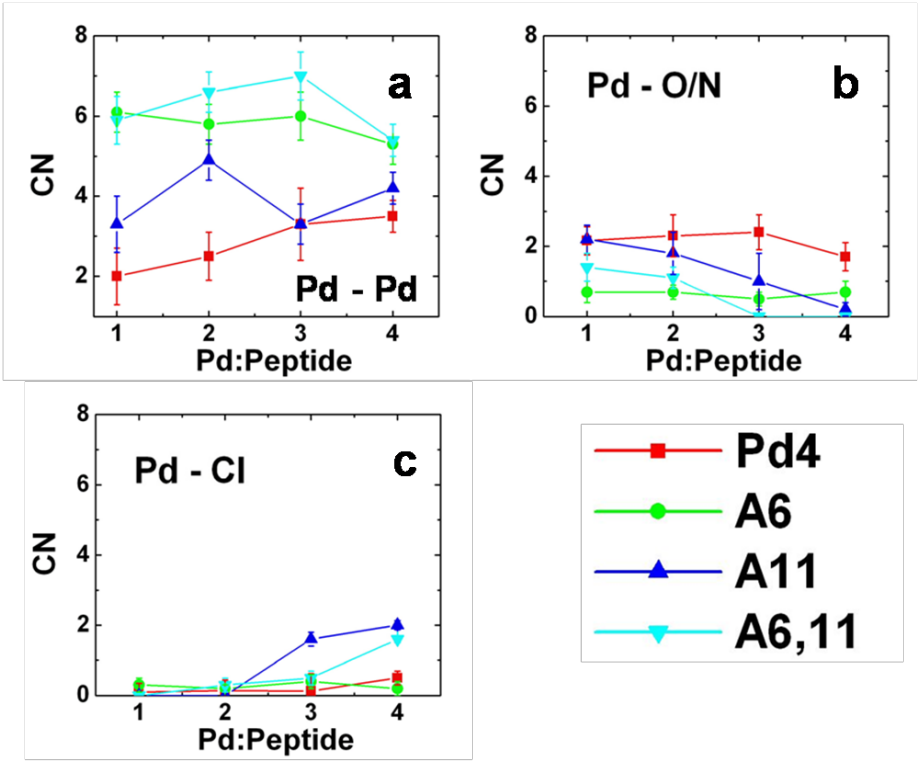

Figure 3.10. CN trends extracted from EXAFS analysis for the Pd^0 materials prepared at ratios 1 - 4 of a) Pd, b) O/N, and c) Cl coordination to Pd atoms.

Analysis of the CN values for the Pd nanoparticle prepared with the A6 peptides demonstrates a substantially different trend as a function of the Pd:peptide ratio as compared to the Pd4 system. Here, regardless of the ratio, nearly identical Pd-Pd CNs of ~6 are observed. This value is smaller than the theoretical value of 9.84 (assuming a perfect cuboctahedron) for particles of ~2.2 nm in diameter,[145] as observed by TEM. This suggests that partial reduction of the Pd^{2+} in the sample occurs, similar to the Pd4 sample; however, the coordination environment plays a less significant role in this process as equivalent degrees of reduction are present at all four Pd:peptide ratio samples. This equivalent degree of reduction is inferred from the identical particle size that is

observed for the sample by TEM. Furthermore, a higher degree of reduction for all samples is evident when using the A6 peptide as compared to the parent Pd4 sequence. Analysis of the Pd-Pd CN for the A11-based structure is presented in the royal blue plot of **Figure 3.10a**. Here, highly varied values are observed, which are likely due to the statistical noise of the EXAFS analysis. In this system, CNs of 3.3, 4.9, 3.3, and 4.2 are noted at Pd:peptide ratios of 1, 2, 3, and 4, respectively. Overall, these values are small, compared to the A6-capped particles, suggesting a lower degree of reduction. Finally, the Pd-Pd CN values for the A6,11-based materials are shown in the light blue data of **Figure 3.10a**. For these materials, high CNs of ~6 are noted that are similar to the A6-prepared nanoparticles at all of the Pd:peptide ratios studied. Note that these materials are ~1 nm in diameter larger than the A6-capped structures, thus a larger Pd-Pd CN value would be expected of A6,11 with more internal Pd atoms increasing the CN average.[145] This increase is observed over the value range of 5.4 - 6.8 for the Pd-Pd CN, though lower than a particle that size should ideally possess. This suggests that a slightly smaller fraction of Pd^{2+} is reduced in the A6,11 sample to result in the observed CN values as compared to the A6 materials. Taken together, this difference in the reduction for all of the different peptide-based samples evident in the Pd-Pd CN was surprising; however, the peptide secondary structure and binding of the Pd^{2+} ions may facilitate this capability. Analysis of the Pd-O/N and Pd-Cl CNs for the reduced nanoparticles with the four different peptide ligands is presented in **Figures 3.10b** and **c**, respectively. For the Pd4- and A6-capped materials, nearly equivalent Pd-O/N CN values for the two systems are observed across the selected Pd:peptide ratios used during materials synthesis; however, for the A11- and A6,11-prepared Pd nanoparticles, a linear decrease in O/N coordination

to Pd is noted as the ratio employed to fabricate the materials increases. Concurrent with this particle surface environment, the Cl coordination to the Pd materials is different as selected for by the peptide used to generate the particles. For instance, using the parent Pd4 and A6 sequences, minimal to no Cl is present within the first coordination sphere of the Pd nanoparticle on average in the samples. Interestingly, for the A11- and A6,11-capped particles, Cl coordination is evident for the materials generated at the higher Pd:peptide ratios. For both systems, no Cl is present when the materials are produced at Pd:peptide ratios of ≤ 2; however, the Pd-Cl CN linearly increases at the higher ratios to 2 and 1.6 for the A11 and A6,11-capped structures, respectively, at the maximum Pd:peptide ratio of 4. This suggests that for these materials, a degree of Cl coordination to the particle surface is present from Cl^- ions in solution in addition to the peptide that gives rise to the observed Pd-O/N coordination.

3.4.6 Catalytic TOF Analysis of the Peptide-Based Materials

Upon characterization of the peptide-capped Pd nanoparticles, their catalytic activity was studied for the Stille coupling of 4-iodobenzoic acid with $PhSnCl_3$ to prepare BPCA, which is illustrated in **Figure 3.11**.

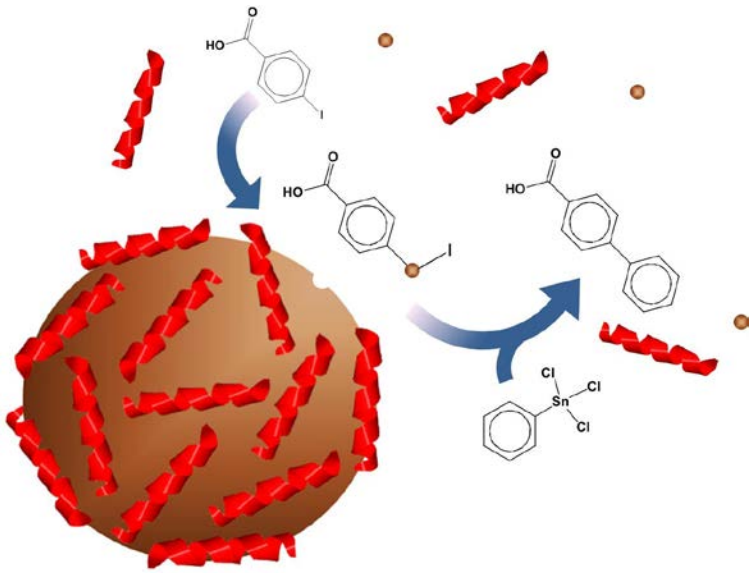

Figure 3.11. Catalytic scheme with peptide-capped Pd nanoparticles employed as the Pd source in the Stille coupling reaction.

Studies of the catalytic functionality are proving to be an important method to characterize the biological/inorganic surface of nanomaterials, as the reactivity is dependent upon the surface structure and composition. To characterize the reactivity of the materials, the TOF values for the individual reactions for all of the nanoparticles prepared were determined over the course of 1.00 h and are presented in **Figure 3.12**. A general decrease is observed in catalytic activity as the Pd:peptide ratio is decreased; however, the total Pd loading for each reaction remains constant at 0.050 mol% Pd.

The particles prepared with the Pd4 peptide at a Pd:peptide ratio of 4 demonstrated a TOF value of 2496 ± 252 mol BPCA (mol Pd ×hr)$^{-1}$.[137] At this same ratio, the A6-capped Pd particles showed an almost twofold increase in catalytic activity, with a TOF of 4314 ± 190 mol BPCA (mol Pd × hr)$^{-1}$.

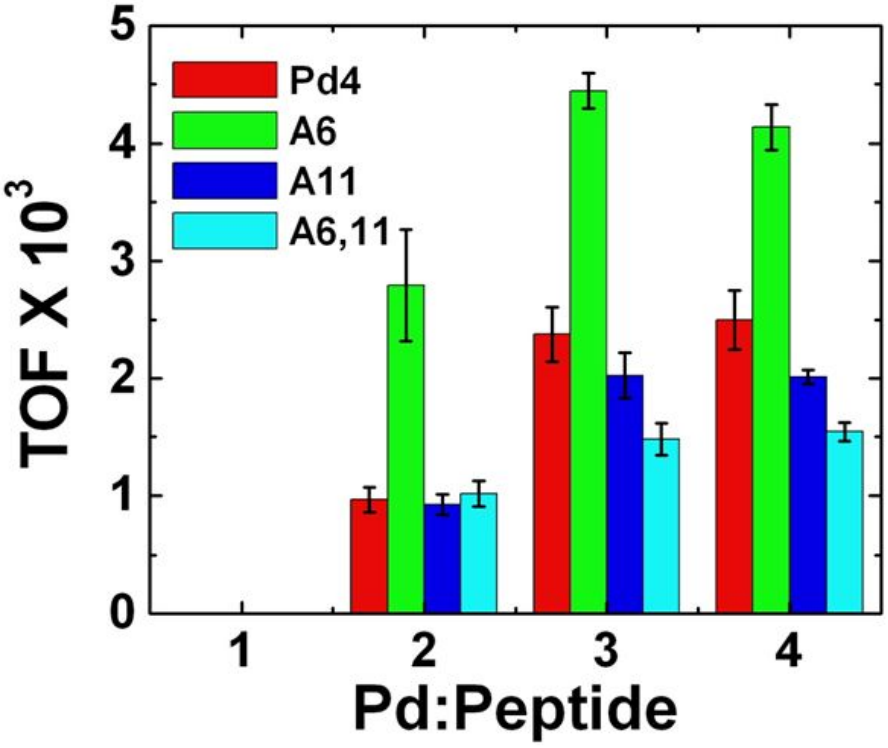

Figure 3.12. TOF analyses of Pd4 and alanine-analogue passivated Pd nanocatalysts in the Stille coupling reaction over Pd:peptide ratios 1 – 4. Catalytic loading of 0.050 mol % was maintained throughout.

The A11-based materials demonstrated catalytic activity that was diminished as compared to the Pd4-capped materials with a TOF value of 2010 ± 59 mol BPCA (mol Pd × hr)$^{-1}$, while the A6,11-prepared Pd nanoparticles had the lowest activity with a TOF of 1565 ± 66 mol BPCA (mol Pd × hr)$^{-1}$.

When using the materials prepared at a Pd:peptide ratio of 3, little deviation in the catalytic activity for these structures was noted as compared to the nanoparticles prepared at a ratio of 4; however, at subsequently lower ratios, diminished reactivity was observed. For the 2:1 ratio previously presented for the Pd4-based materials,[137] the particles showed a drop in reactivity with a TOF value of 965 ± 105 mol BPCA (mol Pd × hr)$^{-1}$ as compared to the materials prepared at higher ratios. This same loss in activity was

observed for the A6-prepared particles where a minimized TOF of 2793 ± 473 mol BPCA (mol Pd × hr)$^{-1}$ was observed. For the A11- and A6,11-capped materials, diminished TOF values of 1026 ± 191 mol BPCA (mol Pd × hr)$^{-1}$ and 1009 ± 78 mol BPCA (mol Pd × hr)$^{-1}$, respectively, were observed. Interestingly, at this ratio, even though minimized reactivity is evident for all of the materials, the A6-capped particles still remain significantly more catalytically active as compared to the particles generated with the other peptides. Finally, for the materials prepared at a Pd:peptide ratio of 1, no activity was observed for any of the particles over the time frame of the TOF study.

To test the effect of free peptide on the reactivity, the following control was studied. First, one batch of Pd nanoparticles was generated using the Pd4 sequence prepared at a Pd:peptide ratio of 4, which was then split into two equal volumes. To one of the Pd nanoparticle samples, sufficient excess Pd4 peptide was added such that the Pd:peptide ratio was decreased to 1, while in the second sample, no additional peptide was added, thus the Pd:peptide ratio remained at 4. Next, two Stille-coupling reactions were prepared that were catalytically driven by the nanoparticle samples that modulated the Pd:peptide ratio. As a result, the reaction catalyzed by particles with a Pd:peptide ratio of 4 proceeded as normal with a TOF value consistent with the observations of Figure 6b; however, the second reaction with excess peptide failed to produce a quantifiable amount of product in the 1.00 h TOF timeframe. This suggests that the excess peptide in solution does indeed alter the reactivity, which could arise from binding of leached Pd atoms generated during the catalytic cycle.

3.5 Summary

The catalytic results, in combination with the high-resolution characterization of the materials, afford the ability to infer unique structural information concerning the biotic/abiotic interface of the peptide-capped Pd nanomaterials. First, from the UV-vis and TEM evidence, it is clear that the peptides are able to cap the Pd structures where particles of the same size are generated using the same peptide, regardless of the Pd:peptide ratio employed during materials synthesis. Furthermore, by slight modifications to the sequence, changes in the particle size are possible over the very small size range of 1.8 – 3.0 nm in diameter. The changes to the peptide sequence are likely to alter the biological recognition of the peptide for the particle surface, which thereby alters the peptide binding affinity values to change the particle size. We have previously established using the Pd4 sequence that the peptide is able to recognize and bind the face centered cubic (*fcc*) structure of Pd,[137] which is likely embedded during the phage display process. By altering the specific binding motif, which has been previously suggested to arise from the two histidine residues,[80] this likely alters the recognition element of the sequence to result in the larger particle sizes. Furthermore, CD and QCM data directly show that stronger binding sequences present more significantly altered secondary structures when bound to the particle surface as compared to free in solution, further suggesting that modifications to the sequences alters the recognition ability and binding strength of the peptides for Pd. This would give rise to the larger structures and different selected sizes for the A6-, A11-, and A6,11-capped Pd nanoparticles. The results also suggest that binding of the histidine at the 11 position is required for increased specificity and binding strength due to the smaller particles prepared using the

native Pd4 and A6 sequences as compared to the A11 and A6,11 peptides that remove binding at this site.

The argument concerning the importance of binding at the 11 position in the peptide sequence is further strengthened in light of the catalytic results. When comparing the TOF values for the materials prepared at the same Pd:peptide ratio, it is evident that reactivity of the peptide-capped particles is altered as a function of the peptide on the surface following the trend of A6 > Pd4 > A11 > A6,11. For those peptides that modified binding at the 11 position, significantly reduced activity is noted. Additionally, based upon the EXAFS analysis of the reduced particles, the A11- and A6,11-capped structures prepared at ratios of 3 and 4 possess a substantial amount of Cl^- coordination at the nanoparticle surface, which likely affects the functionality by inhibiting reactivity at these sites, leading to the decreased TOF values. For this reaction, the materials follow a Pd atom leaching process,[83] consistent with other C-C coupling schemes;[8] therefore, the changes in particle size observed here are not anticipated to alter the reactivity.[130] As a result, the variations in reactivity can be directly attributed to the particle surface structure that is controlled by the peptides. Furthermore, while particles of nearly identical size and structure are prepared at all of the ratios for the different peptide sequences, the catalytic activity of the materials decreases for those particles prepared at lower ratios. For the Pd4-based materials, this has been rationalized to be a function of the degree of reduction where decreased reduction at the lower ratio materials leads to diminished reactivity.[137] For the A6-, A11-, and A6,11-capped particles, similar degrees of reduction are observed across the different particles prepared, thus the same amount of reduced Pd metal in each reaction is roughly equivalent. This indicates that additional

effects are likely to contribute to the lowering of reactivity for particles prepared at the lower ratios. To that end, the main difference between the different sets of materials is the amount of free peptide in the reactions at the lower ratios. In the higher ratios (3 and 4), all of the peptide is anticipated to be coordinated to the Pd particle surface to ensure colloidal stability. When insufficient peptide is present, Pd black precipitation is anticipated, which occurs for materials at ratios > 4, thus suggesting complete particle capping of the peptides at lower ratios. At the lowest ratios (1 and 2), excess peptide is present in the reaction to cap the particle surface, thus metal-free sequences are present in solution that are transferred to the reaction. Due to the theorized Pd leaching process of nanoparticle-driven Stille coupling,[83] seen in **Figure 3.13**, free Pd atoms are released once the BPCA product is generated.

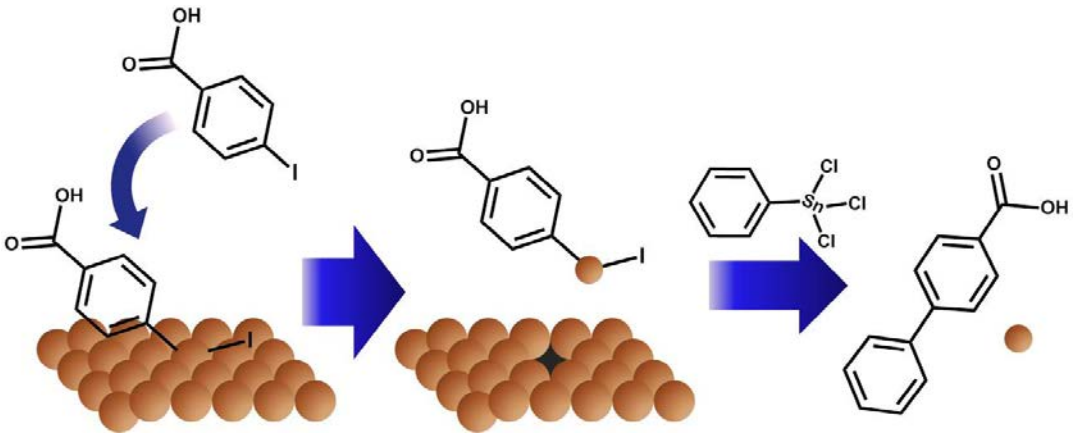

Figure 3.13. The proposed atom-leaching mechanism in the Stille coupling reaction with 4-iodobenzoic acid starting material.

In this sense, the excess peptide could then strongly bind these free Pd atoms, thus sequestering them from solution to lead to the observed lower TOF values. This expansion on previous work illustrates multiple effects otherwise overlooked with respect to concentrations of nanoparticle material:passivant relationships. Following this

approach, more free peptide in solution would lead to diminished reactivity, which is indeed observed as the reactions are processed using the materials generated at lower Pd:peptide ratios. Taken together, this suggests that three effects, the biotic/abiotic surface structure, the degree of Pd reduction, and the amount of free peptide in solution, contribute to the observed reactivity.

These results directly relate to the sequences determined via phage display. While the Pd4 peptide was isolated with affinity for Pd, additional sequences were designed that possessed similar affinity. By changing the peptide sequence, the degree of affinity can be modulated to control particle size and functionality. In some instances, this can decrease the activity; however, selected modifications can be used to substantially increase the functionality, which is highly desirable. This suggests that while phage display can be used to isolate sequences that bind a target substrate, the technique may not elucidate the optimal sequence to control both material structure *and* activity. These two considerations are likely a function of the binding strength, surface peptide structure, and inorganic composition, which could be tuned by the peptide sequence. The peptides isolated via phage display are likely to be optimized for the strongest binding sequences; however, many applications, including catalysis, are enhanced by ligands that are more loosely bound to allow substrate interactions with the metallic surface. Furthermore, only a limited subset of the total number of dodecamer peptides possible is present in the phage library, thus limiting the number sequences that could be determined. Taken together, these results suggest that while phage display is an excellent technique to isolate peptides with specific affinity, the sequences that are determined may not be optimal for the final material application. By employing selective peptide modifications, new

sequences can be rationally designed to control the structure, properties, and function of the final materials.

3.6 Conclusions

In conclusion, it is evident that single residue changes to peptide sequences can control the size and functionality of nanoparticles by modulating the peptide surface binding and structural interface. By these simple substitutions, particle sizes can be tuned that vary over a just a 2 – 3 nm size range, producing nearly monodisperse, single-crystalline materials. This size selectivity is likely a function of the peptide binding motif to its target substrate, which results in changes to the interfacial profile of the peptide-capped materials and possess control over their functionality. Combined, these results suggest that peptides may act as specialized ligands, allowing for nanoparticle fabrication with precise control over the size, shape, crystallinity, and functionality of nanomaterials. Further modifications not available to phage display are needed to confirm these capabilities, which are found in the following text.

Chapter 4. Cysteine Substitution Effects to Enhance the Catalytic Reactivity of Peptide-Capped Nanoparticles

4.1 Overview of Study

Peptide-based methods represent new approaches to selectively produce nanostructures with potentially important functionality. Unfortunately, bioselection methods can only select peptides with compositional affinity and not for the properties of the final material. In this work, evidence is presented to demonstrate that materials-directing peptides can be rationally modified to significantly enhance particle functionality without altering the structural morphology. To this end, modification of selected residues to vary the site-specific binding strength and biological recognition can be employed to increase the catalytic efficiency of peptide-capped Pd nanoparticles. These results represent a step toward the *de novo* design of materials-directing peptides that can control nanoparticle structure/function relationships.

4.2 Introductory Remarks

Biology provides exquisite inspiration for the production of functional inorganic nanomaterials.[22,102,148] Most of these materials are prepared using peptides and proteins to direct structural growth and engender the system with desired properties.[27,36,149] Mimicking these approaches for the generation of technologically useful nanomaterials represents an avenue to achieve important structures for sustainable activities.[8,26,40] Many groups have turned to biocombinatorial approaches to isolate peptides with affinity for a range of non-biological materials;[37,48] however, the effect of the biotic/abiotic interface over the structure/function relationship remains poorly understood. To this end, the

ability to fine-tune desirable material properties could be achieved at the peptide sequence level.[25,27,138,149]

Previously, the Pd-specific Pd4 peptide (TSNAVHPTLRHL) was employed for the fabrication of peptide-capped Pd nanoparticles with the ability to catalyze C-C coupling reactions under non-traditional conditions of a water-based solvent at room temperature.[26] The peptide is anticipated to anchor to the metallic surface through the histidine residues at the six and eleven positions,[80] where substitutions at these sites results in changes to the particle size and catalytic activity.[138] In this regard, it is likely that weaker binding at the six position and stronger binding at the eleven position could result in peptides that produce nanoparticles with optimized catalytic functionality.[138]

In this work, rational design is employed to generate new peptide sequences to enhance the structure/function relationship of inorganic nanoparticles for catalytic functionality; however, such approaches could be adapted for nanomaterials with other functionalities. To this end, the Pd4 peptide was employed as the parent sequence wherein the six and eleven positions were varied over three residues: cysteine, histidine, and alanine. These amino acids were selected to modulate the binding strength at these specific positions with cysteine being the strongest binder, alanine the weakest, and the native histidine being of intermediate binding strength.[37] From this, six different peptides were generated, listed in **Table 4.1**, which were used to prepare the peptide-capped Pd nanoparticles. Complete characterization of the peptide binding effects were studied, followed by their catalytic analysis using Stille C-C coupling, which demonstrated reactivities that varied based upon the binding strength of the residues at the pre-determined positions. Interestingly, no correlation between the peptide binding strength

and catalytic functionality was noted, suggesting that localized binding effects within the sequence dominate property control. Taken together, these results are important as they demonstrate that rational design principles can be employed to generate peptide sequences with the ability to optimize material properties and/or functionalities that cannot be selected for through biocombinatorial approaches.

Based upon the predicted metal surface binding at the six and eleven positions of the Pd4 peptide,[80] a set of six different sequences was prepared (**Table 4.1**).

Peptide	Sequence	Size	TOF[a]
Pd4	TSNAVHPTLRHL	2.0 ± 0.4 nm	2234 ± 99
C6	TSNAVCPTLRHL	2.2 ± 0.3 nm	3963 ± 28
C11	TSNAVHPTLRCL	2.4 ± 0.4 nm	6138 ± 55
C6,11	TSNAVCPTLRCL	2.3 ± 0.4 nm	3974 ± 280
A6C11	TNSAVAPTLRCL	2.4 ± 0.4 nm	6097 ± 65
C6A11	TSNAVCPTLRAL	2.4 ± 0.4 nm	4147 ± 340

a = mol product (mol Pd × h)$^{-1}$

Table 4.1. Table of Pd4 and cys-analogue peptides, with their corresponding sequence, size analysis and TOF analysis.

As illustrated in **Figure 4.1**, the binding events of the peptide at the six and eleven positions are likely to control the structure/function relationship of the finally prepared materials. To determine such effects, a set of six different sequences was prepared (**Table 4.1**). The native peptide, Pd4, possesses histidine residues at these locations. Two single cysteine modified peptides, C6 and C11, were prepared that changed the histidine residue

to a cysteine at the six and eleven positions, respectively, while a double modification peptide, C6,11, was also generated that simultaneously modified both histidines to cysteines. Note that phage display is biased against cysteine, thus such residues are typically not observed in isolated sequences.[150] Two additional peptides were also designed that included both cysteine and alanine modifications: the A6C11 that incorporated an alanine at the six position and a cysteine at the eleven position and the C6A11 peptide with a cysteine and alanine modification at the six and eleven positions, respectively. These two sequences were generated to substantially change the binding strength at the two selected positions, where minimal to no binding at the alanine sites was anticipated, with the strongest binding from the cysteine residues. While these results all support the necessity of peptides for tuning the size, activity, and functionality of Pd nanoparticles, the sequence-specific interfacial binding interactions are still not fully understood. Surface affinity can be obtained and potentially increased for a specific material by the use of rationally designed ligands; however, these passivants must possess a balance of passivation and still be permissive of surface activity. These requirements are well-met by short peptides, due to their ease of synthesis, wide range of interactive side chains, sequence variability, and structural motifs.

These properties are characterized through a variety of methodologies, including TEM analysis of the respective materials, CD spectroscopy of the peptide secondary structure of materials, UV-vis monitoring of the complex and nanoparticle formation, QCM analysis of k_a, k_d, and Keq values for a Pd surface, and TOF analysis via the Stille coupling reaction. Taken together, these results are important as they demonstrate that rational design principles can be employed to generate peptide sequences with the ability

to optimize material properties and/or functionalities that cannot be selected for through biocombinatorial approaches.

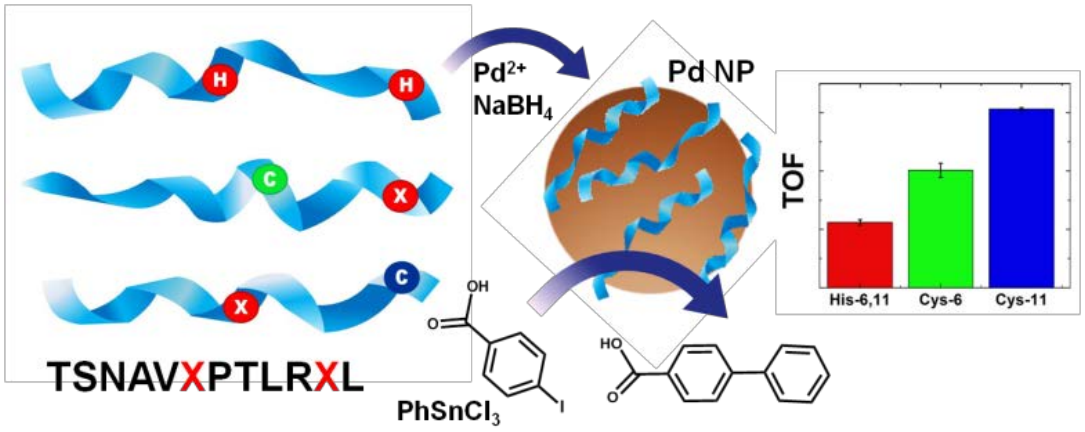

Figure 4.1. Cys and Ala substitutions of the Pd4 peptide and their respective binding and catalytic activities of their resulting nanomaterials.

The continued development of these properties leads to the ability to fine-tune nanomaterial activity through peptide sequence engineering for a target substrate, such that a desired size, shape, activity, and function is capable through rational sequence design.

4.3 Methods

4.3.1 Chemicals

Wang resins, substituted with an FMOC protected leucine residue, FMOC-protected amino acids, piperidine, diisopropyl ethylamine (DIPEA), O-benzotriazole-N,N,N',N'-tetramethyl-uronium-hexafluoro-phosphate (HBTU) and N-hydroxybenzotriazole (HoBT) were purchased from Advanced Chemtech (Louisville, KY). K_2PdCl_4 and triisopropylsilane were purchased from Sigma-Aldrich (Milwaukee, WI), while NaBH4 was acquired from EMD Chemicals (Gibbstown, NJ). Phenyltin trichloride (PhSnCl3),

$CDCl_3$, trifluoroacetic acid (TFA), anhydrous Na_2SO_4, NaCl, and KOH were purchased from Fisher (Pittsburgh, PA), while 4-iodobenzoic acid was acquired from TCI America (Wellesley Hills, MA). N,N-dimethylformamide (DMF), acetonitrile, diethyl ether and methanol were purchased from Pharmco-AAper (Shephardsville, KY). All chemicals were used as received. Milli-Q water (18 mΩ•cm; Millipore, Bedford, MA) was used throughout for all experiments.

4.3.2 Nanoparticle Synthesis

Peptides were synthesized with standard FMOC protocols, HPLC purification, and MALDI confirmation were conducted using standard methods. One set of nanoparticles were prepared for each respective peptide, with the corresponding sequences discussed previously (**Table 4.1**). Here, the synthesis of nanoparticles maintains an approximate 3.3:1 metal-ligand ratio, slightly dependent on varying molecular weight of each peptide. A 10 mg/mL concentration peptide stock solution was prepared in water. To 4.775 mL of water, 100 µL of the peptide stock was added, where the final peptide reaction concentration was 150µM. To this solution, 25.0 µL of a freshly prepared 100 mM K_2PdCl_4 solution was added, the solution turned a bright yellow, and the mixture was allowed to stand for 30.0 min after initial stirring to allow for Pd^{2+}/peptide complexation. To the complex solution, 100 µL of a freshly prepared 100 mM $NaBH_4$ solution was added to reduce the Pd^{2+} ions in solution, which resulted in an immediate solution color change from yellow to brown. The reaction was allowed to stand for 1.00 h to ensure complete metal reduction.

4.3.3 Catalytic Analysis

For the catalytic analysis, Stille C-C coupling was employed. For this, 1.25 mmol of 4-iodobenzoic acid and 1.56 mmol of $PhSnCl_3$ were co-dissolved in sufficient 2.25 M KOH. Subsequently, 1.25 mL of the stock Pd nanoparticles was added to the reaction, resulting in a 0.05 mol% Pd concentration and a final volume of 20.0 mL. 2.0 mL aliquots were then extracted and quenched with 12.5 mL of 5.0% HCl at selected time points up to 1.00 h. The reaction product was then extracted and quantitated using described methods.

4.3.4 Stille Coupling

As a model for probing the activity of Pd nanoparticles, the Stille coupling reaction was used as a catalytic system, in which the peptide-capped particles could be used. Nanoparticle solutions were added in 0.05 Pd mol % (1.25 mL) to 2.25 M KOH with 1.25 mmoles 4-iodobenzoic acid and 1.56 mmoles phenyltin trichloride in a 20.0 mL total solution volume. Samples were taken in 2.0 mL volume aliquots and quenched with 12.5 mL 5.0 % HCl every 5.0 minutes for the first 30.0 min, and every 10 minutes afterward for a total of 60.0 min. The resulting aliquots were extracted with three 30.0 mL washes of diethyl ether and two 20.0 mL washes of saturated salt water. The remaining organic layer was dried and co-dissolved with 75.0 mg t-butylphenol as an internal standard in deuterated chloroform and analyzed *via* ^{1}HNMR. These coupling reactions were performed in triplicate and the TOF values obtained from the slope fit of the initial rate of increase in bisphenyl carboxylic acid (BPCA) moles.

4.3.5 Characterization

UV-vis analysis of the materials was conducted using an Agilent 8453 photodiode array UV-vis spectrometer employing a 0.2 cm path length quartz cuvette. Peptide-Pd^{2+} complex samples in water were analyzed using a peptide solution at the reaction concentration as the blank. UV-vis analysis of the resulting nanoparticles after reduction of these samples was completed using identical methods. The resulting spectra are in the Appendix-III. A 5.00 μL sample of each nanoparticle solution was deposited and allowed to dry on a 400-mesh Cu grid coated with ultrathin carbon. TEM images were obtained of the synthesized NP samples with a JEOL 2010F TEM operating at 200 kV. The analysis of at least 100 nanoparticles among multiple images was employed to determine particle size distributions and ensure consistency. For QCM-D measurement chips, Pd surfaces were prepared by sputter-coating Pd onto Au QCM sensors for 180 s with a Cressington 108-Auto sputter coater. The metallic surfaces were then cleaned by UV/ozone exposure for 10.0 min, followed by a deionized water rinse and another 10.0 min UV/ozone exposure. Each peptide was dissolved in Synergy UV-ultrapure water at concentrations of 2.5, 5.0, 7.5, 10.0, and 15.0 μg/mL. QCM measurements were obtained with a Q-Sense E4 QCM-D system, in which standard flow modules were employed. A flow rate of 0.15 mL/min was used for each analysis. The third overtone frequency was fit with a Langmuir isotherm for all QCM measurements from which the binding constants can be determined via known methods. CD spectra were obtained on a Jasco J-815 CD spectrometer using a 750 μL quartz cuvette with a pathlength of 0.5 cm. Peptides were dissolved in double-deionized water and a concentration of 16 μM was used for all CD measurements. Nanoparticles were prepared at equivalent ratios and likewise diluted for

CD. The CDPro software package was used for analysis of CD spectra to deconvolute secondary structure contributions.

4.4 Results and Discussion

4.4.1 QCM Analysis of Pd4 and Cys-Analogues

As previously employed, the Langmuir model was derived to be applicable to a multiple-concentration system, such that the k_a and k_d are both unknown, as previously described. Quartz crystal microbalance (QCM) analysis was initially employed to determine changes in the Pd affinity of the peptides based upon the sequence changes. **Figure 4.2a** presents the observed frequency changes for the C6A11 peptide binding to a Pd sensor at five selected concentrations. As anticipated, for all peptide concentrations as time increases, the change in frequency decreases until saturation, consistent with binding of the target surface. Note that an inverted plot is presented to enhance the clarity of data presentation. From this, a series of five k_{obs} values were determined employing previously described methods,[61] which were then plotted against the peptide concentration (**Figure 4.2b**). Linear fitting of the data was then used to determine the association (k_a) and dissociation (k_d) constants of peptide binding from the slope and y-intercept values of the best-fit line, respectively. Similar studies were conducted for all of the peptides of **Table 4.1** (Appendix III, **Figure A3.1**), where the binding constants for all sequences are listed in **Figure 4.2c**. From this analysis, the parent Pd4 peptide was observed to possess a k_a of 1693 ± 169 $M^{-1}s^{-1}$ and a k_d of 0.0028 ± 0.0006 s^{-1}, which

results in a K_{eq} value of 6.05 × 10^5 ± 1.33 × 10^5 M^{-1} and a ΔG value of -33.0 ± 0.5 kJ/mol.

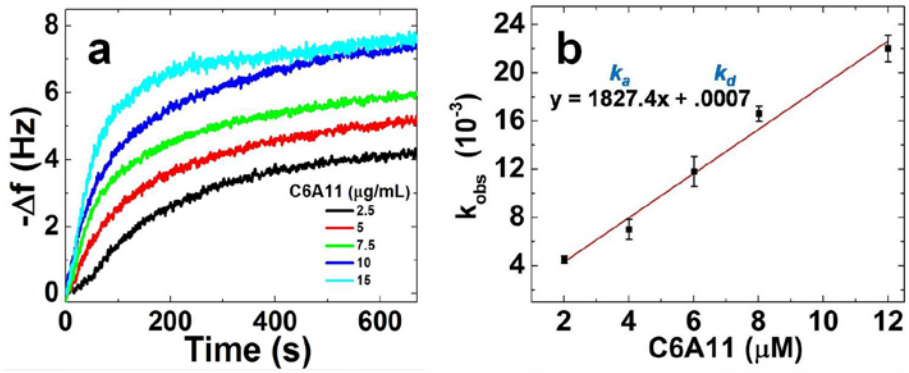

c

Molecule	k_a ($M^{-1}s^{-1}$)	k_d × 10^{-3} (s^{-1})	K_{eq} × 10^5 (M^{-1})	ΔG (kJ/mol)
Pd4	1693 ± 76	2.8 ± 0.6	6.1 ± 1.2	-33.0 ± 0.5
C6	1991 ± 117	1.0 ± 0.4	19.9 ± 7.3	-35.9 ± 0.9
C11	1474 ± 132	1.0 ± 0.5	14.7 ± 7.4	-35.1 ± 1.2
C6,11	1722 ± 72	1.0 ± 0.5	17.2 ± 8.5	-35.5 ± 1.2
A6C11	1563 ± 210	2.8 ± 0.9	5.6 ± 1.9	-32.7 ± 0.8
C6A11	1827 ± 113	0.7 ± 0.4	26.1 ± 14.2	-36.5 ± 1.3

Figure 4.2. QCM analysis of peptide binding: (a) observed frequency changes based upon peptide binding as a function of C6A11 concentration, (b) plot of the calculated k_{obs} values as a function of C6A11 concentration, and (c) Pd adsorption analysis for the parent Pd4 peptide and cysteine analogues.

Interestingly, when cysteine-only modifications were employed (C6, C11, and C6,11), while slightly lower k_a values were noted as compared to the Pd4, substantially diminished k_d values were also observed. As a result, significantly increased K_{eq} values of 1.99 × 10^6 ± 7.28 ×10^5 M^{-1}, 1.47 × 10^6 ± 7.39 ×10^5 M^{-1}, and 1.72 × 10^6 ± 8.52 ×10^5 M^{-1} were determined for the C6, C11, and C6,11 peptides, respectively. This in turn leads to greater ΔG values of -35.9 ± 0.9 kJ/mol for the C6, -35.1 ± 1.2 kJ/mol for the C11, and -35.5 ± 1.2 kJ/mol for the C6,11 peptides, indicating a greater affinity for the Pd surface.

When both alanine and cysteine-based peptide modifications are employed, unique changes in the Pd binding constants were observed. For instance, analysis of the A6C11 peptide demonstrated k_a and k_d values of 1563 ± 210 $M^{-1}s^{-1}$ and 0.0028 ± 0.0009 s^{-1}, respectively, thus resulting in a K_{eq} of 5.58 × 10^5 ± 1.86 ×10^5 $M^{-1}$and a ΔG of -32.7 ± 0.8 kJ/mol. Such values are quite similar to those observed for the parent Pd4 peptide, suggesting that the increased binding effect of the cysteine residue may be offset by the weakened binding of the alanine. Analysis of the C6A11, however, demonstrated binding constants of 1827 ± 113 $M^{-1}s^{-1}$, 0.0007 ± 0.0004 s^{-1}, 2.61 × 10^6 ± 1.42 ×10^6 M^{-1}, and -36.5 ± 1.3 kJ/mol for the k_a, k_d, K_{eq}, and ΔG values, respectively. From this analysis, the strongest binding was observed from the C6A11 peptide, within the error of the analysis, while the weakest binding was observed from the A6C11. Such results were somewhat surprising as alanine modifications to the peptide were anticipated to diminish the binding strength regardless of the position; however, changes to the peptide conformation based upon the sequence substitution may occur to increase the affinity. To this end, altered biotic/abiotic interfaces are likely, which were probed via CD analysis of the peptides before and after nanoparticle surface binding (discussed below).

4.4.2 UV-vis and TEM Analysis

Upon confirmation of the Pd affinity, the peptides were employed as passivating ligands to fabricate Pd nanoparticles using standard approaches.[26] The materials were then analyzed *via* UV-vis spectroscopy and transmission electron microscopy (TEM). UV-vis analysis of each peptide solution indicated a relatively featureless spectrum as anticipated (Appendix III, **Figure A3.2**). Upon addition of K_2PdCl_4, the spectra of the Pd^{2+}

complexed peptides demonstrated the appearance of a ligand-to-metal charge transfer (LMCT) band at ~215 nm.[138] After addition of $NaBH_4$, the reduced materials displayed a broad absorbance that increased towards lower wavelengths and the lack of an LMCT peak, all of which suggests nanoparticle formation. TEM imaging of the materials capped with the designed peptides is presented in **Figure 4.3**.

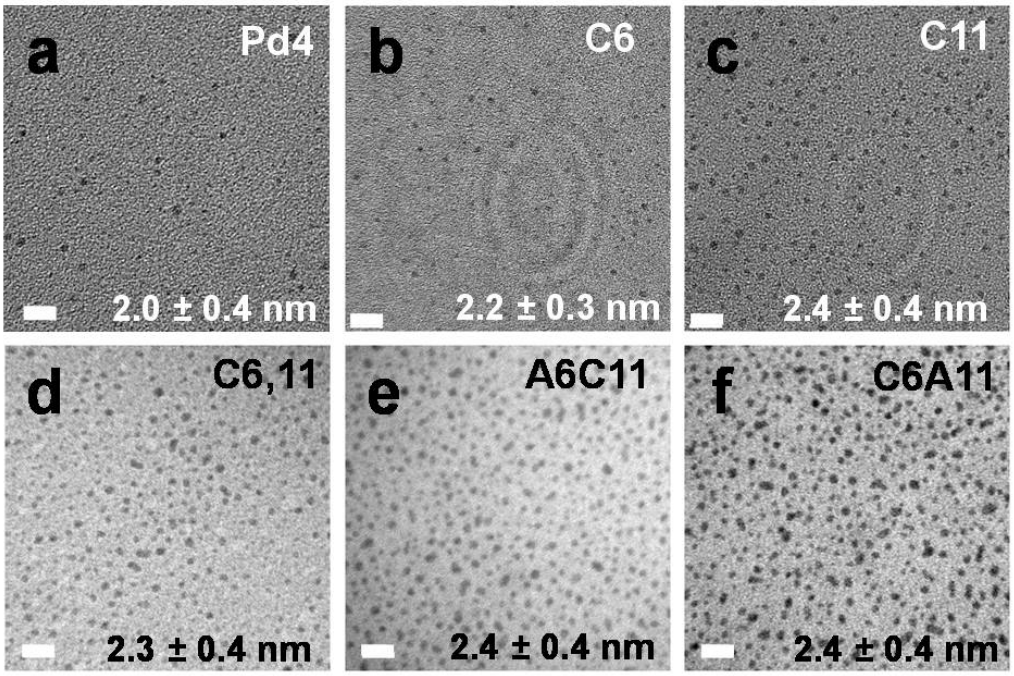

Figure 4.3. TEM analysis of the Pd nanoparticles capped with the (a) Pd4, (b) C6, (c) C11, (d) C6,11, (e) A6C11, and (f) C6A11 peptides. All scale bars are 10.0 nm.

For the Pd4-capped particles, an average size of 2.0 ± 0.4 nm was noted, consistent with previous studies;[26,138] however, for the particles prepared with the cysteine-substituted peptides, a slight size increase to 2.2 ± 0.3 nm (C6) and 2.4 ± 0.4 nm (C11), and 2.3 ± 0.4 nm (C6,11) was observed. Furthermore, for the materials capped with either the A6C11 or C6A11 peptide, particles of an identical size of 2.4 ± 0.4 nm were noted. Such similar sizes for the particles prepared with the A6C11 and C6A11 peptides were surprising as

they have different binding affinities, based upon their ΔG values; however, such results may be related to the biological recognition of the particle surface rather than their individual metallic affinity.[137] This suggests that the resultant particle size is based upon factors such as peptide binding motifs and surface recognition elements, rather than on the absolute degree of affinity for the target material. It is also interesting to note that particles of nearly the same size were generated with the designed sequences (2.2 – 2.4 nm). Such results are different than previous work with alanine substituted peptides that displayed controllable changes in particle size based upon sequence modifications.[138] This indicates that the presence of cysteine residues may modify the bio-recognition capabilities of the peptides through metal-sulfur interactions; however, the overall structure of the different bound peptides is anticipated to vary based upon the altered sequences and the binding of the other residues to the particle surface.

4.4.3 CD Analysis of the Unbound and Bound Peptides

Structurally, CD spectroscopy showed significant changes in peptide conformation after Pd binding that is strictly dependent on the location of cysteine within the sequence. The largest change in peptide surface structure was observed with the C6,A11 peptide after Pd binding. For this peptide, CD (Figure 3) showed the presence of two new peaks at ~215 nm (negative peak) and ~240 nm (slightly positive peak) when bound to the Pd nanoparticles and a wavelength shift from 201 nm to 205 nm for the dominant negative CD peak (random coil). Collectively, these features are indicative of a change in peptide structure upon binding to the Pd surface, which exhibits partial characteristics of a polyproline type II (PP2) helix (~18% contribution).

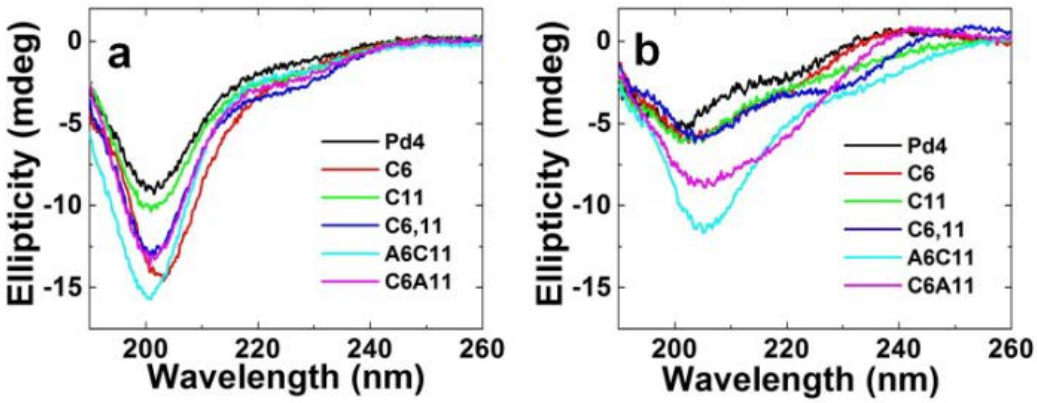

Figure 4.4. CD analysis of the selected peptides (a) before and (b) after binding to the Pd nanoparticle surface. Deconvolution of the CD spectra is visible in **Figure A3.3** (Additional Information III).

The Pd-bound C6 peptide possessed similar features to C6,A11, although they appear to be less structured and more unfolded based on differences in ellipticity. For the set of peptides with cysteine only in the 11 position, the CD spectra of the Pd-bound C11 and A6,C11 peptides exhibit striking similarities in terms of peak shapes and wavelengths, where both represent unordered structures on Pd. Again, the Pd-bound C11 peptide has a decreased ellipticity relative to A6,C11 on Pd and is more unfolded. Lastly, the cysteine double substituted C6,11 peptide has a surface structure on Pd similar to C6 and C11 based on equal ellipticity values, but it contains peaks which correlate to Pd-bound C6. In total, this suggests that the cysteine in the peptide six position affects the overall surface structure, while the presence of histidine or alanine at the eleven position attenuates the magnitude of ellipticity, resulting in a less native peptide structure. When binding residues are present in both the six and eleven positions, the peptides adopt a more unfolded structure on the Pd surface due to a dual binding motif. It is interesting to note that peptides with cysteine modifications at the same site (C6 and C6A11 versus C11 and

A6C11) have remarkably similar CD spectra when bound to the particle (Appendix III, **Figure A3.3**).

4.4.4 Nanoparticle Activity Differences with Respect to Cys-Substitution

Upon characterization of the particle surface structure, Stille C-C coupling was used to probe the catalytic activity of the particles (**Figure 4.5**). This can then be employed to ascertain the structural effects of the peptides on the overall material properties. Note that particles of nearly identical sizes are employed for this reaction, thus differences in the reactivity are most likely attributable to changes in the peptide/particle surface structure. For this reaction, the coupling of 4-iodobenzoic acid with $PhSnCl_3$ to prepare biphenylcarboxylic acid in water at room temperature was used. From these studies, an increase in catalytic activity was noted based upon the cysteine modifications to the peptide sequences as compared to the particles prepared with the parent Pd4.[138] Such results were quite surprising as thiols are well-known poisons for noble metal-based nanocatalysts.[151,152] The non-poisoning effect is likely to be attenuated by the binding of the additional sequence residues to the particle surface, as discussed below. For comparison, as previously reported, the Pd4-capped particles demonstrate a TOF value of 2234 ± 99 mol product (mol Pd × hr)$^{-1}$.[138] For the particles capped with C6, C6,11, and C6A11 peptides, an approximate two-fold increase in the reaction efficiency was observed, displaying TOFs of 3963 ± 28 mol product (mol Pd × hr)$^{-1}$, 3974 ± 280 mol product (mol Pd × hr)$^{-1}$, and 4147 ± 340 mol product (mol Pd × hr)$^{-1}$, respectively. Note that for all of these peptides, the strongest residue binding was incorporated at the six position of the sequence.

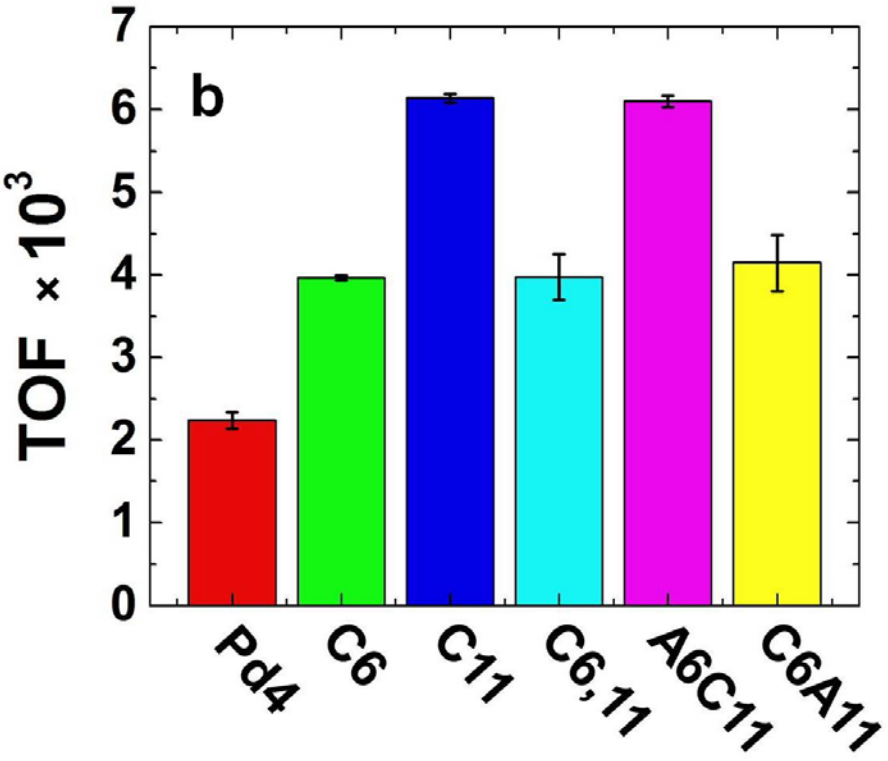

Figure 4.5. TOF analysis of the peptide-capped Pd nanoparticles for the Stille coupling reaction.

Remarkably, a nearly three-fold TOF increase over the Pd4-capped particles for the model reaction was observed for the materials prepared using the C11 and A6C11 with TOF values of 6138 ± 55 mol product (mol Pd × hr)$^{-1}$ and 6097 ± 65 mol product (mol Pd × hr)$^{-1}$, respectively. For these sequences, weaker binding was incorporated at the sixth position as compared to the stronger binding cysteine residue at the eleventh position. Such high TOF values indicate a direct correlation between the peptide sequence, secondary structure (based upon CD), and catalytic reactivity, which suggested high reaction efficiency under aqueous and low temperature conditions with low Pd loadings.

4.5 Summary

Comparing the reactivity of the particles as a function of the cysteine position provides important evidence to indicate that the materials functionality can be directly tuned and substantially enhanced through biomolecule sequence modifications (**Figure 4.1**). To this end, greater TOF values were observed from the particles capped with cysteine-containing peptides over the cysteine-free parent Pd4 sequence. This suggests that such modifications may alter the structure/positioning of the peptide on the particle surface to give rise to this level of reactivity increase. This is highly surprising in light of well-known thiol-based poisoning of catalytic particle surfaces.[152] In general, strong thiol binding at active sites is observed, along with steric crowding at the particle surface, both of which contribute to the diminished reactivity. Such capabilities are likely to be attenuated by the additional functional groups of the peptide sequence binding at the particle surface. This would provide steric bulk to prevent additional thiol-based surface poisoning, while allowing substrate access to the catalytic surface. To this end, these results indicate that thiol-based ligands can be designed as nanoparticle stabilizers for catalytic applications should sufficient offsetting binding moieties be present.

Furthermore, when comparing the five modified sequences, an interesting trend is observed; for those peptides with stronger binding at the eleven position and weaker binding at the six position, increased reactivity with greater TOF values is demonstrated. Such TOFs were substantially larger than those observed for the materials prepared with the other sequences that positioned amino acids with stronger and/or equal binding strengths at the six position over the eleven position. This evidence indicates that the peptide sequence inherently affects the particle functionality and can be used as a design

point to modify particle properties for eventual applications. Furthermore, no observable trends were present between the peptide Pd affinity (ΔG values), the particle size, and the observed reactivity as materials of the same size particles were prepared by all five modified sequences. As such, the observed changes in TOF can be attributed to the bound peptide structure, which likely affects the overall reactivity. These changes in the particle surface morphology, as measured and confirmed by CD, are likely to enhance the reaction mechanism, which has been suggested to follow a unique atom leaching process.[130] For this, changes in the surface bound peptide morphology may more efficiently display the reactive metallic species to the reagents in solution to allow for more rapid Pd leaching during oxidative addition.[130] Should this process be enhanced, additional Pd species would be present in solution to drive the reaction, thus raising the TOF value. Such peptide structural arguments are supported by the CD observations where similar biomolecular structures were observed for the peptides with cysteine at either the six or eleven position, thus directly correlating with the catalytic observations.

4.6 Conclusions

In summary, it has been demonstrated that the properties of peptide-capped nanomaterials can be predicted and directly modulated based upon the peptide sequence. In the present catalytic system, an increase in reactivity was observed as a function of cysteine and alanine substitutions at the selected positions within the peptide sequence. Based upon this effect, peptide rational design was possible, where the placement of such residues within the parent sequence was determined based upon known amino acid affinities and computationally predicted motifs. These results indicate that while biocombinatorial techniques can isolate peptides with optimal affinity, rational design can be employed to

enhance/optimize the functionality of the materials. Through this approach, property enhancement was demonstrated with no apparent changes to the metallic core structure of the materials. Such capabilities could prove to be quite useful for a variety of materials outside of catalytic applications, including plasmonic, magnetic, and electronic structures.

Chapter 5. Appendices

Appendix I

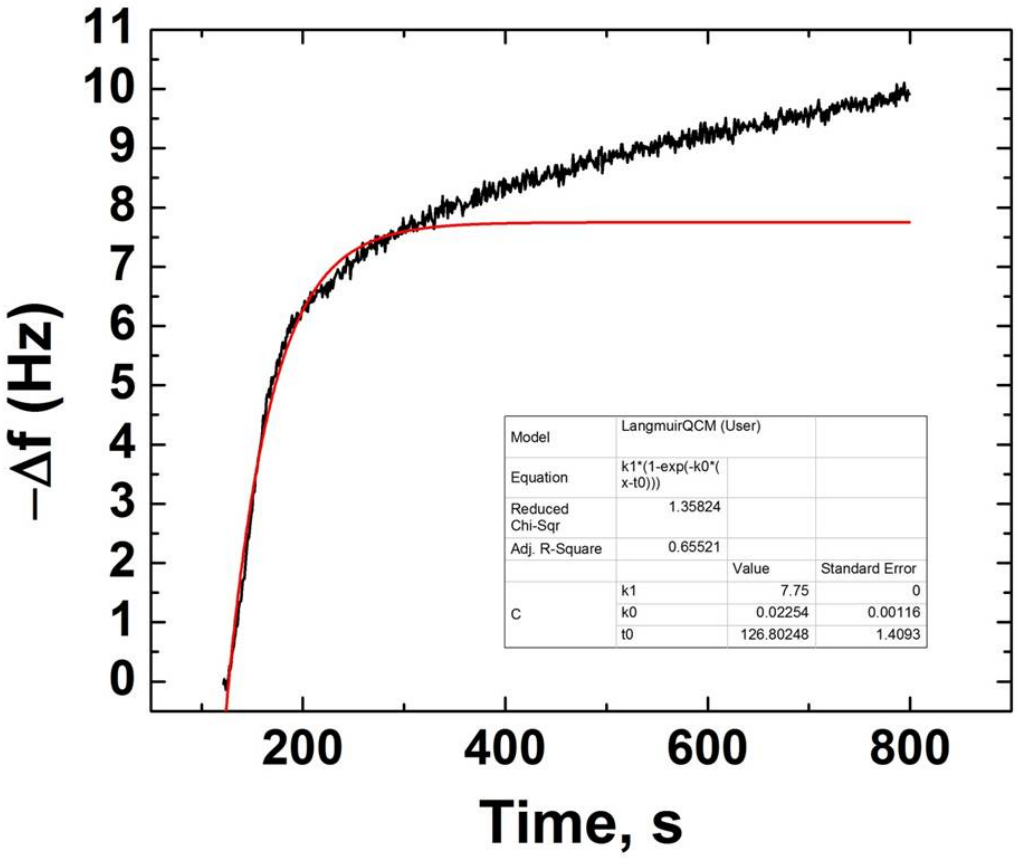

Figure A1.1. Langmuir model fitting of Pd4 binding to Pd-coated sensors at the 15 µg/mL concentration. From this, a kobs is obtained, visible as 0.02254.

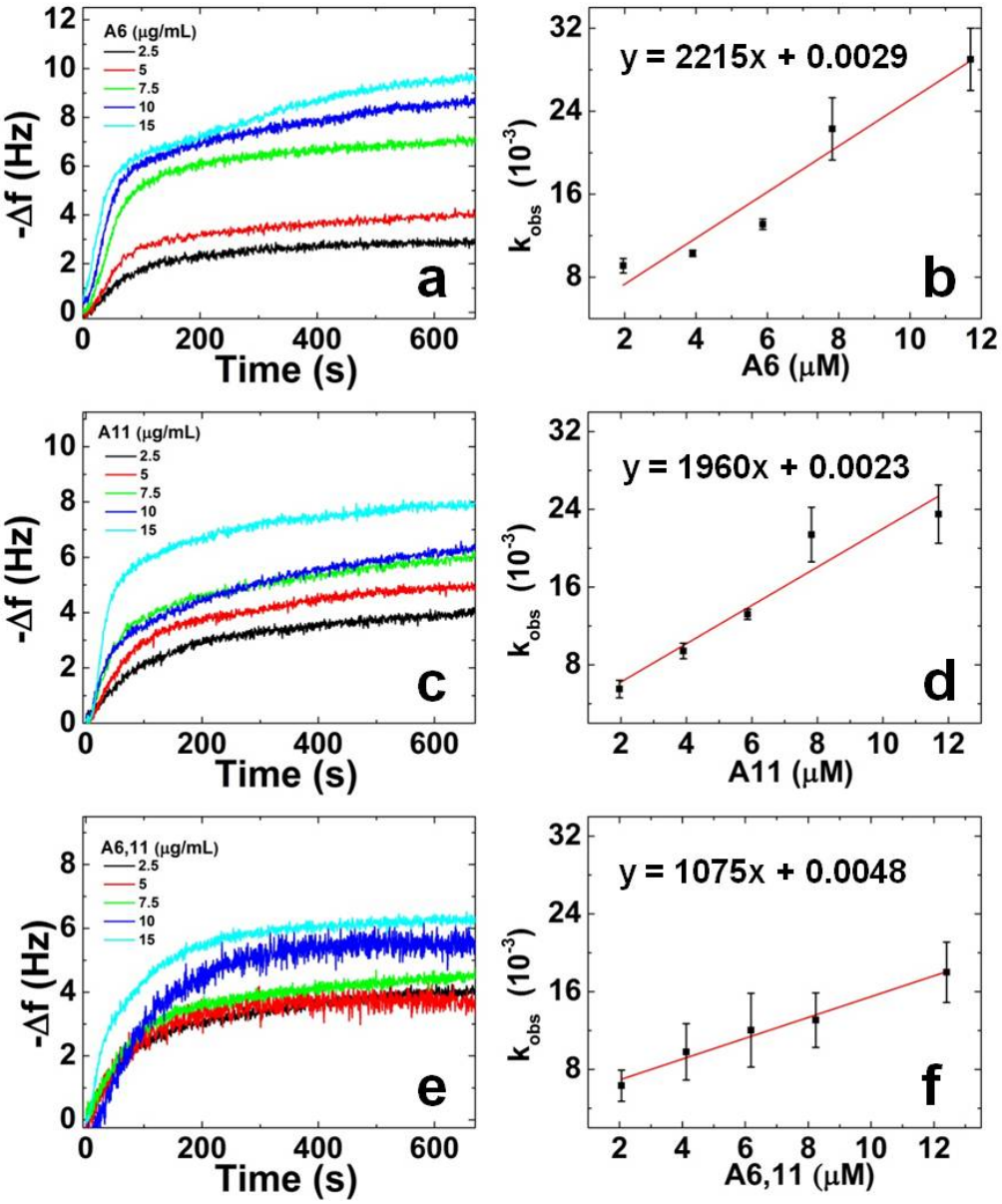

Figure A1.2. QCM spectra of incremental concentrations of five concentrations of the a) A6, c) A11, and e) A6,11 peptides. The kobs values were plotted as a function of concentration and a linear fit assigned for b) A6, d) A11, and f) A6,11.

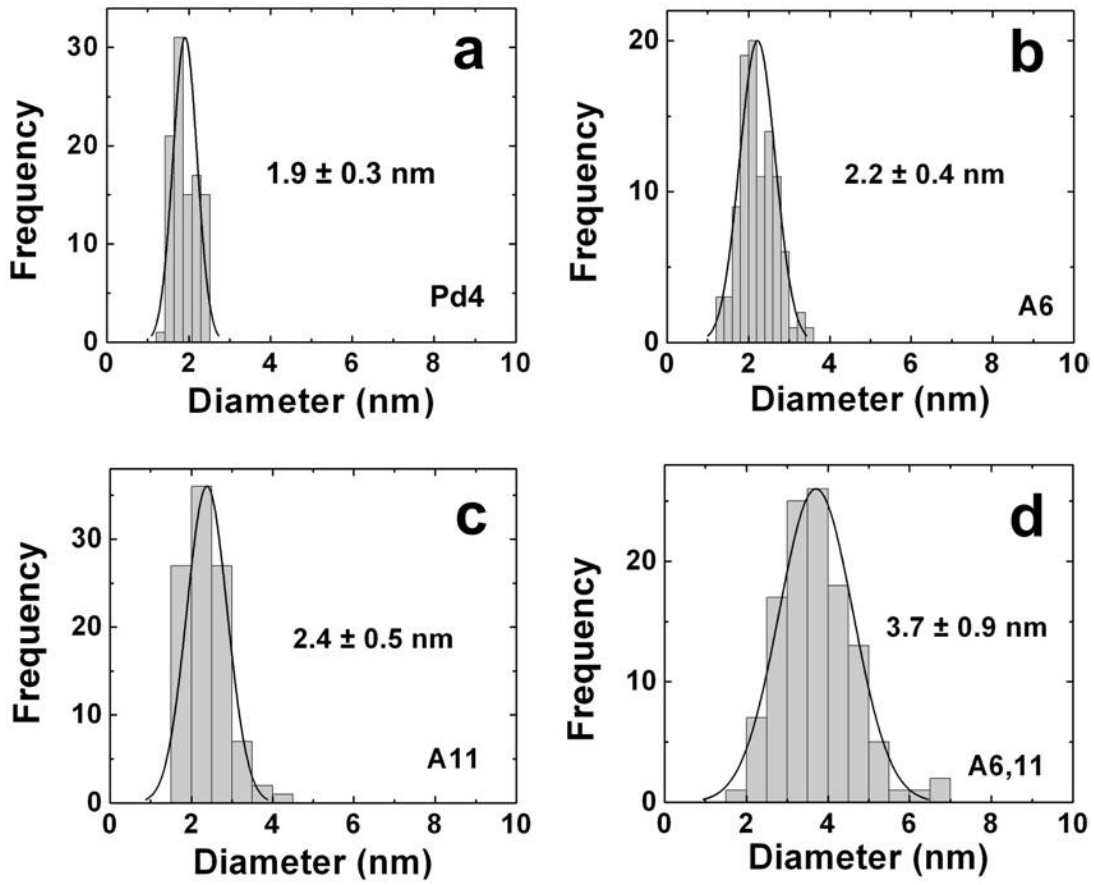

Figure A1.3. Particle size distribution histograms of the Pd nanoparticles prepared using the (a) Pd4, (b) A6, (c) A11, and (d) A6,11 peptides.

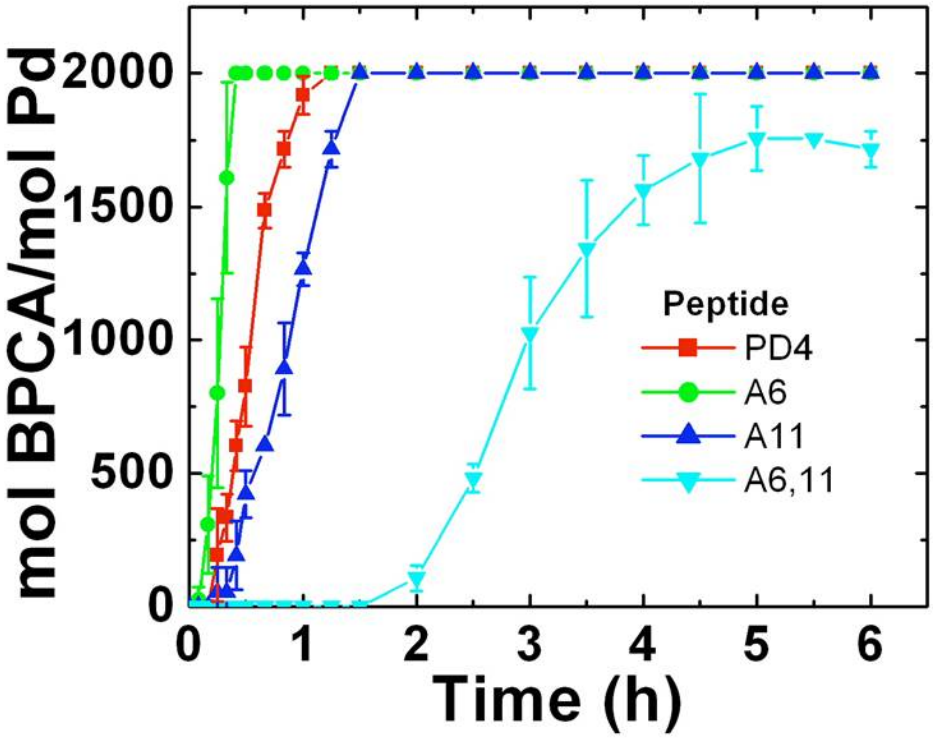

Figure A1.4. Catalytic TOF analysis for the peptide-based materials. The analysis is plotted as the mol BPCA/mol Pd as a function of time, to which the TOF value is obtained through determination of the slope over the linear region of each plot.

Appendix II

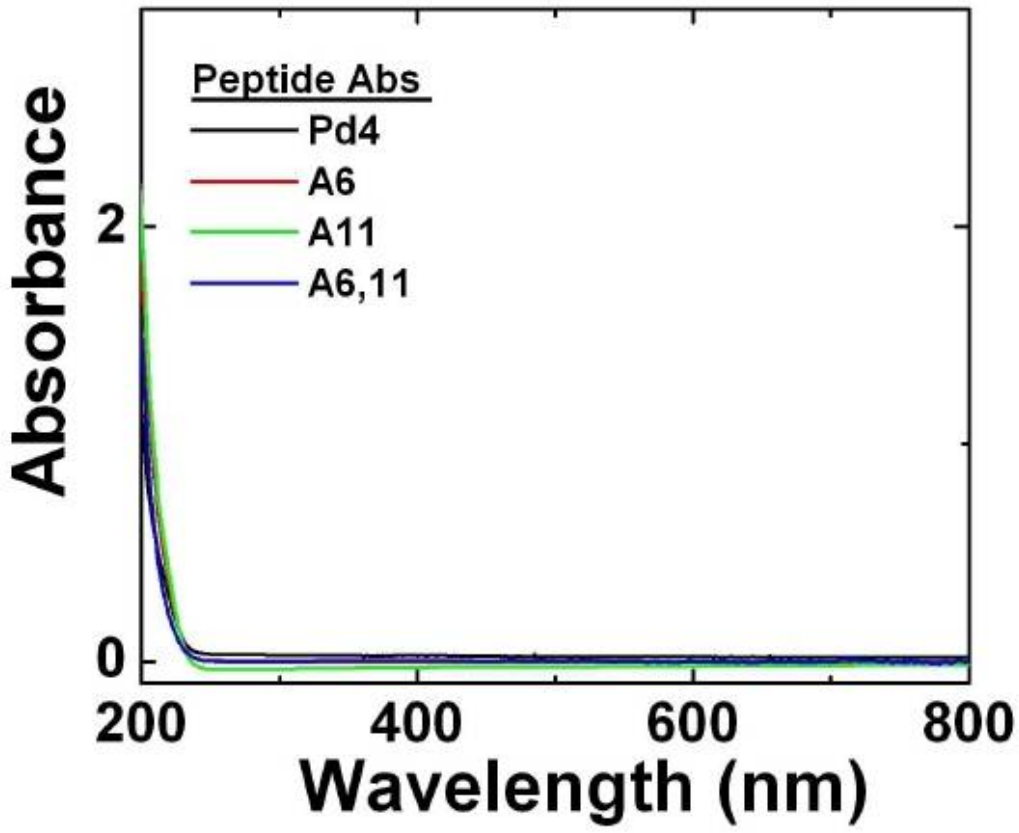

Figure A2.1. UV-vis absorbance of each peptide with water as a blank.

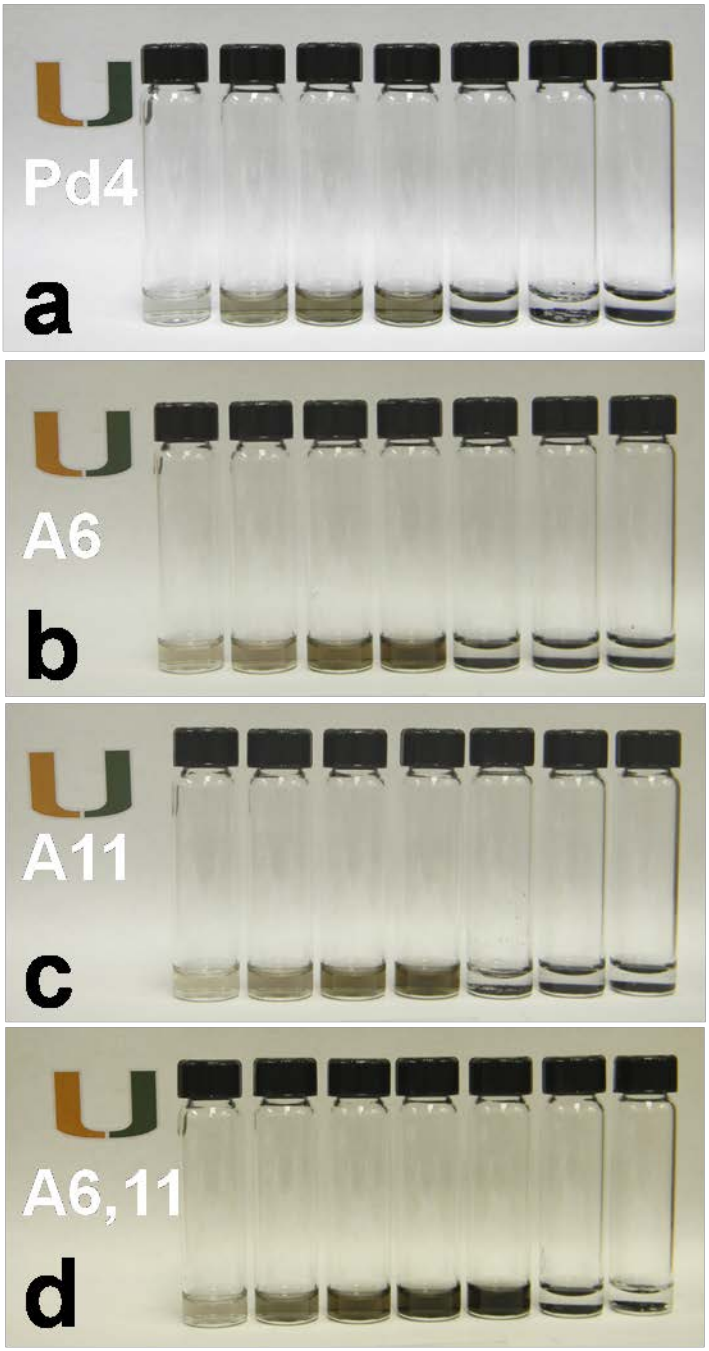

Figure A2.2. Images of nanoparticle systems formed with Pd:peptide ratios 1-7 employed in the presence of peptides a) Pd4, b) A6, c) A11, and d) A6,11, respectively.

Pd:peptide	ζ-potential (mV)
1	−28.6 ± 1.5
2	−28.2 ± 1.1
3	−34.9 ± 0.5
4	−36.7 ± 1.5

Figure A2.3. ζ-potential values for Pd nanoparticles prepared at the Pd:peptide ratios 1-4.

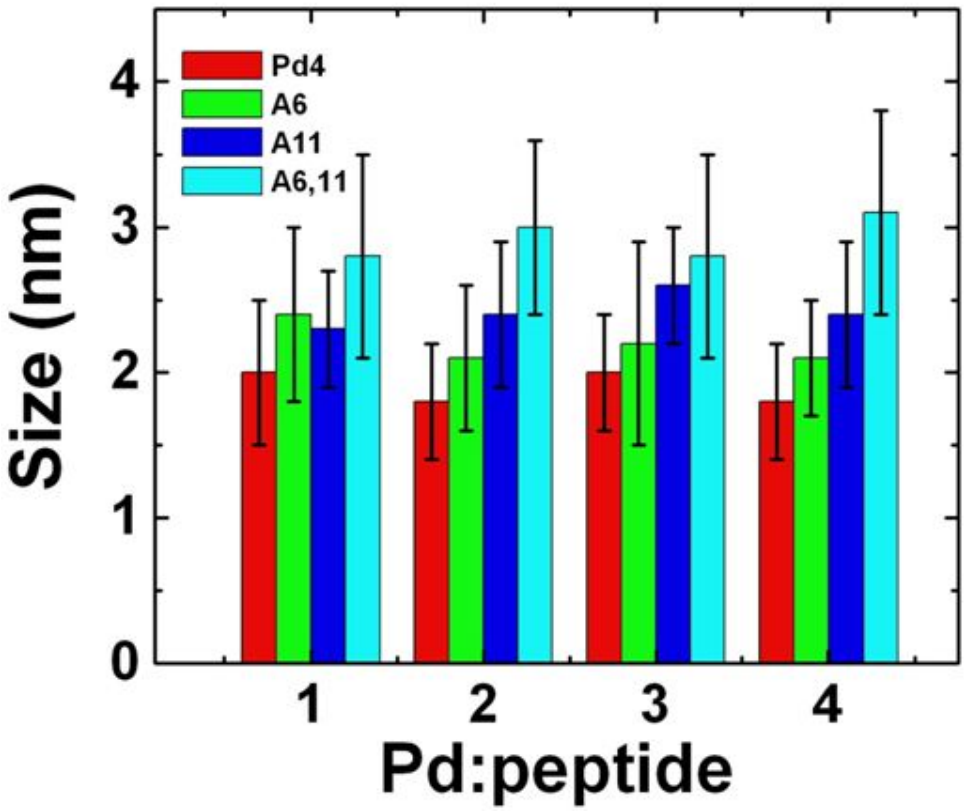

Figure A2.4. Particle size averages for materials prepared with Pd4, A6, A11, and A6,11 at Pd:peptide 1-4.

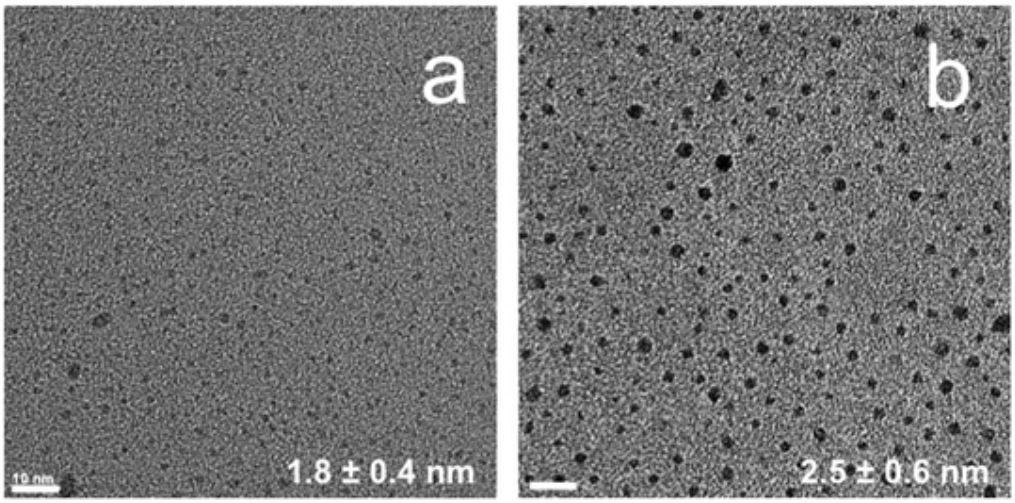

Figure A2.5. TEM images of the effects of the Pd4 peptide addition on the Pd nanoparticle size for particles with peptide added a) prior to reduction and b) after reduction, which results in larger nanoparticle sizes.

Peptide (Ratio)	Helix	3_{10} Helix	Strand	Turn	PP2	Unordered
Pd4 (0)	0.059	0.023	0.26	0.124	0.127	0.406
Pd4 (1)	0.000	0.077	0.148	0.223	0.132	0.420
Pd4 (2)	0.021	0.050	0.326	0.050	0.117	0.437
Pd4 (3)	0.000	0.064	0.202	0.182	0.125	0.427
Pd4 (4)	0.000	0.095	0.225	0.215	0.111	0354
A6 (0)	0.011	0.067	0.033	0.227	0.163	0.498
A6 (1)	0.042	0.031	0.366	0.015	0.042	0.505
A6 (2)	0.032	0.041	0.288	0.117	0.117	0.405
A6 (3)	0.041	0.020	0.364	0.002	0.174	0.399
A6 (4)	0.002	0.067	0.445	0.000	0.173	0.313
A11 (0)	0.153	0.066	0.000	0.239	0.107	0.435
A11 (1)	0.027	0.020	0.381	0.007	0.13	0.436
A11 (2)	0.003	0.046	0.391	0.000	0.159	0.401
A11 (3)	0.000	0.027	0.400	0.000	0.172	0.402
A11 (4)	0.074	0.000	0.299	0.099	0.143	0.385
A6,11 (0)	0.000	0.098	0.021	0.269	0.142	0.469
A6,11 (1)	0.109	0.036	0.121	0.146	0.141	0.449
A6,11 (2)	0.094	0.007	0.182	0.131	0.149	0.438
A6,11 (3)	0.056	0.000	0.366	0.028	0.121	0.429
A6,11 (4)	0.029	0.001	0.386	0.039	0.120	0.425

Figure A2.6. Secondary structure components of peptides when in complex form with incremental Pd:peptide ratio Pd^{2+} ions 1-4.

Peptide (Ratio)	Helix	3_{10} Helix	Strand	Turn	PP2	Unordered
Pd4 (0)	0.059	0.023	0.26	0.124	0.127	0.406
Pd4 (1)	0.010	0.072	0.037	0.237	0.158	0.485
Pd4 (2)	0.000	0.072	0.086	0.222	0.138	0.482
Pd4 (3)	0.025	0.061	0.081	0.217	0.153	0.464
Pd4 (4)	0.029	0.047	0.186	0.166	0.108	0.464
A6 (0)	0.011	0.067	0.033	0.227	0.163	0.498
A6 (1)	0.051	0.040	0.048	0.170	0.170	0.521
A6 (2)	0.023	0.026	0.115	0.170	0.156	0.510
A6 (3)	0.028	0.034	0.243	0.022	0.143	0.530
A6 (4)	0.015	0.037	0.161	0.175	0.130	0.482
A11 (0)	0.153	0.066	0.000	0.239	0.107	0.435
A11 (1)	0.056	0.011	0.204	0.026	0.171	0.532
A11 (2)	0.003	0.018	0.329	0.024	0.130	0.495
A11 (3)	0.012	0.006	0.369	0.000	0.121	0.491
A11 (4)	0.014	0.006	0.316	0.061	0.127	0.475
A6,11 (0)	0.000	0.098	0.021	0.269	0.142	0.469
A6,11 (1)	0.008	0.064	0.029	0.227	0.156	0.515
A6,11 (2)	0.001	0.068	0.000	0.261	0.216	0.454
A6,11 (3)	0.029	0.071	0.000	0.246	0.171	0.484
A6,11 (4)	0.058	0.061	0.039	0.282	0.102	0.457

Figure A2.7. Secondary structure components of peptides when in bound to the nanoparticle surface with incremental Pd:peptide ratios 1-4.

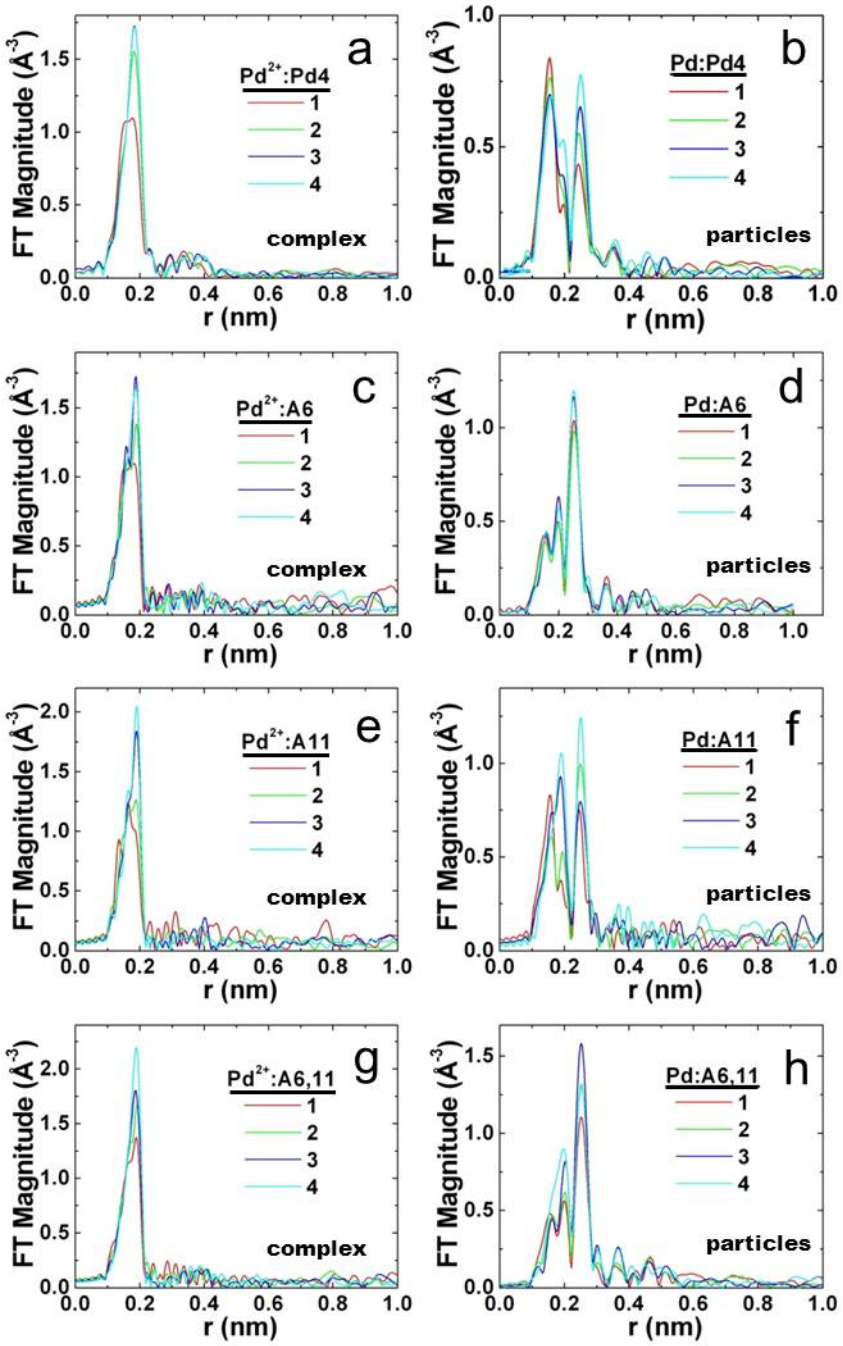

Figure A2.8. EXAFS r-space analysis of the described Pd:peptide ratios with the Pd^{2+} complex for a) Pd4, c) A6, e) A11, and g) A6,11 peptides. Analysis of the reduced materials for in r-space were performed for b) Pd4, d) A6, f) A11, and h) A6,11.

Appendix III

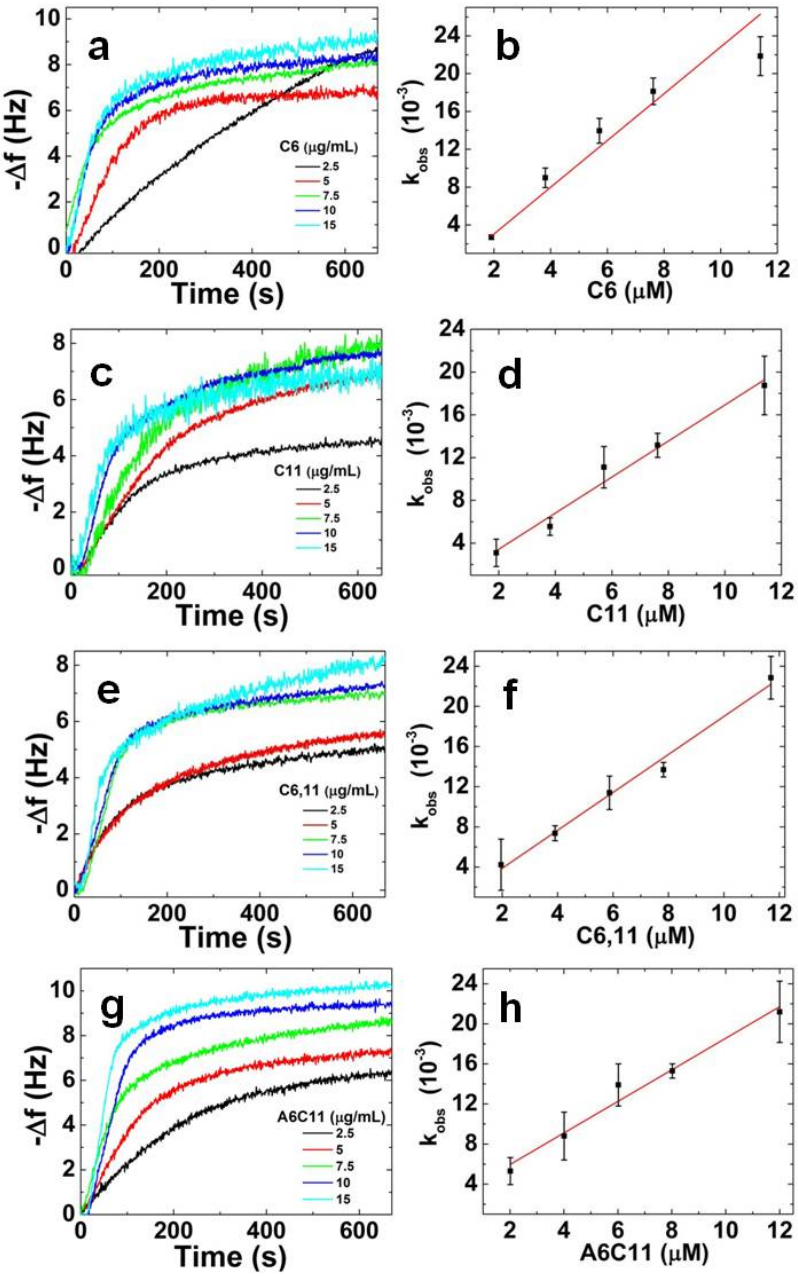

Figure A3.1. The QCM measurements obtained from various concentrations for the a) C6, c) C11, e) C6,11, and g) A6C11 peptides, respectively. The corresponding linear fit of kobs values to the right of each QCM measurement for b) C6, d) C11, f) C6,11, and h) A6C11 peptides, which yields the slope and intercept, as the k_a and k_d, respectively.

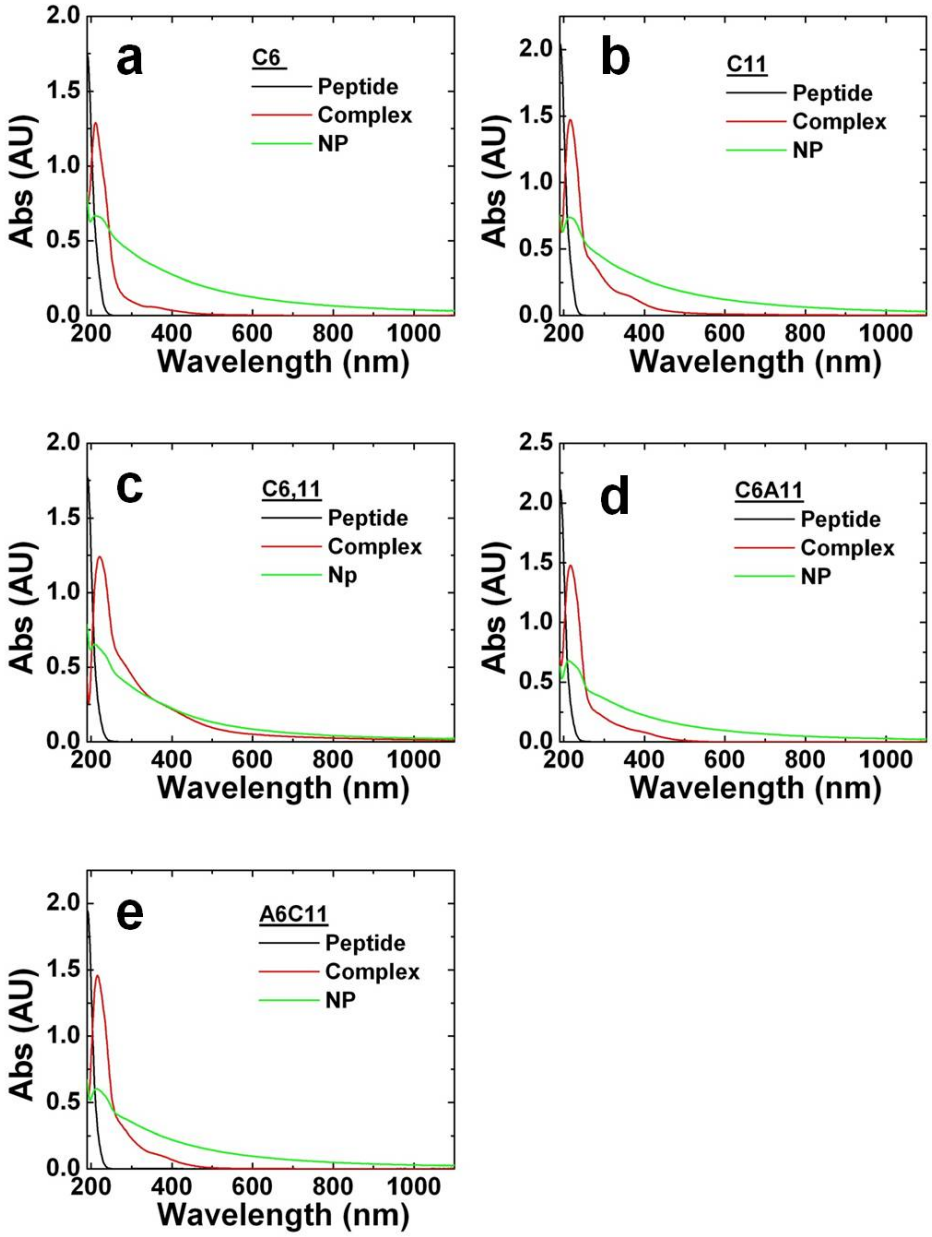

Figure A3.2. UV-vis analysis of the cys-analogues a) C6, b) C11, c) C6,11, d) A6C11, and e) C6A11, the complexes formed upon addition of K_2PdCl_4, and the resulting nanomaterials after reduction.

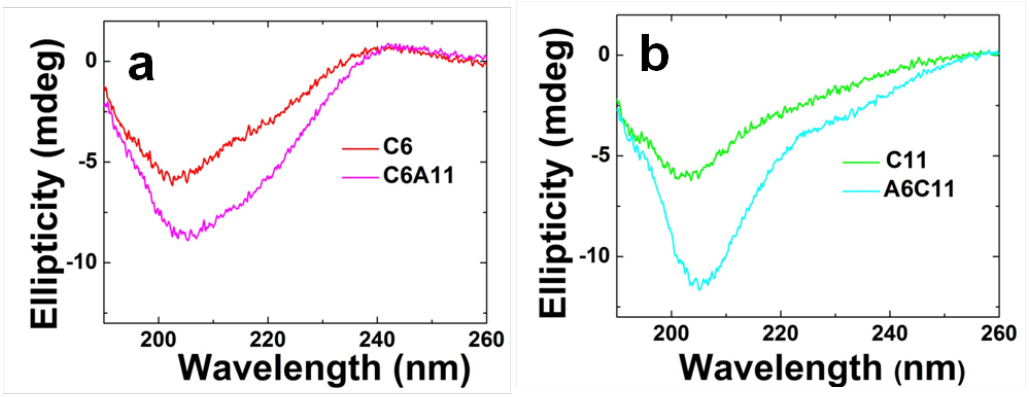

c

Peptide	Helix	3_{10} Helix	Strand	Turn	PP2	Unord.
C6A11	0.013	0.023	0.224	0.155	0.130	0.455
Pd-C6A11	0.000	0.020	0.197	0.127	0.177	0.480
A6C11	0.018	0.027	0.238	0.159	0.120	0.440
Pd-A6C11	0.080	0.000	0.170	0.140	0.112	0.497
C11	0.010	0.023	0.231	0.143	0.136	0.457
Pd-C11	0.025	0.023	0.227	0.159	0.118	0.447
C6	0.005	0.022	0.239	0.139	0.137	0.458
Pd-C6	0.000	0.028	0.259	0.094	0.155	0.464
C6,11	0.013	0.027	0.222	0.161	0.118	0.459
Pd-C6,11	0.004	0.013	0.148	0.128	0.175	0.532

Figure A3.3. CD spectra of peptides a) C6 and C6A11 in addition to b) C11 and A6C11, respectively, which illustrate their structural similarities based on CD absorbance. Secondary structure contributions of peptides deconvoluted from CD spectra using CDPro software (c).

References

(1) *Market Report: Global Catalyst Market, 2nd Edition.* **2011**, *1*.

(2) Joos, F.; Plattner, G. K.; Stocker, T. F.; Marchal, O.; Schmittner, A. *Science* **1999**, *284*, 464.

(3) Doney, S. C.; Fabry, V. J.; Feely, R. A.; Kleypas, J. A. *Annual Review of Marine Science* **2009**, *1*, 169.

(4) Jenkinson, D. S.; Adams, D. E.; Wild, A. *Nature* **1991**, *351*, 304.

(5) Silvy, R. P. *Oil Gas-European Magazine* **2003**, *29*, 108.

(6) Voityuk, A. A. *Mol. Biol.* **1987**, *21*, 729.

(7) Temkin, O. N. *Kinet. Catal.* **2012**, *53*, 313.

(8) Astruc, D. *Inorg. Chem.* **2007**, *46*, 1884.

(9) Stille, J. K. *Angew. Chem., Int. Ed.* **1986**, *25*, 508.

(10) Armor, J. N. *Appl. Catal., A* **2000**, *194*, 3.

(11) Centi, G.; Ciambelli, P.; Perathoner, S.; Russo, P. *Catal. Today* **2002**, *75*, 3.

(12) Widegren, J. A.; Finke, R. G. *J. Mol. Catal. A: Chem.* **2003**, *198*, 317.

(13) Wang, D. S.; Xie, T.; Li, Y. D. *Nano Research* **2009**, *2*, 30.

(14) Braunstein, P. *J. Organomet. Chem.* **2004**, *689*, 3953.

(15) Mirkin, C. A. *Inorg. Chem.* **2000**, *39*, 2258.

(16) Guo, S. J.; Fang, Y. X.; Dong, S. J.; Wang, E. K. *J. Phys. Chem. C* **2007**, *111*, 17104.

(17) Polleux, J.; Pinna, N.; Antonietti, M.; Hess, C.; Wild, U.; Schlogl, R.; Niederberger, M. *Chem. Eur. J.* **2005**, *11*, 3541.

(18) Lynch, I.; Dawson, K. A. *Nano Today* **2008**, *3*, 40.

(19) Fang, C.; Bhattarai, N.; Sun, C.; Zhang, M. Q. *Small* **2009**, *5*, 1637.

(20) Gref, R.; Couvreur, P.; Barratt, G.; Mysiakine, E. *Biomaterials* **2003**, *24*, 4529.

(21) Pasquato, L.; Pengo, P.; Scrimin, P. *Supramol. Chem.* **2005**, *17*, 163.

(22) Dickerson, M. B.; Sandhage, K. H.; Naik, R. R. *Chem. Rev.* **2008**, *108*, 4935.

(23) Dickerson, M. B.; Jones, S. E.; Cai, Y.; Ahmad, G.; Naik, R. R.; Kroger, N.; Sandhage, K. H. *Chem. Mater.* **2008**, *20*, 1578.

(24) Lee, S. W.; Mao, C. B.; Flynn, C. E.; Belcher, A. M. *Science* **2002**, *296*, 892.

(25) Jakhmola, A.; Bhandari, R.; Pacardo, D. B.; Knecht, M. R. *J. Mater. Chem.* **2010**, *20*, 1522.

(26) Pacardo, D. B.; Sethi, M.; Jones, S. E.; Naik, R. R.; Knecht, M. R. *ACS Nano* **2009**, *3*, 1288.

(27) Bhandari, R.; Coppage, R.; Knecht, M. R. *Catal. Sci. Technol.* **2012**, *2*, 256.

(28) Slocik, J. M.; Naik, R. R. *Adv. Mater.* **2006**, *18*, 1988.

(29) Kreuter, J. *J. Nanosci. Nanotechno.* **2004**, *4*, 484.

(30) Song, C. S. *Catal. Today* **2002**, *77*, 17.

(31) Cuenya, B. R. *Thin Solid Films* **2010**, *518*, 3127.

(32) Herves, P.; Perez-Lorenzo, M.; Liz-Marzan, L. M.; Dzubiella, J.; Lu, Y.; Ballauff, M. *Chem. Soc. Rev.* **2012**, *41*, 5577.

(33) Rana, S.; Yeh, Y. C.; Rotello, V. M. *Curr. Opin. Chem. Biol.* **2010**, *14*, 828.

(34) Pengo, P.; Baltzer, L.; Pasquato, L.; Scrimin, P. *Angew. Chem., Int. Ed.* **2007**, *46*, 400.

(35) Samanta, B.; Yan, H.; Fischer, N. O.; Shi, J.; Jerry, D. J.; Rotello, V. M. *J. Mater. Chem.* **2008**, *18*, 1204.

(36) Heinz, H.; Farmer, B. L.; Pandey, R. B.; Slocik, J. M.; Patnaik, S. S.; Pachter, R.; Naik, R. R. *J. Am. Chem. Soc.* **2009**, *131*, 9704.

(37) Naik, R. R.; Jones, S. E.; Murray, C. J.; McAuliffe, J. C.; Vaia, R. A.; Stone, M. O. *Adv. Funct. Mater.* **2004**, *14*, 25.

(38) Flynn, C. E.; Lee, S. W.; Peelle, B. R.; Belcher, A. M. *Acta Mater.* **2003**, *51*, 5867.

(39) Hess, G. T.; Cragnolini, J. J.; Popp, M. W.; Allen, M. A.; Dougan, S. K.; Spooner, E.; Ploegh, H. L.; Belcher, A. M.; Guimaraes, C. P. *Bioconjugate Chem.* **2012**, *23*, 1478.

(40) Nam, K. T.; Kim, D. W.; Yoo, P. J.; Chiang, C. Y.; Meethong, N.; Hammond, P. T.; Chiang, Y. M.; Belcher, A. M. *Science* **2006**, *312*, 885.

(41) Lee, Y.; Kim, J.; Yun, D. S.; Nam, Y. S.; Shao-Horn, Y.; Belcher, A. M. *Energy Environ. Sci.* **2012**, *5*, 8328.

(42) Li, Z. P.; Koch, H.; Dubel, S. *J. Mol. Microbiol. Biotechnol.* **2003**, *6*, 57.

(43) Sarikaya, M.; Tamerler, C.; Jen, A. K. Y.; Schulten, K.; Baneyx, F. *Nature Materials* **2003**, *2*, 577.

(44) Mejare, M.; Ljung, S.; Bulow, L. *Protein Eng.* **1998**, *11*, 489.

(45) Feng, J.; Pandey, R. B.; Berry, R. J.; Farmer, B. L.; Naik, R. R.; Heinz, H. *Soft Matter* **2011**, *7*, 2113.

(46) Mejare, M.; Bulow, L. *Trends Biotechnol.* **2001**, *19*, 67.

(47) Ulijn, R. V.; Smith, A. M. *Chem. Soc. Rev.* **2008**, *37*, 664.

(48) Li, Y. J.; Huang, Y. *Adv. Mater.* **2010**, *22*, 1921.

(49) Ruan, L. Y.; Chiu, C. Y.; Li, Y. J.; Huang, Y. *Nano Lett.* **2011**, *11*, 3040.

(50) Khatayevich, D.; So, C. R.; Hayamizu, Y.; Gresswell, C.; Sarikaya, M. *Langmuir* **2012**, *28*, 8589.

(51) Pumera, M. *Mater. Today* **2011**, *14*, 308.

(52) Dong, X. C.; Huang, W.; Chen, P. *Nanoscale Res. Lett.* **2011**, *6*.

(53) Gorjizadeh, N.; Kawazoe, Y. *J. Nanomater.* **2010**.

(54) Cui, Y.; Kim, S. N.; Jones, S. E.; Wissler, L. L.; Naik, R. R.; McAlpine, M. C. *Nano Lett.* **2010**, *10*, 4559.

(55) Han, T. H.; Lee, W. J.; Lee, D. H.; Kim, J. E.; Choi, E. Y.; Kim, S. O. *Adv. Mater.* **2010**, *22*, 2060.

(56) So, C. R.; Hayamizu, Y.; Yazici, H.; Gresswell, C.; Khatayevich, D.; Tamerler, C.; Sarikaya, M. *ACS Nano* **2012**, *6*, 1648.

(57) Seker, U. O. S.; Zengin, G.; Tamerer, C.; Sarikaya, M.; Demir, H. V. *Langmuir* **2011**, *27*, 4867.

(58) Sano, T.; Cantor, C. R. *Proceedings of the National Academy of Sciences of the United States of America* **1995**, *92*, 3180.

(59) Weber, P. C.; Ohlendorf, D. H.; Wendoloski, J. J.; Salemme, F. R. *Science* **1989**, *243*, 85.

(60) So, C. R.; Tamerler, C.; Sarikaya, M. *Angew. Chem., Int. Ed.* **2009**, *48*, 5174.

(61) Tamerler, C.; Oren, E. E.; Duman, M.; Venkatasubramanian, E.; Sarikaya, M. *Langmuir* **2006**, *22*, 7712.

(62) Rhee, C. K.; Kim, B. J.; Ham, C.; Kim, Y. J.; Song, K.; Kwon, K. *Langmuir* **2009**, *25*, 7140.

(63) Li, H.; Sun, C. L.; Yu, M. A.; Yu, D. G.; Li, B. J.; Shi, Z. J. *Chem. Eur. J.* **2011**, *17*, 3593.

(64) Bazzanella, N.; Checchetto, R.; Miotello, A. *J. Nanomater.* **2011**.

(65) Vallee, A.; Humblot, V.; Pradier, C. M. *Acc. Chem. Res.* **2010**, *43*, 1297.

(66) Zhou, B.; Hermans, S.; Somorjai, G. A.; American Chemical Society. Meeting. *Nanotechnology in catalysis*; Kluwer Academic/Plenum Publishers: New York, 2004.

(67) Manea, F.; Houillon, F. B.; Pasquato, L.; Scrimin, P. *Angew. Chem., Int. Ed.* **2004**, *43*, 6165.

(68) De, D. D.; Englehardt, J. D.; Kalu, E. E. *J. Electrochem. Soc.* **2000**, *147*, 4573.

(69) Ikeda, S.; Ishino, S.; Harada, T.; Okamoto, N.; Sakata, T.; Mori, H.; Kuwabata, S.; Torimoto, T.; Matsumura, M. *Angew. Chem., Int. Ed.* **2006**, *45*, 7063.

(70) Hagiwara, H.; Kumagae, K.; Ishihara, T. *Chem. Lett.* **2010**, *39*, 498.

(71) Gasteiger, H. A.; Kocha, S. S.; Sompalli, B.; Wagner, F. T. *Appl. Catal., B* **2005**, *56*, 9.

(72) Chiu, C. Y.; Li, Y. J.; Ruan, L. Y.; Ye, X. C.; Murray, C. B.; Huang, Y. *Nat. Chem.* **2011**, *3*, 393.

(73) Zhang, D. S.; Du, X. J.; Shi, L. Y.; Gao, R. H. *Dalton Trans.* **2012**, *41*, 14455.

(74) Lisiecki, I. *J. Phys. Chem. B* **2005**, *109*, 12231.

(75) Chen, Y.; Lin, Y. C.; Huang, C. W.; Wang, C. W.; Chen, L. J.; Wu, W. W.; Huang, Y. *Nano Lett.* **2012**, *12*, 3115.

(76) Mukerjee, S. *J. Appl. Electrochem.* **1990**, *20*, 537.

(77) Huang, J.; Jiang, T.; Gao, H. X.; Han, B. X.; Liu, Z. M.; Wu, W. Z.; Chang, Y. H.; Zhao, G. Y. *Angew. Chem., Int. Ed.* **2004**, *43*, 1397.

(78) Wang, Y. G.; Shah, N.; Huffman, G. P. *Energ. Fuel.* **2004**, *18*, 1429.

(79) Bianchini, C.; Shen, P. K. *Chem. Rev.* **2009**, *109*, 4183.

(80) Pandey, R. B.; Heinz, H.; Feng, J.; Farmer, B. L.; Slocik, J. M.; Drummy, L. F.; Naik, R. R. *PCCP* **2009**, *11*, 1989.

(81) Durand, J.; Teuma, E.; Gomez, M. *Eur. J. Inorg. Chem.* **2008**, 3577.

(82) Ramezani-Dakhel, H.; Mirau, P. A.; Naik, R. R.; Knecht, M. R.; Heinz, H. *PCCP* **2013**.

(83) Pacardo, D. B.; Slocik, J. M.; Kirk, K. C.; Naik, R. R.; Knecht, M. R. *Nanoscale* **2011**, *3*, 2194.

(84) Pacardo, D. B.; Knecht, M. R. *Catal. Sci. Technol.* **2013**, *3*, 745.

(85) Stille, J. K.; Lau, K. S. Y. *Acc. Chem. Res.* **1977**, *10*, 434.

(86) Slocik, J. M.; Govorov, A. O.; Naik, R. R. *Angew. Chem., Int. Ed.* **2008**, *47*, 5335.

(87) Rodriguez, J. A.; Goodman, D. W. *Science* **1992**, *257*, 897.

(88) Zhou, S. H.; Jackson, G. S.; Eichhorn, B. *Adv. Funct. Mater.* **2007**, *17*, 3099.

(89) Hou, W. B.; Dehm, N. A.; Scott, R. W. J. *J. Catal.* **2008**, *253*, 22.

(90) Stumpf, H. O.; Pei, Y.; Kahn, O.; Sletten, J.; Renard, J. P. *J. Am. Chem. Soc.* **1993**, *115*, 6738.

(91) Xu, C. X.; Zhang, Y.; Wang, L. Q.; Xu, L. Q.; Bian, X. F.; Ma, H. Y.; Ding, Y. *Chem. Mater.* **2009**, *21*, 3110.

(92) Sinfelt, J. H.; Via, G. H.; Lytle, F. W. *J. Chem. Phys.* **1980**, *72*, 4832.

(93) Wang, L. Y.; Park, H. Y.; Lim, S. I. I.; Schadt, M. J.; Mott, D.; Luo, J.; Wang, X.; Zhong, C. J. *J. Mater. Chem.* **2008**, *18*, 2629.

(94) Han, J. G.; Zhao, R. N.; Duan, Y. H. *J. Phys. Chem. A* **2007**, *111*, 2148.

(95) Stamenkovic, V. R.; Mun, B. S.; Arenz, M.; Mayrhofer, K. J. J.; Lucas, C. A.; Wang, G. F.; Ross, P. N.; Markovic, N. M. *Nature Materials* **2007**, *6*, 241.

(96) Coq, B.; Figueras, F. *J. Mol. Catal. A: Chem.* **2001**, *173*, 117.

(97) Dash, P.; Dehm, N. A.; Scott, R. W. J. *J. Mol. Catal. A: Chem.* **2008**, *286*, 114.

(98) Murray, J.; Macartney, D.; Thatcher, G. R. J. *Org. Lett.* **2001**, *3*, 3635.

(99) Lee, H. J.; Chen, P.; Moon, S. J.; Sauvage, F.; Sivula, K.; Bessho, T.; Gamelin, D. R.; Comte, P.; Zakeeruddin, S. M.; Il Seok, S.; Gratzel, M.; Nazeeruddin, M. K. *Langmuir* **2009**, *25*, 7602.

(100) Bhandari, R.; Knecht, M. R. *Catal. Sci. Technol.* **2012**, *2*, 1360.

(101) Bhandari, R.; Knecht, M. R. *Langmuir* **2012**, *28*, 8110.

(102) Kroger, N.; Deutzmann, R.; Sumper, M. *Science* **1999**, *286*, 1129.

(103) Knecht, M. R.; Wright, D. W. *Chem. Commun.* **2003**, 3038.

(104) Sidhaye, D. S.; Kashyap, S.; Sastry, M.; Hotha, S.; Prasad, B. L. V. *Langmuir* **2005**, *21*, 7979.

(105) Praharaj, S.; Nath, S.; Ghosh, S. K.; Kundu, S.; Pal, T. *Langmuir* **2004**, *20*, 9889.

(106) Mott, D.; Luo, J.; Njoki, P. N.; Lin, Y.; Wang, L. Y.; Zhong, C. J. *Catal. Today* **2007**, *122*, 378.

(107) Andreiadis, E. S.; Vitale, M. R.; Mezailles, N.; Le Goff, X.; Le Floch, P.; Toullec, P. Y.; Michelet, V. *Dalton Trans.* **2010**, *39*, 10608.

(108) Fleming, D. A.; Thode, C. J.; Williams, M. E. *Chem. Mater.* **2006**, *18*, 2327.

(109) Lee, S. K.; Yun, D. S.; Belcher, A. M. *Biomacromolecules* **2006**, *7*, 14.

(110) Mao, C. B.; Solis, D. J.; Reiss, B. D.; Kottmann, S. T.; Sweeney, R. Y.; Hayhurst, A.; Georgiou, G.; Iverson, B.; Belcher, A. M. *Science* **2004**, *303*, 213.

(111) Huang, Y.; Chiang, C. Y.; Lee, S. K.; Gao, Y.; Hu, E. L.; De Yoreo, J.; Belcher, A. M. *Nano Lett.* **2005**, *5*, 1429.

(112) Anandan, S.; Grieser, F.; Ashokkumar, M. *J. Phys. Chem. C* **2008**, *112*, 15102.

(113) Guo, S. J.; Wang, E. K. *Nano Today* **2011**, *6*, 240.

(114) Ataee-Esfahani, H.; Wang, L.; Nemoto, Y.; Yamauchi, Y. *Chem. Mater.* **2010**, *22*, 6310.

(115) Seferos, D. S.; Giljohann, D. A.; Hill, H. D.; Prigodich, A. E.; Mirkin, C. A. *J. Am. Chem. Soc.* **2007**, *129*, 15477.

(116) Busbee, B. D.; Obare, S. O.; Murphy, C. J. *Adv. Mater.* **2003**, *15*, 414.

(117) Nam, Y. S.; Shin, T.; Park, H.; Magyar, A. P.; Choi, K.; Fantner, G.; Nelson, K. A.; Belcher, A. M. *J. Am. Chem. Soc.* **2010**, *132*, 1462.

(118) Nam, Y. S.; Magyar, A. P.; Lee, D.; Kim, J. W.; Yun, D. S.; Park, H.; Pollom, T. S.; Weitz, D. A.; Belcher, A. M. *Nature Nanotech.* **2010**, *5*, 340.

(119) Neltner, B.; Peddie, B.; Xu, A.; Doenlen, W.; Durand, K.; Yun, D. S.; Speakman, S.; Peterson, A.; Belcher, A. *ACS Nano* **2010**, *4*, 3227.

(120) Diagne, C.; Idriss, H.; Kiennemann, A. *Catal. Commun.* **2002**, *3*, 565.

(121) Kugai, J.; Velu, S.; Song, C. S. *Catal. Lett.* **2005**, *101*, 255.

(122) Slocik, J. M.; Zabinski, J. S.; Phillips, D. M.; Naik, R. R. *Small* **2008**, *4*, 548.

(123) Lee, Y. J.; Yi, H.; Kim, W. J.; Kang, K.; Yun, D. S.; Strano, M. S.; Ceder, G.; Belcher, A. M. *Science* **2009**, *324*, 1051.

(124) Chen, C. L.; Zhang, P. J.; Rosi, N. L. *J. Am. Chem. Soc.* **2008**, *130*, 13555.

(125) Sethi, M.; Knecht, M. R. *ACS Appl. Mater. Inter.* **2009**, *1*, 1270.

(126) Knecht, M. R.; Weir, M. G.; Frenkel, A. I.; Crooks, R. M. *Chem. Mater.* **2008**, *20*, 1019.

(127) Tamerler, C.; Duman, M.; Oren, E. E.; Gungormus, M.; Xiong, X. R.; Kacar, T.; Parviz, B. A.; Sarikaya, M. *Small* **2006**, *2*, 1372.

(128) Olmedo, I.; Araya, E.; Sanz, F.; Medina, E.; Arbiol, J.; Toledo, P.; Alvarez-Lueje, A.; Giralt, E.; Kogan, M. J. *Bioconjugate Chem.* **2008**, *19*, 1154.

(129) Wilson, O. M.; Knecht, M. R.; Garcia-Martinez, J. C.; Crooks, R. M. *J. Am. Chem. Soc.* **2006**, *128*, 4510.

(130) Diallo, A. K.; Ornelas, C.; Salmon, L.; Aranzaes, J. R.; Astruc, D. *Angew. Chem., Int. Ed.* **2007**, *46*, 8644.

(131) Ornelas, C.; Ruiz, J.; Salmon, L.; Astruc, D. *Adv. Synth. Catal.* **2008**, *350*, 837.

(132) Phan, N. T. S.; Van Der Sluys, M.; Jones, C. W. *Adv. Synth. Catal.* **2006**, *348*, 609.

(133) Mann, S. *Biomineralization : principles and concepts in bioinorganic materials chemistry*; Oxford University Press: New York, 2001.

(134) Kirschvink, J. L.; Jones, D. S.; MacFadden, B. J. *Magnetite biomineralization and magnetoreception in organisms : a new biomagnetism*; Plenum Press: New York, 1985.

(135) Round, F. E.; Crawford, R. M.; Mann, D. G. *The Diatoms : biology & morphology of the genera*; Cambridge University Press: Cambridge England ; New York, 1990.

(136) Bhandari, R.; Knecht, M. R. *ACS Catalysis* **2011**, *1*, 89.

(137) Coppage, R.; Slocik, J. M.; Briggs, B. D.; Frenkel, A. I.; Heinz, H.; Naik, R. R.; Knecht, M. R. *J. Am. Chem. Soc.* **2011**, *133*, 12346.

(138) Coppage, R.; Slocik, J. M.; Sethi, M.; Pacardo, D. B.; Naik, R. R.; Knecht, M. R. *Angew. Chem., Int. Ed.* **2010**, *49*, 3767.

(139) Kuang, Z. F.; Kim, S. N.; Crookes-Goodson, W. J.; Farmer, B. L.; Naik, R. R. *ACS Nano* **2010**, *4*, 452.

(140) Kim, S. N.; Slocik, J. M.; Naik, R. R. *Small* **2010**, *6*, 1992.

(141) Chen, C. L.; Rosi, N. L. *J. Am. Chem. Soc.* **2010**, *132*, 6902.

(142) Kim, S. N.; Kuang, Z. F.; Slocik, J. M.; Jones, S. E.; Cui, Y.; Farmer, B. L.; McAlpine, M. C.; Naik, R. R. *J. Am. Chem. Soc.* **2011**, *133*, 14480.

(143) Tomasio, S. M.; Walsh, T. R. *J. Phys. Chem. C* **2009**, *113*, 8778.

(144) Yu, J.; Becker, M. L.; Carri, G. A. *Small* **2010**, *6*, 2242.

(145) Frenkel, A. I.; Hills, C. W.; Nuzzo, R. G. *The Journal of Physical Chemistry B* **2001**, *105*, 12689.

(146) Scott, R. W. J.; Ye, H.; Henriquez, R. R.; Crooks, R. M. *Chem. Mater.* **2003**, *15*, 3873.

(147) Skoog, D. A. *Fundamentals of analytical chemistry*; 8th ed.; Thomson-Brooks/Cole: Belmont, CA, 2004.

(148) Bhainsa, K. C.; D'Souza, S. F. *Colloids Surf., B* **2006**, *47*, 160.

(149) Briggs, B. D.; Knecht, M. R. *J. Phys. Chem. Lett.* **2012**, *3*, 405.

(150) Scholle, M. D.; Kehoe, J. W.; Kay, B. K. *Comb. Chem. High T. Scr.* **2005**, *8*, 545.

(151) Quinn, R.; Dahl, T. A.; Toseland, B. A. *Appl. Catal., A* **2004**, *272*, 61.

(152) Ibanez, F. J.; Zamborini, F. P. *Langmuir* **2006**, *22*, 9789.

VITA

Ryan Coppage was born in Owensboro, Kentucky on August 9th, 1981. He attended Ohio County High School and later went to Murray to earn his B.S. and M.S. in Chemistry from Murray State University, Kentucky. While in Murray, he developed an interested in the area of materials chemistry, which caused him to join Dr. Marc R. Knecht's lab at the University of Kentucky's Chemistry Department in 2008. In fall of 2008, Ryan as accepted to the doctoral program at the University of Kentucky and joined Marc Knecht's lab at the end of that semester. Ryan later transferred with Marc to the University of Miami, Florida. Under Dr. Knecht's supervision, he conducted research on understanding how peptide orientation and sequence effects can control material size and activities of inorganic nanoparticles and published several articles in peer-reviewed journals.